

<https://doi.org/10.15388/vu.thesis.349>

<https://orcid.org/0000-0001-7148-3335>

VILNIUS UNIVERSITY

CENTER FOR PHYSICAL SCIENCES AND TECHNOLOGY

Oleg Kravcov

Kinetic Monte-Carlo Simulations of Carrier Dynamics in III-Nitrides

DOCTORAL THESIS

Natural sciences,
Physics (N 002)

VILNIUS 2022

The dissertation was prepared within the period from 2016 to 2021 at the Institute of Photonics and Nanotechnology. The research was supported by the Research Council of Lithuania.

Academic supervisor – Prof. Habil. Dr. Gintautas Tamulaitis (Vilnius university, natural sciences, physics, N 002)

This doctoral thesis will be defended at a public meeting of the Dissertation Defence Panel, consisting of:

Chairman – Prof. Dr. Darius Abramavičius (Vilnius university, natural sciences, physics N 002).

Members:

Dr. Linas Ardaravičius (The center for physical sciences and technology, natural sciences, physics N 002),

Dr. Karolis Kazlauskas (Vilnius university, natural sciences, physics N 002),

Dr. Anatolijs Šarakovskis (Institute of solid state physics, university of Latvia, natural sciences, physics, N 002),

Prof. Habil. Dr. Sigitas Tamulevičius (Kaunas university of technology, technological sciences, materials engineering, T 008).

The dissertation will be defended at a public meeting of the Dissertation Defence Panel on 15 September, 2022 in room A101 at the Institute of Photonics and Nanotechnology.

Address: Saulėtekio al. 3. Vilnius, Lithuania

Tel. (85) 264 9211; e-mail: office@ftmc.lt

The text of this dissertation can be accessed at the Martynas Mažvydas national library, the library of Vilnius university and the center for physical sciences and technology as well as on the website of Vilnius University:

www.vu.lt/lt/naujienos/ivykiu-kalendorius

<https://doi.org/10.15388/vu.thesis.349>

<https://orcid.org/0000-0001-7148-3335>

VILNIAUS UNIVERSITETAS
FIZINIŲ IR TECHNOLOGIJOS MOKSLŲ CENTRAS

Oleg Kravcov

Krūvininkų dinamikos III grupės
nitriduose modeliavimas kinetiniu
Monte Karlo metodu

DAKTARO DISERTACIJA

Gamtos mokslai,
Fizika, (N 002)

VILNIUS 2022

Disertacija rengta 2016–2021 metais Fotonikos ir Nanotechnologijų Institute.
Tyrimus rėmė Lietuvos mokslo taryba.

Mokslinis vadovas – Prof. Habil. Dr. Gintautas Tamulaitis (Vilniaus universitetas, gamtos mokslai, fizika, N 002)

Gynimo taryba:

Pirmininkas – Prof. Dr. Darius Abramavičius (Vilniaus universitetas, gamtos mokslai, fizika, N 002).

Nariai:

Dr. Linas Ardaravičius (Fizinių ir technologijos mokslų centras, gamtos mokslai, fizika, N 002),

Dr. Karolis Kazlauskas (Vilniaus universitetas, gamtos mokslai, fizika, N 002),

Dr. Anatolijs Šarakovskis (Kietojo kūno institutas, Latvijos universitetas, gamtos mokslai, fizika, N 002),

Prof. Habil. Dr. Sigitas Tamulevičius (Kauno technologijų universitetas, Technologijos mokslai, medžiagų inžinerija, T 008).

Disertacija ginama viešame Gynimo tarybos posėdyje 2022 m. rugsėjo mėn.
15 d. Fotonikos ir Nanotechnologijų institute A101 posėdžių salėje.

Adresas: Saulėtekio al. 3, Vilnius, Lietuva),
tel. (85) 264 9211; el. paštas office@ftmc.lt

Disertaciją galima peržiūrėti Lietuvos nacionalinėje Martyno Mažvydo, Vilniaus universiteto ir fizinių ir technologijos mokslų centro bibliotekose, bei Vilniaus universiteto interneto svetainėje adresu:

<https://www.vu.lt/naujienos/ivykiu-kalendorius>

LIST OF ABBREVIATIONS

Acronym	Meaning
2D	Two-Dimensional
3D	Three-Dimensional
CDF	Cumulative distribution function
DOS	Density of States
EBL	Electron Blocking Layer
FWHM	Full Width at Half Maximum
IQE	Internal Quantum Efficiency
kMC	Kinetic Monte-Carlo
LA	Longitudinal Acoustic
LDOS	Density of Localized States
LED	Light Emitting Diode
LO	Longitudinal Optical
MBE	Molecular Beam Epitaxy
MC	Monte-Carlo
MOCVD	Metalorganic Chemical Vapor Deposition
MQW	Multiple Quantum Wells
NRC	Non-Radiative Recombination Center
PDF	Probability density function

PL	Photoluminescence
RNG	Random Number Generator
SRH	Shockley-Read-Hall

ACKNOWLEDGEMENT

I would like to express my sincere thanks to my supervisor prof. Gintautas Tamulaitis for helping me with my studies and more during all these years.

Also, I would like to thank dr. Jūras Mickevičius for mentoring and huge help with model creation. As well as dr. Ramūnas Aleksiejūnas for the fruitful discussions which lead to a better understanding of model.

And finally, thanks all colleagues for sharing with experimental data and jus simple moral support.

CONTENTS

INTRODUCTION	11
Main Goal.....	12
Objectives.....	12
Novelty and importance	13
Thesis statements	14
Layout of the thesis.....	14
Author’s contribution.....	16
List of publications	17
List of conference presentations.....	17
1. LITERATURE REVIEW.....	18
1.1. III–nitrides	18
1.2. Carrier localization	20
1.3. Carrier recombination.....	22
2. THEORETICAL MODEL	25
2.1. Kinetic Monte-Carlo algorithm.....	25
2.2. Generating states	26
2.3. Particle generation and update.....	26
2.4. Types of events	28
2.4.1. Localized carriers.....	29
2.4.2. Free carriers.....	30
2.5. Phonon scattering	33
2.6. Diffusion	34
3. RESULTS AND DISCUSSION	37
3.1. Dynamics in a system of localized carriers in AlGaIn.....	37
3.1.1. Experimental details.....	37
3.1.2. PL spectra simulations.....	37
3.1.3. PL intensity simulations.....	42
3.1.4. Conclusions.....	49
3.2. Free and localized carrier dynamics in AlGaIn.....	51
3.2.1. Experimental details.....	51
3.2.2. Simulation details.....	52
3.2.3. Simulation of PL spectra	52
3.2.4. PL Efficiency simulations	59
3.2.5. Conclusion	66

3.3. Diffusion in a common system of free and localized carriers in InGaN ..	68
3.3.1. Experimental details	68
3.3.2. Simulation of diffusion	69
3.3.3. Simulation of diffusion using Monte – Carlo method	70
3.3.4. Fitting of the calculated dependences with those obtained experimentally	78
3.3.5. Conclusion	82
CONCLUDING STATEMENTS	84
LIST OF REFERENCES	86
SANTRAUKA.....	95
Darbo tikslai	96
Darbo užduotys	96
Mokslinis naujumas ir svarba	97
Ginamieji teiginiai	98
Autoriaus indėlis	98
1. TEORINIS MODELIS	99
1.1. Monte-Karlo algoritmas	99
1.2. Būsenų generavimas	100
1.3. Dalelių generavimas ir atnaujinimas	100
1.5. Įvykių tipai	102
2. REZULTATAI IR JŲ APTARIMAS	106
2.1. Lokalizuotų krūvininkų dinamika AlGaN	106
2.1.1. Fotoluminescencijos spektro modeliavimas.....	106
2.1.2. Fotoluminescencijos našumo priklausomybės nuo temperatūros modeliavimas	109
2.1.3. Išvados	111
2.2. Laisvųjų ir lokalizuotų krūvininkų dinamikos AlGaN kristale modeliavimas	112
2.2.1. Fotoluminescencijos spektro modeliavimas.....	112
2.2.2. Fotoluminescencijos našumo modeliavimas	114
2.2.3. Išvados	117
2.3. Difuzijos modeliavimas sistemuose su laisvais ir lokalizuotais krūvininkais	118
2.3.1. Difuzijos modeliavimas	118
2.3.2. Modeliavimo rezultatų tapatinimas su eksperimentiniais	120
2.3.3. Išvados	122

3. APIBENDRINIMAS	123
CURRICULUM VITAE.....	125
LIST OF PUBLICATIONS AND TEIR COPIES	126

INTRODUCTION

In modern life, light emitting diodes (LEDs) become dominating light sources in many applications (displays, traffic lights, greenhouse lighting and other important fields) and, most importantly, in general lighting with capability to save up to 10% of the world-wide electricity consumption. The first LEDs are known for more than half a century, the interest in LEDs was boosted by the development of GaN-based high-brightness blue LEDs and subsequent development of white LEDs in 1993 [1]. Since then, tremendous amount of research has been done on the development of III-nitride-based devices.

III-nitride-based devices have many advantages, such as their low sensitivity to ionizing radiation and ability to operate at high terahertz frequencies at room temperatures [2]. But most notorious is the possibility to design material for specific band gap energy. By adding fraction Aluminum Nitride (AlN) or Indium Nitride (InN) to GaN system we can create ternary compounds which emission wavelength covers wide range from near infrared, all visible light to deep ultraviolet spectrum. These properties make Nitrides a promising material for Military and Space applications as well as some less obvious implications in medicine, water purifying devices or generating artificial light for plant growing.

Ternary nitride compounds, such as AlGa_N and InGa_N, exhibit quite specific temperature behavior of their photoluminescence spectra. At low excitation densities, the luminescence band peak energy is below the band gap and follows an S-shaped temperature dependence, whereas the dependence of band width has a W-shape [3][4]. This behavior is attributed to the contribution of localized states which can occur due to inhomogeneous composition or the fluctuations in well width [5]. This leads to a strong inhomogeneous broadening of luminescence spectra and increases its intensity due to preventing the nonequilibrium carrier from reaching the nonradiative recombination centers. However, a strong loss in efficiency appears at elevated excitation intensities [6]. This effect is usually referred to as the droop effect.

Understanding the mechanisms behind the efficiency droop as well as understanding the impact of localized carriers on luminescence properties and their interaction of the localized carriers with free electrons and holes is a key issue in the quest to further improve the emission efficiency of III-nitride-based light emitting devices.

Main Goal

The main goal of this study is to develop a model to simultaneously describe free and localized carriers in III-nitrides and exploit the Monte-Carlo technique to simulate the behavior of free and localized nonequilibrium carriers and reveal how the different recombination processes affect the band shape and efficiency of photoluminescence in epilayers and quantum wells with different carrier localization and excitation conditions. Fitting the results obtained experimentally by other authors with corresponding simulated results is used to verify the simulation model and extract the parameters necessary for the simulations. The unique dependences of the emission properties on temperature and the efficiency droop effect in ternary III-nitrides is under especial focus.

Objectives

- i) Developing a theoretical model to simultaneously describe the dynamics of two interacting systems of free and localized carriers in III-nitride epilayers and quantum wells.
- ii) Adopting the kinetic Monte-Carlo simulation to perform calculations of PL dynamics in III-nitride compounds with different strength of carrier localization in a wide dynamic range of the nonequilibrium carrier density.
- iii) Fitting the simulated and experimental results on the temperature and carrier density dependences of PL characteristics in AlGaIn epilayers.
- iv) Investigating the influence of the localization conditions and recombination mechanisms on the photoluminescence band shape and efficiency at low excitation densities.
- v) Analyzing the carrier dynamics in the system consisting of both free and localized carriers and its influence on PL spectra and efficiency.
- vi) Revealing the origin of the efficiency droop effect.
- vii) Evaluating the impact of localization on carrier diffusivity.

Novelty and importance

Monte-Carlo simulation is a well-known method to describe the PL properties in III-nitrides [7][8]. However, the published results are limited to the consideration either free or localized carriers. The single-particle approach is quite acceptable at low excitations, such model is insufficient to explain the influence of localization on PL efficiency droop. Due to the complexity of the system to be modeled and the strong reliance of the Monte Carlo algorithms on transfer rates, which are difficult to properly define and estimate, it is a common practice to describe the quantum efficiency in a more abstract manner by using well known empiric ABC [9] or Arrhenius [10] models. Despite the good congruence of the results obtained by solving these approaches with experimental data at high density of nonequilibrium carriers, they still suffer from strong uncertainty and discrepancy in a wide range of carrier densities. The main limitation of the ABC model is the uncertainty in the ratio between the densities of free and localized nonequilibrium carriers, and the carrier density dependence of the rate coefficients for the processes important for the system. Meanwhile, the Arrhenius expression can be used to describe several different recombination channels, the obtained fitting values are not directly and unambiguously linked with specific recombination mechanisms and rather reflects the combined result of all processes acting in parallel.

The kinetic Monte Carlo simulations exploited in this work provide unique capabilities to extract information from experimental results. The simulation provides the ability to obtain the information on the contributions of specific recombination and transfer mechanisms in real time with the resolution in energy and space. The simulation exploited to simultaneously describe four experimental dependences of the photoluminescence parameters enabled extracting the parameters describing the transfer and recombination processes in the system of nonequilibrium carriers and revealing the influence of the processes on luminescence properties in III-nitrides, what would be not feasible by just phenomenological analysis of the experimental data without the modeling.

Thesis statements

- I. In systems with strong localization and high density of nonradiative recombination centers, the photoluminescence efficiency decreases predominantly because of tunneling of localized excitons to nonradiative recombination centers. Consequently, the internal quantum efficiency is below 100% even at low temperatures and small densities of nonequilibrium carriers.
- II. The efficiency droop as the total density of nonequilibrium carriers increases in III-nitrides with strong carrier localization can be explained by an increasing contribution of nonradiative recombination of free carriers and a decreasing contribution of the radiative recombination of localized excitons at the densities of nonequilibrium carriers below the values sufficient for significant involvement of nonradiative Auger recombination.
- III. Increasing density of nonequilibrium carriers in InGaN initially results in the decrease of the diffusion coefficient due to enhanced carrier localization and is followed by the increase of its value due to increasing share of free carriers. The anisotropy of diffusion in non-polar *m*-plane InGaN is determined by the difference in the dispersion of potential fluctuations for light and heavy holes.

Layout of the thesis

This thesis consists of an [introduction](#), [literature review](#) and [theoretical model](#) chapters followed by chapters [results and Discussion](#) and [Concluding Statements](#).

In [Literature Review \(Ch. 1\)](#) the main properties [of III-group nitrides](#) and their ternary compounds are briefly discussed. The main point of interest in such materials is the strongly expressed effect of [localization](#). We persuade that the main properties of [carrier dynamics](#) are affected by the recombination near band gap and thus both free and localized particles should be taken into account.

The [theoretical part \(Ch. 2\)](#) of the thesis describes step by step the [kinetic Monte-Carlo](#) model used in all further calculations. The developed algorithm

is designed to simultaneously operate with [two types of particles](#): free electrons and holes and localized excitons. Further, we provide detailed information on [types of events of importance](#) and define the system transfer rates. Finally, we discuss some additional effects which could not be included in program code directly, namely, [phonon scattering](#) and changes in [diffusivity](#).

The [Results and Discussion \(Ch. 3\)](#) consists of three parts. Each of them starts with a brief introduction and motivation for specific simulations performed. Next, we shortly overview the experimental data used for fitting and the structure of the samples studied experimentally (Sec. [3.1.1](#), [3.2.1](#), [3.3.1](#)). Adoption of modifications of the source code for more effective execution of the tasks in this work is described in more detail in sections [3.1.2](#), [3.2.2](#), and [3.3.3](#).

The first part [Results and Discussion](#) is dedicated to the dynamics in a [system with localized carriers \(Sec. 3.1\)](#). The measurement was obtained under low excitation conditions, thus the single particle kMC was used. We examine the temperature behavior of the [photoluminescence spectra](#) and compare the obtained results with those reported in literature. The key point of this section is to simulate the [PL intensity](#) dependence on temperature for AlGaIn MQWs and understand how it is affected by localization.

Second section is devoted to PL dynamics of a [system with free and localized carriers \(Sec. 3.2\)](#). Here, we expand our model to perform simulations at much higher carrier density by using multi-particle kinetic Monte-Carlo algorithm. [The photoluminescence spectra](#) behavior under different localization and excitation conditions were analyzed. These simulations were aimed at explaining the [PL efficiency](#) dynamics in AlGaIn and finding the processes causing the PL efficiency decrease at increasing excitation intensity usually referred to as the droop effect.

Finally, in the third part of the [Results and Discussion](#), we focus on the study of [carrier diffusivity \(Sec. 3.3\)](#). The complex diffusion coefficient dependence on carrier density in InGaIn-based heterostructures was simulated using both [theoretical](#) and [kinetic Monte-Carlo](#) approaches. We discuss the effects of strong localization on carrier mobility and study the origin of [anisotropic diffusivity](#) in experimentally studied samples.

The [concluding statements \(Ch. 4\)](#) summarize the results obtained by the Monte-Carlo simulations exploiting the model developed in this work to reveal the impact of carrier localization on the dynamics of nonequilibrium carriers in III-nitrides.

Author's contribution

The development of the model and all the theoretical calculations using the kinetic Monte-Carlo simulations presented in this work were performed by the author. The code used for kMC modeling was created from scratch using C++ and was upgraded in accordance with the objectives of the current study during the entire study period.

All experimental data used in this work were obtained by colleagues at the Institute of Photonics and Nanotechnology, Vilnius University.

List of publications

- P1) O. Kravcov, J. Mickevičius, G. Tamulaitis, [*Kinetic Monte Carlo simulations of the dynamics of a coupled system of free and localized carriers in AlGaN*](#), Journal of Physics: Condensed Matter, vol. 32, no. 14, p. 145901, **2020**.
- P2) R. Aleksiejūnas, K. Nomeika, O. Kravcov, S. Nargelas, et al, [*Impact of Alloy-Disorder-Induced Localization on Hole Diffusion in Highly Excited c-Plane and m-Plane \(In, Ga\) N Quantum Wells*](#), Physical Review Applied, vol. 14, no. 5, pp. 1–11, **2020**.
- P3) O. Kravcov, J. Mickevičius, G. Tamulaitis, [*Origin of thermal quenching of exciton photoluminescence in AlGaN epilayers*](#), Lithuanian Journal of Physics, vol. 61, no. 2, pp. 84–90, **2021**

List of conference presentations

- i) O. Kravcov, J. Mickevičius, G. Tamulaitis, *Recombination Dynamics In III-Nitride Semiconductors with Carrier Localization*, 46th International School & Conference on the Physics of Semiconductors, Jaszowiec 2017, Poland, Szczzyrk, June 17 - 23, **2017** . (Poster)
- ii) O. Kravcov, J. Mickevičius, G. Tamulaitis, *Kinetic Monte Carlo Simulations of Carrier Dynamics in AlGaN/AlGaN Quantum Wells*, 13th International Conference on Nitride Semiconductors (ICNS-13), USA, Bellview, July 6-13, **2019**. (Oral)
- iii) O. Kravcov, J. Mickevičius, G. Tamulaitis, *Monte Carlo Simulations of Optical Properties in III-Nitrides*, Lietuvos nacionalinė fizikos konferencija LNFK -43, Kaunas, spalio 3 – 5 , **2019**. (Stendinis)
- iv) O. Kravcov, J. Mickevičius, G. Tamulaitis, *Monte Carlo simulations of carrier dynamics in coupled systems of free and localized carriers in III - Nitrides*, Int. Conf. Towards Understanding and Modelling Intense Electronic Excitation, Warsaw, Poland, February 17-18, **2020**. (Oral)

1. LITERATURE REVIEW

1.1. III-nitrides

III-nitrides are a group of direct-band-gap compound semiconductors consisting of nitrogen and group III elements, predominantly gallium (Ga), aluminum (Al) and indium (In). Since 1990-ties, these semiconductors became extensively used in optoelectronics, especially in light-emitting diodes, lasers, and photodetectors. Though GaN-based devices were known for decades, this class of semiconductors got a lot of attention after the introduction of p-type GaN doped with Mg and development of high-brightness blue and, later, green LEDs [1]. Currently, the ternary III-nitride compounds, such as AlGaN and InGaN, are under intense research, as they provide a unique source of light sources covering a wide range from near infrared to deep ultraviolet, including the entire visible spectrum.

The III-nitride alloys can be crystallized in cubic zinc-blende and hexagonal wurtzite structures graphically represented in Figure 1.1. In some rare cases like in a pair with II-group or rear-earth metals, III-nitrides can also crystalize in a rock salt structure [11]. Due to its thermal stability, most of the currently available devices are based on wurtzite-structure crystalline structure grown in c -direction [0001]. Another interesting material is non-polar m -plane [1 $\bar{1}$ 00] III-nitride layers grown along a -axis. Such layers have no effect of polarization-induced built-in electric fields [12][13]. The zinc-blende phase could theoretically achieve higher efficiency due to the absence of polarization field, whereas the rock salt structure is known for its unique electrical properties.

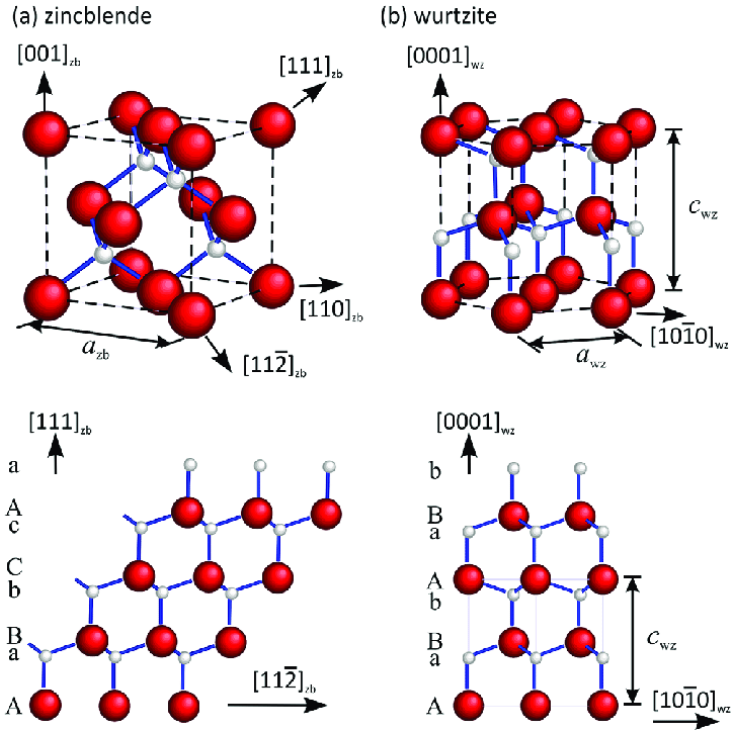


Fig 1.1. Crystal structure of zinc-blende (a) and wurtzite (b) GaN [14].

Group III-nitrides in their hexagonal/wurtzite structure typically have direct band gap, so their main optical properties are defined by recombination near band edge energy. with 3.4 eV, while AlN – 6.2eV and InN ~0.7eV at 300K temperature. Such wide band gap is unique among other common direct band semiconductors like phosphide (P), arsenide (As) and antimonide (Sb) usually operate in infrared sector. By mixing several materials we can attune the energy band gap E_g in ternary allows such as $Al_xGa_{x-1}N$ or $Al_xGa_{x-1}N$ $In_xGa_{x-1}N$ which is described by following the Vegard's law:

$$E_g = E_{g1}x + E_{g2}(1 - x) - E_{12}(x * (x - 1)) \quad 1.1.$$

here, E_{g1} and E_{g2} represent band gap energies of first and second material and E_{12} is lattice bonding parameter which is obtained from experimental measurements. X -represent part of the element in alloy, as such with increase fraction of aluminum the band gap goes up and similar with increase of indium band energy decrease.

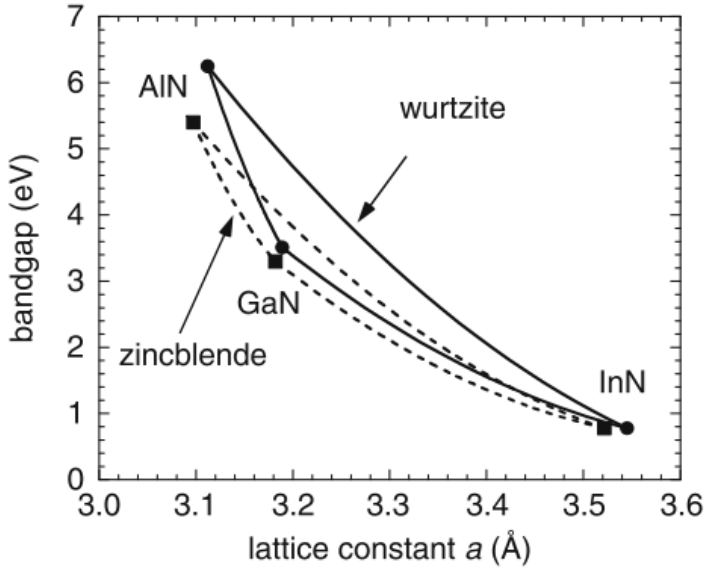


Fig 1.2. The band gap energy and Lattice parameter of III-nitride compounds [14].

Meanwhile, the electronic interband transmission is also affected by temperature. Canonically, the temperature dependence of band gap energy can be expressed using empiric Varshni expression [15]:

$$E_g(T) = E_g(0) - \frac{\alpha T^2}{T + \beta} \quad 1.2.$$

The $E_g(0)$ is band gap at zero temperature, α and β Varshni parameters acquired from experimental data. Such decrease usually attributed to increase in with rise of atomic vibration amplitude which affect global electronic band structure.

1.2. Carrier localization

Considerable, the most notable characteristic of III-nitride compounds is the strong localization. Spatial band gap variations due to inhomogeneities in composition, quantum well (QW) thickness, strain as well as just a random fluctuation in In-N bonds lead to occurrence of significant number of localized states. In such system the carriers can be captured by localized states below the band gap energy forming exciton like electron-hole pairs. Localized

carriers can stay in non-equilibrium state for long period of time as such particle can move only by hopping through nearby empty localized states. As a result, in a system with strong localization most of the classical distribution models based on Boltzmann distribution struggle to describe behavior of carrier dynamics. However, the energy distribution of localized states can be described by normal distribution (or in some works by Boltzmann) with a dispersion parameter of the potential fluctuation σ . The localized states are distributed randomly in space and the mean energy value corresponds to band gap energy at that location. The double scale potential model suggests what due to inhomogeneous distribution in alloy there are some larger scale band gap fluctuations with energy Γ [16]. This leads to formation of spatially separated “islands” with different average energy of localized states. The schematic representation of potential field fluctuation is shown in Fig 1.3. Due to potential barrier and small diffusivity localized carriers tends to stay in same area they were captured and thus most PL dynamics depends on smaller dispersion parameter σ .

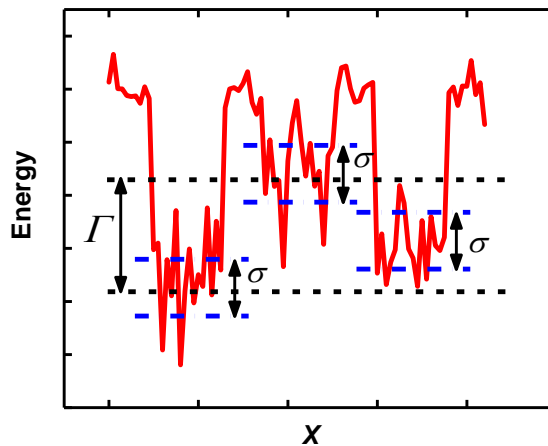


Fig 1.3. Schematic representation of potential field fluctuations. Red line shows possible potential field fluctuations.

The presence of localized states can be indicated in experiments by a strong inhomogeneous broadening of the photoluminescence spectra [5]. Furthermore, the localization of carriers leads to an unusual temperature dependence of the PL band peak energy and width: so called “S-shaped” and

“W-shaped” dependences, respectively. Such behavior is well known and have been studied for long time in InGaN [7][17][18] and AlGaIn [4][19][20][21] alloys. The spatial variations of emission intensities and/or peak positions have been studied directly by confocal microscopy [22][23][24], scanning near-field optical microscopy (SNOM) [25][26][27][28], and cathodoluminescence [29][30]. The potential fluctuations on several spatial scales were revealed with the largest domains of a micron size and the smallest on the scale of a few nm [31][32].

Localization strongly affects the performance of photonic devices based on ternary and quaternary III-nitride alloys. The main reason behind such impact is the limited transportation of strongly localized carriers. On one hand, localization of the nonequilibrium carriers at the minima of the potential fluctuations can be beneficial for the light emission efficiency as the localized carriers are isolated from nonradiative recombination centers [25][22]. This leads to a high internal quantum efficiency even in samples with large dislocation densities [33][34]. On the other hand, it can also act as effective transport channel to NRC if the deep localized state is at near of it, however due to randomize nature of distribution of localized states it is rarely the case. In a similar manner, the strong localization has some positive and negative influence on stimulated emission [35][36][37].

In current state the main disadvantage of the III-nitride devices is the global decrease in internal quantum efficiency at higher excitation densities also known as droop effect. While the numerical calculation base on ABC [38][39] model could provide significant fit with experimental data, nevertheless, there is still debates on the origin of efficiency droop. This effect is often attributed to increase in Auger recombination rate [40] as delocalized particles tend to spawn in the same space. Alternatively, delocalization-activated nonradiative recombination or incomplete carrier localization have been suggested as another efficiency droop mechanisms [29][41].

1.3. Carrier recombination

The proper estimation of recombination rates of free and localized carriers is crucial for Monte-Carlo type simulations. However, due to the random nature of the band potential fluctuations, modeling of the carrier dynamics within the localizing potential is a challenging task. Usually, it requires solving the Schrödinger equation for electrons and holes in random localizing potential and determining the energies and the spatial structure of the localized quantum states. Recently, a method based on localization landscape theory

has been proposed, which somewhat reduces the complexity by replacing the Schrödinger equation with a simpler one [42][43].

Simplified approaches to modeling the system consisting of free and localized carriers are typically based on reducing the system to a single dominant constituent of either free or localized carriers at certain conditions. The former is analyzed using the standard ABC model [9][39][44], there recombination rate R is described as a sum of all possible processes:

$$R(N) = AN + BN^2 + CN^3 \quad 1.3.$$

where N is density of free carriers and A, B, C is coefficients for Shockley–Read–Hall, bimolecular and Auger recombination, respectively. Modified recombination rates can be added to consider localized carrier migration and recombination [23] or excitonic recombination [45][46]. Comprehensive version of these models could be expressed as follows:

$$\begin{cases} \frac{dN}{dt} = G - AN - BN^2 - CN^3 - \gamma_{\downarrow}N + \gamma_{\uparrow}n \\ \frac{dn}{dt} = \gamma_{\downarrow}N - Dn - En - \gamma_{\uparrow}n \end{cases} \quad 1.4.$$

Here, G is generation rate, n is density of localized carriers/excitons. D represent the radiative lifetime and E - non-radiative recombination by tunneling to NRC. Though last one usually gets neglected as the main mechanism of nonradiative recombination is attributed to the SRH recombination [47][48][49]. The localization γ_{\downarrow} and γ_{\uparrow} delocalization coefficients describe transfer rate between two systems. Unfortunately, these models often rely on statistic average to describe the ratio between free and localized carriers or evaluation of respected transfer rates, which is not a trivial task considering complex nature of potential fluctuations. Another flaw is that coefficients themselves can depend on carrier density, have nonlinear response, or vary due to external conditions.

The more abstract way to describe carrier recombination is to evaluate internal quantum efficiency. Regardless of the specific mechanism, the temperature dependence of the spectrally-integrated PL intensity usually can be described by the Arrhenius expression:

$$I(T) = \frac{I_0}{1 + \sum_i c_i \exp\left(-\frac{E_{Ai}}{k_B T}\right)} \quad 1.5.$$

where I_0 is the low-temperature PL intensity, c_i and E_{Ai} are the rate constant and activation energy of the i -th process, and i is the number of nonradiative recombination channels, typically ranging from 1 to 3. The thermally-activated mechanisms responsible for the PL quenching are usually related to the thermal dissociation of excitons [50][51], escape of carriers out of a quantum well [52], transfer of carriers over a barrier to nonradiative recombination centers [53][54], and thermal activation of localized carriers [55]. However, a few distinct activation energies are hardly compatible with a wide and continuous energy distribution of localized states.

2. THEORETICAL MODEL

Two nonequilibrium carrier subsystems, free electrons and holes and exciton-like localized electron-hole pairs (excitons), are simultaneously described in our model. The free carriers can move independently in space, whereas their energy is determined by the Fermi-Dirac statistics. The excitons are acting as single particles that are trapped by localizing potential, and their energy is fixed at the energy of the localized state they occupy. The excitons can travel in space by hopping through localized states. A set of possible recombination and transfer events depending on their state is assigned to each type of particles. By using Monte – Carlo technique, we simulate the dynamics of the entire system at a fixed carrier density.

2.1. Kinetic Monte-Carlo algorithm

In general, kinetic Monte-Carlo algorithms are suitable to describe the time evolution of the system by updating events according to randomly generated number, given that the correct transition rates are provided. The model for simulating the PL behavior is based on single particle MC [8][56][57]. Certain steps can vary in different simulations, but the calculation procedure can be reduced to solving two problems: determining the time, when the event occurs, and selecting, which specific event will take place [58]. The results of such simulations are obtained by accumulating data from calculations repeated many times, usually 10^5 and more. The simplified procedure of our simulations can be described as follows:

1. *Initializing values.*
2. *Generating states.*
3. *Setting time $t = 0$*
4. *Updating particles*
 - a. *Generating particles.*
 - b. *Choosing and update each particle in a random order.*
 - c. *Rechecking for conflicting events.*
 - d. *Taking the thermal interaction of the particles into account.*
5. *Updating data and increasing time by a step: $t = t + dt$*
6. *Repeating from step 4 while time $t < t_{max}$*
7. *Repeating from step 2 for N times to collect sufficient statistics.*

The same algorithm can be used in single-particle as well as in multi-particle regimes, additional steps can be added or those listed above omitted to decrease the calculation time. This is usually accomplished to prevent overcalculations of the processes which rarely occur under certain conditions and to prevent of stacking nonrelevant data.

2.2. Generating states

In this simulation, we use a 4-dimensional space and energy grid, in which the cells representing states are selected small enough to prevent more than one state occupying the same cell. The localized states with density N_{loc} and nonradiative recombination centers (NRC) with density N_r are generated randomly within the volume, whereas free states exist as an energy continuum above the mobility edge. The localized state energy E is randomly assigned below the mobility edge E_{me} according to the Gaussian distribution [17][21]:

$$f(E) = \frac{1}{\sigma\sqrt{2\pi}} e^{-\frac{1}{2}\left(\frac{E-E_{me}}{\sigma}\right)^2} \quad 2.1.$$

Here, σ is the standard deviation of the energy of localized states. The spatial coordinates of localized states and NRC are generated randomly, no correlation between space and energy is allowed. To increase the simulation performance, both localized states and NRC are assigned to Q-Tree like structures (is a tree data structure in which each internal node has exactly four children).

2.3. Particle generation and update

Particle is an object defined as a single carrier (electron or hole) or a coupled pair of electron and hole (exciton), which can be observed and is described as one entity. By default, electrons and holes can move in free states independently, whereas excitons are represented as bound electron – hole pair capable to move through localized states by hopping. Particles are generated in pairs (electron and hole) with the same spatial coordinates assigned randomly. Particle generation can occur at the beginning of each time step before any of events are calculated depending on configurations. There are three generation regimes: pulsed, quasi-steady-state, and constant-density. In pulsed regime, all carries are generated at the beginning of each new cycle (at

$t = 0$), whereas at quasi-steady-state conditions there is the probability of creating a pair during the entire simulations. At the constant density regime, the number of particles at each time step stays the same. In all three regimes, if by certain reasons, like low excitation densities or short time step, the number of particles required to be generated is not a whole number, the generation of that part is decided by generating a random number.

Particle updating can be subdivided into two random number calculations: finding out whether the selected particle will do anything during the fixed time period and, if yes, selecting the event from cumulative function of possible events. The probability of any event W is calculated using the expression:

$$W = \int_0^{\Delta t} \nu \exp(-\nu t) dt = 1 - \exp(-\nu \Delta t) \quad 2.2.$$

where $\nu = \sum v_i$ is the total sum of the rates of all possible events and Δt is the time step, which should be chosen small enough to make the probability of second successive event during the same time step negligible. This probability does not depend on the starting time t . Additional decay rate factors under integral (2.2) come from normalization. The success of event is accepted if the calculated probability W is greater than randomly generated number $P \in (0, 1]$. Next, the second random number $R \in (0, 1]$ is generated to select the specific event with index i from CDF:

$$\sum_{i=1}^{n-1} v_i < \nu R \leq \sum_{i=1}^n v_i \quad 2.3.$$

Note that the selection from CDF usually is accomplished for efficient calculations by using a binary search. For a single particle regime, the first part can be optimized by reversing the equation. The generated random number can be used to calculate the exact time dt , after which the event occurs, thus skipping inactive steps:

$$dt = \frac{1}{\nu} \ln\left(\frac{1}{P}\right) \quad 2.4.$$

Unfortunately, this approach does not work in multi-particle regime, as certain rates may change over time while other ones depend on the system state which fails to be updated due skipped time steps.

2.4. Types of events

Figure 2.1 represents all events considered in the present model. Here, we can divide the events into three subcategories. The first category comprises the events resulting in elimination of a particle. For simplicity, we calculate their probabilities from the point of view of electron and assume that carriers recombine in pairs. In such a way, each successful recombination process for electron causes the same process for hole. The only difference between radiative and nonradiative recombination is that in the first case a photon with energy of the corresponding particle pair is generated. The energy of this photon is used for updating the PL spectrum. The second process simply removes these particles from the pool.

The second event category can be referred to as transport. The particles after this event change their coordinate or energy. For localized particles, the values are changed for the pair, whereas the state of free carriers can be updated separately.

Finally, there is a category of transfer events: the electron-hole pair can be bound into exciton or exciton can dissociate into free electron and hole. There are several different mechanisms in each category, some of them can be neglected in the real situation under study.

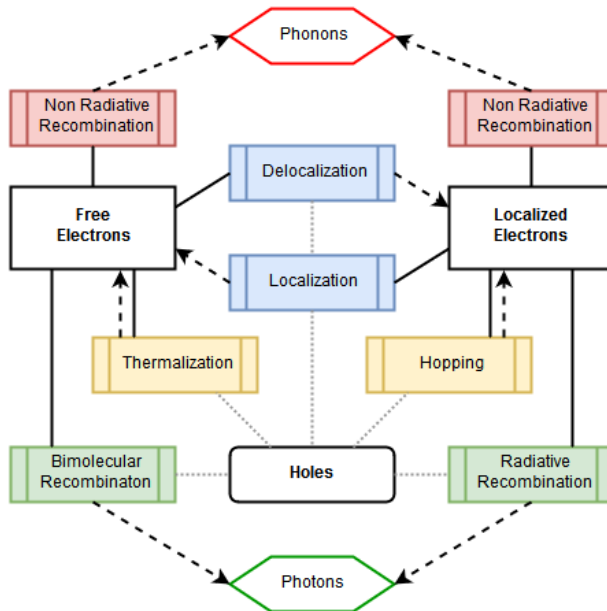


Fig 2.1. Schematic representation of possible events for carrier update.

2.4.1. Localized carriers

Localized carriers are a bound electron-hole pair in a localized state, thus most of the event types have some energy dependent rates. Traditionally, the main properties of system behavior are defined by exciton hopping and radiative recombination. In samples with low localization effect or under high excitation, delocalization process needs to be taking into account. Finally, in systems which consist of a large amount of NRCs the non – radiative recombination due to tunneling can occur.

The transition rate between two states for localized excitons can be defined using the classical Miller-Abraham's expression [59]:

$$v_{i \rightarrow j} = v_0 \exp\left(-\frac{2R_{i \rightarrow j}}{\alpha}\right) \exp\left(-\frac{(E_j - E_i) + |E_j - E_i|}{2k_B T}\right) \quad 2.5.$$

Here, v_0 is the attempt to escape frequency, which is related to the phonon vibration frequency. The tunneling effect is defined by the first exponential part with R_{ij} as the distance between two states and α as the decay length of exciton wavefunction. Finally, E_i and E_j are the energies of initial and final states, respectively, T is the temperature, and k_B is the Boltzmann constant. To get the total hopping rate, we need to take a sum through all possible transitions to non-occupied states:

$$v_{hopp} = \sum_{i \neq j}^{N_{loc}} v_{i \rightarrow j} \quad 2.6.$$

In simulation, we can reduce the calculation time by considering only the nearest neighbors, since the probability of tunneling to distant states is negligible. Over the course of simulation, we found out that it is better to calculate all possible outcomes of hopping rates beforehand, if the localized particle density is expected to be high, whereas to run the calculation only on demand, as the total number of possible hops can put stress on computer system.

The radiative recombination rate can be calculated as linear process with fixed lifetime:

$$v_{rad} = \frac{1}{\tau_{rad}} \quad 2.7.$$

where τ_{rad} is exciton radiative lifetime. It seems this rate does not dependence on the energy of localized state [60]. The value of the rate is determined by how strong electron-hole wave functions overlaps.

For this model, we define the main mechanism of non-radiative recombination for localized excitons as tunneling to NRC. The origin of such centers can be attributed to gallium vacancies, native defects, interstitial and antisite defects or impurities [61]. Recombination rate depends on distribution of both localized states and NRCs. We assume that the energies of all NRCs serving as the final state are lower than the initial exciton energy, which is typically a case for a III-nitride semiconductors [62][63]. we can rewrite the rate as a sum of all possible hops to nearest NRCs:

$$v_{nonrad} = v_0 \sum_{NRC} \exp\left(-\frac{2R_{i \rightarrow NRC}}{\alpha}\right) \quad 2.8.$$

$R_{i \rightarrow NRC}$ being the distance between exciton and NRC. This is basically the same Miller-Abraham's expression with the second member being equal to 1. In a similar manner, the delocalization can be described as vertical jumps from a localized state to free states above mobility edge E_{me} :

$$v_{deloc} = v_0 \exp\left(-\frac{(E_{me} - E_i)}{k_B T}\right) \quad 2.9.$$

2.4.2.Free carriers

The recombination rates of free carriers are under study for a long time. Differently from localized particles free electrons and holes can move independently. Furthermore, their location and energies are not fixed at a single value.

The rate of interaction between free carrier and phonon is substantially larger than that for other events and can occur thousands of times during a single step. Consequently, it is almost impossible to calculate the real time energy values. Instead, we generate them randomly according to the Fermi-Dirac distribution:

$$F(E, T) = \frac{1}{\exp\left(\frac{E - E_F}{k_B T}\right) + 1} \quad 2.10.$$

where T is the temperature and k_B is the Boltzmann constant. Quasi-Fermi level energy E_F depends on free carrier density n and can be obtained by numerical calculations using the following expression:

$$n(E_F) = \int_{-\infty}^{\infty} F(E, E_F) g(E) dE \quad 2.11.$$

Here, $g(E)$ is the density of states. The spatial distribution of free carriers over the volume should be homogenous due to its random nature. Thus, the diffusion effect can be neglected. Consequently, the particle coordinates can be updated as a result of a Brownian-like movement using a random step with thermal velocity.

$$v_{th} = \sqrt{\frac{\mathcal{D} k_b T}{m^*}} \quad 2.12.$$

Here, m^* is the carrier effective mass and \mathcal{D} is the targeted dimension. At the end of each step, the particle moves in a random direction by a random length l_{th} , which is calculated so that the average velocity would end up with the same value as the thermal velocity:

$$l_{th} \in [0, C v_{th} \Delta t] \quad 2.13.$$

Here, Δt is the step time, C is a normalization parameter equal to 2, 3/2, and 4/3 for 1D, 2D, and 3D.

The main mechanism of radiative recombination for free carriers is the band-to-band recombination also referred to as bimolecular recombination. For a single electron, the radiative recombination rate can be defined as:

$$v_{rad} = B' p \quad 2.14.$$

where, p is the hole density and B' is the bimolecular recombination coefficient. The total recombination rate after updating the state for all electrons will be proportional to the classical expression np or n^2 when the

electron and hole densities are equal. Though this expression is strongly simplified, it works well for most of the time, since the bimolecular recombination in our simulations is mostly overshadowed by other processes. For more accurate calculations, we can include the dependences of the bimolecular recombination coefficient on temperature and carrier density. To evaluate the dependences, we compare Fermi-Dirac distribution and density of states of both electrons and holes for specific parameters:

$$B(T, n) \sim \int_{-\infty}^{\infty} F_e(E + E_{me}, T, n) g_e(E + E_{me}) * F_p(-E, T, p) g_p(-E) dE \quad 2.15.$$

This dependence can be further simplified to expressions:

$$B(n) \sim \frac{B_0}{1 + \frac{n}{n^*}} \quad 2.16.$$

Here, B_0 is the low-density coefficient, and n^* is the carrier density at the saturation threshold. The temperature dependency typically defined as[64]:

$$B(T) \sim B_0 T^{-\frac{D}{2}} \quad 2.17.$$

where D is the dimensionality of the system.

There are several mechanisms of non-radiative recombination of free carriers. The simplest way to describe this process is to introduce the particle capture rate ν_{cap} which is different from the average time necessary for a free carrier to reach the NRC. Unfortunately, such parameter is sample specific and has little to no information about the origins of the recombination mechanism. The other approach is to consider the density of nonradiative recombination centers, which is defined as a normalized version of that obtained in the Shockley-Read-Hall model [65]:

$$\nu_{non} = \nu_{cap} N_{NRC} \equiv \nu_{th} \sigma N_{NRC} \quad 2.18.$$

where N_{NRC} and σ are the density and cross - section of NRCs, respectively.

Another common way to describe the non-radiative recombination is based on the assumption that the free particle has to overcome a barrier with activation energy E_A to be captured by a NRC:

$$v_{non} = v_{cap} \exp\left(-\frac{E_A}{k_B T}\right) \quad 2.19.$$

However, such expression can be seen as a combination of two already described processes - delocalization of a localized particle followed by its capture by NRC.

Similarly, to the capture by NRC, free carriers can be captured by localized states. This event we refer to as localization. The only difference in these processes is that the particle can be captured only by non-occupied localized states, as only one exciton at a time can be at certain localized place.

$$v_{loc} = v_{cap} N_{loc} \quad 2.20.$$

Here, N_{loc} is the number of free localized states or the number of free states within a specific localization radius.

2.5. Phonon scattering

The suggested model is good for explaining the free and localized carrier dynamics or distribution. However, for a better fit between simulated and experimental photoluminescence spectra and experimental data, we should consider additional effects, especially, a double-scale character of fluctuations of potential field [16] and photon-phonon interaction. The double-scale model suggests that there should be macroscopic fluctuations in potential field landscape. The second dispersion parameter Γ might be introduced to describe the fluctuations of the average potential in the different macroscopic areas of lower potential. Such spatial variance does not affect the local carrier dynamics, but instead broadens the all-over spatial carrier distributions, which are reflected in an increased width of PL bands. The logical way to include this effect is to add additional Gaussian distribution to the mobility edge energy between different cycles of simulation. At the same pace, we can simply employ the Gaussian convolution on the final PL spectra to obtain same result.

The photon-phonon interaction can be added as additional scattering of the emitted photon $\Delta\phi$ expressed as [66][67]:

$$\Delta\Phi = \beta T + \frac{\gamma}{\exp\left(\frac{E_{LO}}{k_B T}\right) - 1} \quad 2.21.$$

Here, β and γ represent the coupling strength of carriers (excitons) with acoustic and LO phonons, respectively, and E_{LO} is the optical phonon energy.

2.6. Diffusion

The diffusion coefficient is not present in our kMC model as a preset parameter. Instead, its value is calculated after the simulations considering the carrier lifetime and mean path. However, it is useful to compare the results of theoretical calculations with the results obtained in our study. Diffusion is a collective process, thus, it strongly depends on carrier density. In systems without localization, this dependence can be explained using general Einstein equation of relation between diffusivity and mobility in degenerate bands:

$$D(N) = \frac{k_B T}{e} \mu A(\eta) = D_0 A(\eta) \quad 2.22.$$

$$A(\eta) = \frac{\mathcal{F}_{1/2}(\eta)}{\mathcal{F}_{-1/2}(\eta)}, \quad \eta = \frac{E - E_F}{k_B T}$$

Here D_0 is the low-density diffusion coefficient without localization, $\mathcal{F}_{\pm 1/2}(\eta)$ are the Fermi integrals. In general, the Fermi integral with order of $1/2$ describes the relation between free carrier density and Fermi energy $N = N_{\text{eff}} \mathcal{F}_{1/2}(\eta)$ [68]. Here N_{eff} is effective density of states and η Fermi level energy in respect to band edge. For a Boltzmann statistic parameter $A(\eta)$ equal 1. To take into account the localization, we use a modified version of Eq. 2.23, as proposed in [69]:

$$D(N) = \frac{D_0 A(\eta)}{1 + A(\eta) \frac{E_U N_L}{k_B T N_F}} \quad 2.23.$$

where E_u is the Urbach energy corresponding to the energy dispersion of localized states. N_L and N_F represent the densities of localized and free carriers, respectively, whereas the total density $N = N_L + N_F$. This model is based on the assumption that the carriers in localized states are immobile. This assumption is correct in systems with a high potential energy dispersion.

Consequently, the increase in the density of localized states leads to a slower rise in the diffusivity compared to that in the systems without localization.

On the other hand, Eq. 2.23 can be converted into a form convenient to be used in our kMC simulations. For that it's better to rewrite the diffusion dependence in terms of free carrier density and quasi – Fermi level energy. Both of these parameters are well known at any given time of calculation. We can exploit the property of Fermi integral to reduce its order then derivative: $\frac{d\mathcal{F}_i}{d\eta} = \mathcal{F}_{i-1}$. As such eq. 2.23 is equivalent to eq. 2.25 which is also known as chemical diffusion coefficient D_N [70]:

$$D_N(N) = \chi D_j \quad 2.24.$$

$$\chi = \frac{N}{k_B T} \frac{\delta\mu}{\delta N}$$

Here, χ is so called thermodynamic factor, μ is the chemical potential. The difference between D_0 and D_j is that the first one is described as a system parameter, whereas the later one is fundamentally related to the behavior of a single particle. This relation is easier to integrate in our model, since all the parameters at the time of simulation are easily extracted. Both parameters A and χ act similarly: they are equal to 1 at low densities of free carriers and increase to 1.5-3 at carrier densities above 10^{19}cm^{-3} .

The enhanced diffusion with increasing carrier density is caused by scattering effects. Electron-hole scattering can be described using Fletcher formula [71]:

$$D_{e-h} = 48\pi^{\frac{3}{2}} 2^{-\frac{3}{2}} N^{-1} (\varepsilon\varepsilon_0)^2 e^{-4} \left(\frac{m_e + m_h}{m_e m_h} \right)^{\frac{1}{2}} \quad 2.25.$$

$$\times \frac{(k_B T)^{\frac{5}{2}}}{\lg \left(1 + 256(\varepsilon\varepsilon_0)^2 N^{-\frac{2}{3}} e^{-4} (k_B T)^2 \right)}$$

Here, ε is the static relative permittivity of the material and ε_0 is the vacuum permittivity. The total change in diffusion coefficient due to scattering can be calculated as:

$$\frac{1}{D_{total}} = \frac{1}{D} + \frac{1}{D_{e-h}} \quad 2.26.$$

At low carrier densities, the scattering effect does not affect the diffusion coefficient. At higher carrier densities, the decrease in diffusivity is approximately of the same magnitude as the increase according to Eq. 2.24.

3. RESULTS AND DISCUSSION

3.1. Dynamics in a system of localized carriers in AlGa_N

In this section, we discuss the dynamics of low-density exciton density systems in ternary nitride compounds simulated using the kinetic Monte-Carlo algorithm. The calculations of free and localized exciton kinetics and, consequently, of PL properties has been performed by stepwise introduction of different processes into the model describing carrier dynamics. This approach enabled us to reveal the importance of the specific processes, study the influence of the parameters defining the rate of those processes and link the parameters with the material properties.

3.1.1. Experimental details

A single AlGa_N epilayer distinguished by strong carrier localization was selected for the study. The Al_{0.65}Ga_{0.35}N epilayer was grown by migration-enhanced metalorganic chemical vapor deposition (MEMOCVD®) on the c-plane sapphire substrate. The photoluminescence was measured under quasi-steady-state excitation conditions. The 5th harmonic (213 nm) of the YAG:Nd laser radiation (pulse duration 4 ns) were used for excitation. A closed-cycle helium cryostat enabled the variation of temperature in the range from 8 to 300 K. The PL signal was analyzed by a double monochromator (Jobin Yvon HRD - 1) and detected by a UV-enhanced photomultiplier.

3.1.2. PL spectra simulations

As a starting point for further simulations the calculate PL spectra. At low excitation densities, the radiative recombination of localized excitons is the dominant radiative process. For such conditions, non-radiative recombination, localization, or delocalization have almost no impact on PL shape thus can be omitted. Typical simulated PL spectra for nitride compounds are shown in Fig. 3.1. Note that the PL peak energy is below the band gap by more than several potential dispersion parameter σ . At low temperatures (blue line), PL shapes are typically asymmetric: the high energy tail is defined by carrier thermal distribution whereas the lower energy slope depends on how fast the carries can reach lower energy states. At elevated temperatures (red line), PL

form becomes more Gaussian-like and tends to follow the distribution of localized states.

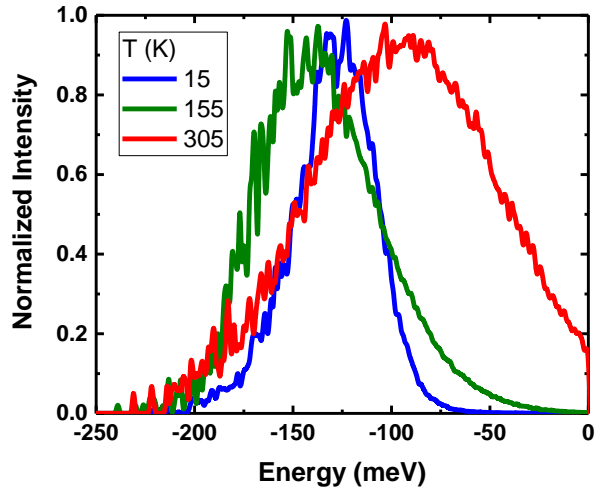


Fig 3.1. Typical simulated PL spectra of AlGaIn MQW under low excitation conditions at different temperatures

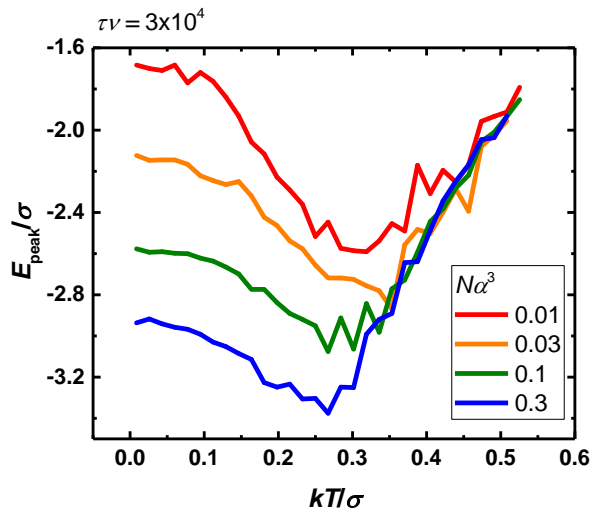


Fig 3.2. Temperature dependence of peak energy of PL band simulated at different parameters $N\alpha^3$ (indicated).

The PL band shape is generally determined by the distribution function of localized states and parameters $\nu_0\tau_0$ and $N\alpha^3$, which govern the localized exciton hopping process in time and space, respectively [8][57]. Fig. 3.2 and Fig. 3.3 represents simulated PL band peak energy dependence on temperature with different parameter pairs.

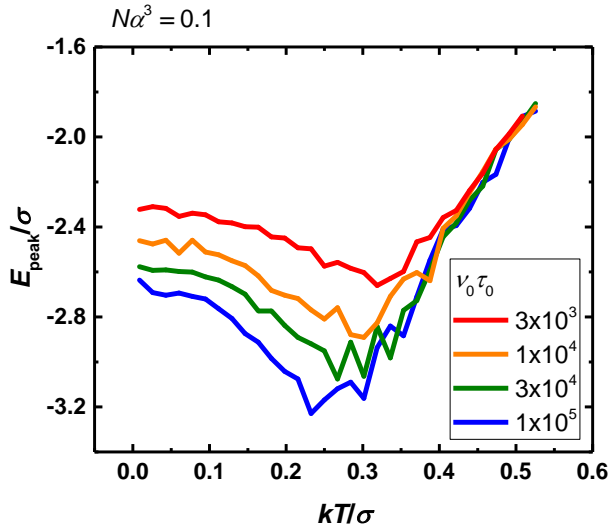


Fig 3.3. Temperature dependence of peak energy of PL band simulated at different parameters $\nu_0\tau_0$ (indicated).

The increase of both $\nu_0\tau_0$ and $N\alpha^3$ values will lead to large Stokes shift at temperatures before thermalization. Furthermore, $N\alpha^3$ also determinates the steep of slope at which mean energy decrease. At elevated temperatures, the influence of localized states becomes insufficient, thus the PL band peak energy approaches the band gap energy and follows Varshni pattern. Also, the decrease in both parameter pairs leads to the small shift of the second turning point of the S-shaped curve towards higher temperatures.

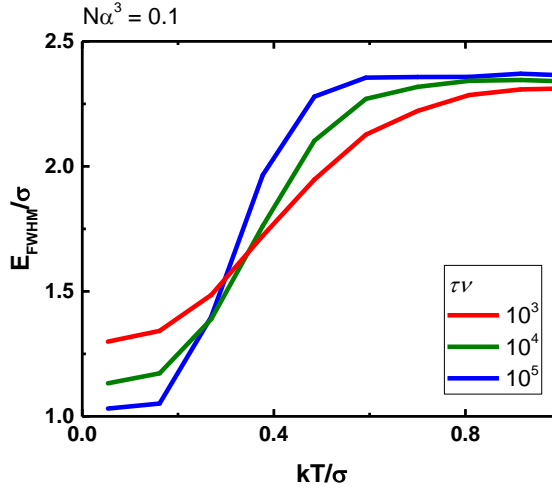


Fig 3.4. Simulated PL FWHM temperature dependence at different values of parameter $\nu_0\tau_0$.

Simulated PL FWHM (Fig. 3.4) smoothly increases with increasing temperature until reaching a constant value around $kT = 0.8 \sigma$. This saturation does not depend on any parameters and is fixed at a value of 2.4σ , although such behavior is not observed experimentally due to further broadening due to photon-phonon scattering. The behavior in low-temperature range is mostly affected by the particle ability to reach lower energy states. The increase in $\nu_0\tau_0$ leads to a sharper initial slope.

To evaluate the energy scale of the distribution of localized states and to estimate the values of exciton hopping parameters, we exploited the temperature dependence of the Stokes shift (defined as the difference between the PL band peak position and the mobility edge), as shown in Fig. 3.5. The measured PL Stokes shift slightly decreases with increasing temperature in the range from 8 to 200 K and increases at elevated temperatures up to 300 K. The Stokes shift with increasing temperature according to a simplified model of band tail filling, referred to as the Eliseev model [17], reproduces the decrease in the Stokes shift at elevated temperatures, as shown by a red dashed line in Fig. 3.5. The application of the Eliseev model in this temperature range enables estimation of the dispersion parameter describing the energy distribution of localized states. For the $\text{Al}_{0.65}\text{Ga}_{0.35}\text{N}$ epilayer under study, σ equals 50 meV. Meanwhile, the fitting of the increase of the Stokes shift and its low-temperature value simulated using exciton hopping model with the experimental results allowed estimating the optimal hopping parameters: $\nu_0\tau_0 = 5 \times 10^4$ and $N\alpha^3 = 0.075$. The simulated Stokes shift dependence on

temperature is presented by a blue solid line in Fig. 3.5 and demonstrates a good agreement with the corresponding experimental dependence.

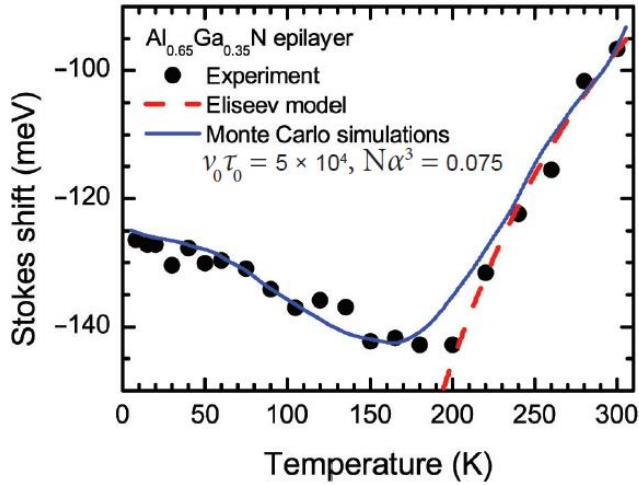


Fig 3.5. Experimental (points) and simulated (line) dependence of PL band peak energy in AlGa_N epilayer on temperature. The dotted line represents Eliseev fit [P3].

Fig. 3.6 represents the PL band width of Al_{0.65}Ga_{0.35}N epilayers as a function of temperature and shows a smooth rise in the width with increasing temperature. Originally simulated PL FWHM (red line) is shifted in energy due to neglect of the additional broadening of macro-scaled potential field. The initial part of simulated dependence seems to follow experimental shape. Though, at temperature above 200 K the curve flattens as we haven't included phonon scattering. Therefore, a more sophisticated model is needed. so further correction (dashed line) is added [16]. The initial variance in the energy of localized states across sample was found to be 60 meV, exciton coupling strength with phonon parameters β and γ was 0.15 meV/K and 1500 meV, respectively. The optical phonon energy was set to 97 meV. Below 200 K, the slight additional rise of FWHM is attributed to interaction with acoustic phonons. Whereas at elevated temperatures it is surpassed by the interaction with optical phonons.

$$\Gamma = 60\text{meV} \quad E_{\text{LO}} = 97\text{meV} \quad \beta = 0.15\text{meV/K} \quad \gamma = 1500\text{meV}$$

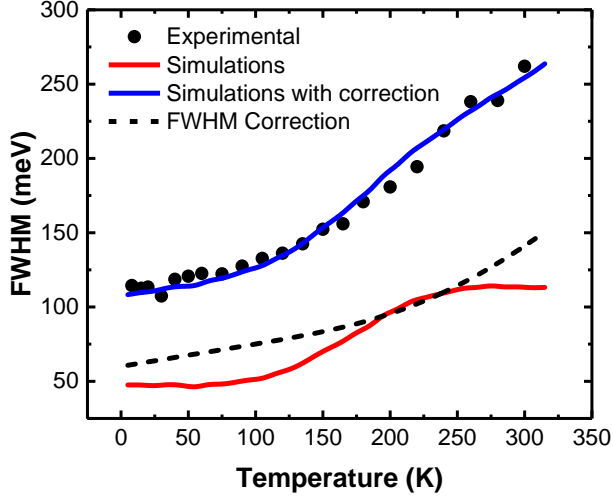


Fig 3.6. Experimental (points) and simulated (red line) PL FWHM of AlGaIn epilayer. Blue line represents PL FWHM after adding FWHM broadening due to interaction with phonons (dashed line).

3.1.3. PL intensity simulations

To better understand the carrier dynamics, we review the impact of different mechanisms on calculated efficiency. By using the obtained parameters, we take into account the non-radiative recombination mechanisms, which previously were omitted. For low excitation densities, we limit the number of possible recombination mechanisms only to excitonic channels according to section 2.5. According to this approach, the PL intensity (and efficiency) is governed by the ratio $N_{\text{nrc}}/N_{\text{loc}}$, which controls the influence of nonradiative recombination [56]. By creating randomly generated nonradiative recombination centers across the simulation grid we are able to simulate PL efficiency with exciton tunneling to NRC or delocalization with followed capture to NRC. Fortunately, there is no rapid changes in non – radiative recombination rate below the mobility edge for both cases, thus the corresponding changes to PL peak position and FWHM are negligible.

The exciton delocalization and subsequent capture by NRCs is the main mechanism of nonradiative recombination in the exciton hopping models presented in literature [57]. This mechanism is governed by the relative density of nonradiative and localized centers and by the temperature. The

curves of PL efficiency as a function of temperature simulated for several values of parameter $N_{\text{nrc}}/N_{\text{loc}}$, are presented in Fig. 3.7. At lowest temperatures, the PL efficiency is close to 100% and drops with the rise in thermal energy. The temperature for the onset of efficiency decrease and the decrease rate afterwards depend on the $N_{\text{nrc}}/N_{\text{loc}}$ ratio. As the ratio increases, the onset of PL efficiency decrease shifts to lower temperatures, which, in turn, results in a lower efficiency at room temperature. This mechanism is basically a two - step process, thus, the low probability of delocalization ensures almost temperature-independent PL intensity at low temperatures. The dependence of non-radiative recombination rate on energy is strongly affected by the ratio of kT to σ , so high localization energy barriers can prevent carries from reaching NRC [72].

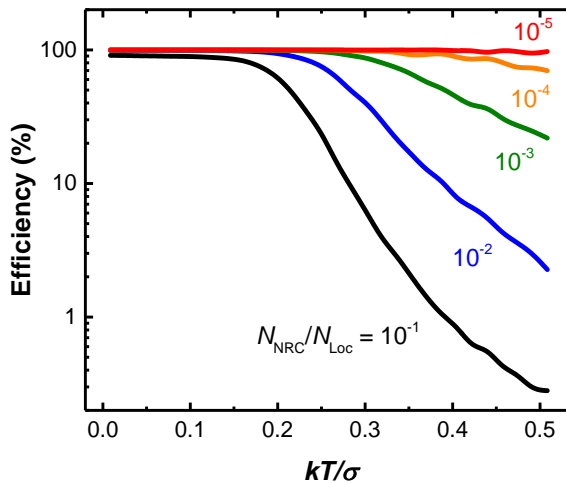


Fig 3.7. Simulated PL efficiency dependence on temperature at different ratios of the density of NRC and localized states. Non – radiative recombination of excitons by delocalization and capture to NRC is taken into account.

The rate of direct exciton tunneling to NRCs depends on how many NRCs are in a close vicinity of a given localized state. Therefore, this mechanism is governed not only by the density of nonradiative centers but also by the density of localized states, described by the parameter $N_{\text{nrc}}/N_{\text{loc}}$. The simulated PL efficiency curves are shown in Fig. 3.8 for several values of this parameter. Usually, the ratio is assumed to be small and the process of exciton tunneling to NRC is neglected. Indeed, for low densities of NRCs, only a slight decrease of the PL efficiency is observed at high temperature, as shown in Fig. 3.8.

Note that the increase in the ratio $N_{\text{nrc}}/N_{\text{loc}}$ results in a significant decrease of the low-temperature efficiency value and a gradual decrease starting already at low temperatures. The former feature is consistent with the previously reported experimental results [73], whereas it is not observed for the nonradiative recombination via delocalized states discussed above. Differently from the published results, the energy distribution of non – radiative recombination times is less dependent on kT to σ ratio. The lower lifetime near band edge energy is determinate by a larger number of localized states. This increase a probability to find a nearly randomly generated NRC, as such increasing tunneling rate. A similar behavior has been observed experimentally in InGaN MQW [74].

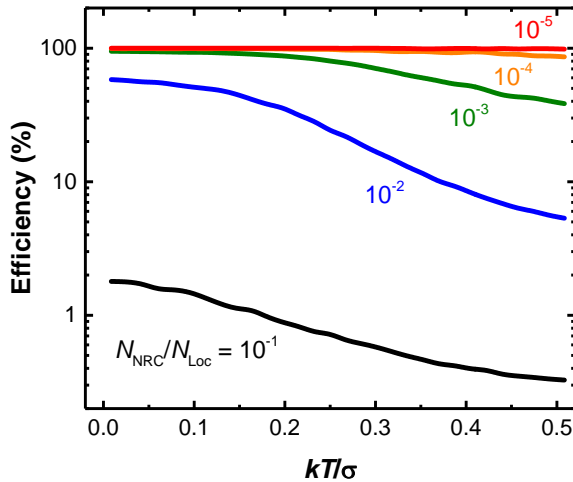


Fig 3.8. Simulated PL efficiency dependence on temperature at different ratios of the density of NRC and localized states. Non – radiative recombination of excitons by tunneling to NRC is taken into account.

Fig 3.9 represents the simulated PL efficiency dependence on temperature at different values of parameter $N_{\text{nrc}}/N_{\text{loc}}$ with both non – radiative recombination mechanisms taken into account. At low temperatures or in the case when the density of localized states is significantly higher than the density of NRC the influence of non – radiative recombination’s is insignificant. This is classical explanation of a high efficiency in III – V nitride compounds: the localized states act as natural barriers preventing the carriers from reaching NRCs. However, with increasing $N_{\text{nrc}}/N_{\text{loc}}$ the peak efficiency of PL begins to decrease.

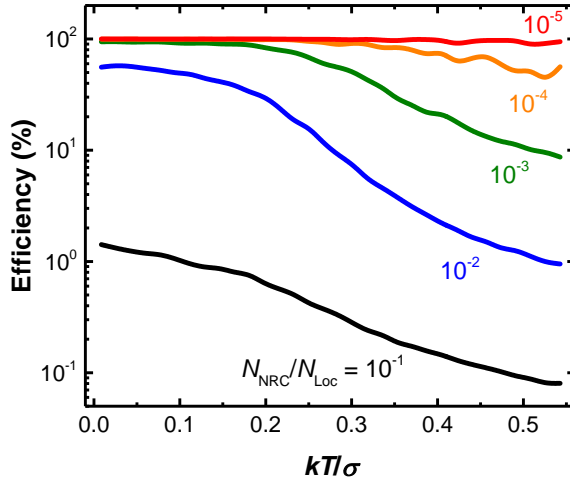


Fig 3.9. Simulated PL efficiency dependence on temperature at different ratios of the density of NRC and localized states. Non – radiative recombination of excitons by both tunneling to NRC and delocalization/capture to NRC are taken into account.

In order to compare simulations with experimental data, the temperature dependence of PL intensity measured under quasi-steady-state excitation is presented for a selected high-Al-content epilayer in Fig. 3.10. The best fit was found to be with the parameter of $N_{nr}/N_{loc} = 0.18$. This value corresponds to a poor quality of the sample. The PL intensity decreases, albeit slowly, already at low temperatures. The decrease becomes substantially faster at elevated temperatures. The total decrease in efficiency is less than an order which could be seen as a good characteristic for nitride compounds, however due low initial IQE it lacks potency for application in optoelectronic devices.

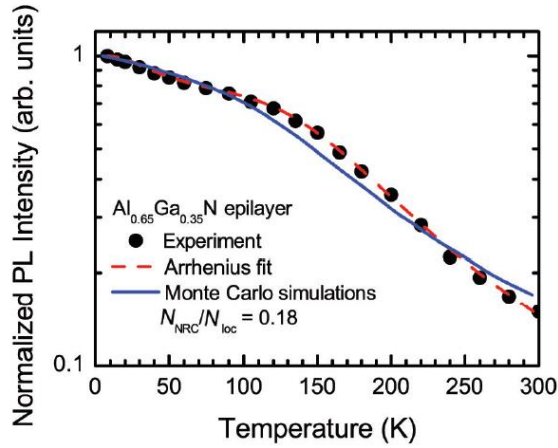


Fig 3.10. Experimental (points) and simulated (lines) temperature dependences of PL intensity in AlGaN epilayer [P3]

The experimental points might be well fitted (see Fig 3.10) using Eq. (1.5) with $i = 2$ implying involvement of two nonradiative channels with activation energies of 6 meV and 69 meV. These channels might be tentatively attributed to the exciton redistribution within localized states and the exciton delocalization to the mobility edge. Despite that the simulated efficiency values fit nice at low and high temperatures there is some mismatch with Arrhenius fit at middle range (around 150 K) which can be caused by change in the dominant recombination mechanism. As seen in Fig 3.11, the proper activation energies could be evaluated only at high densities of NRC. Otherwise, the same Arrhenius fit could not be applied due to high inaccuracy as the non-radiative recombination becomes inferior compared to radiative. Nevertheless, our simulations show that the activation energy E_2 can be attributed to non-radiative recombination by delocalization and capture. Moreover, the lower energy E_1 is clearly defined by tunneling mechanism which is a dominant recombination channel in this particular case. This is because the delocalization/capture events are strongly limited by thermal energy, since the potential fluctuation parameter is usually large III-nitrides. On the other hand, tunneling to NRC is energy independent, and rather affected by the distance between randomly generated localized states and NRC.

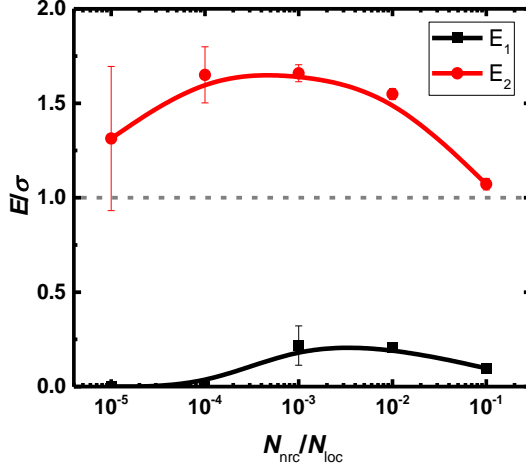


Fig 3.11. Activation energies for two recombination channels as a function of the ratio between the densities of NRC and localized states.

In samples with strong localization, the predominant non-radiative channel is exciton tunneling to NRC, whereas in the samples containing shallow localized states the probability of capture to NRC is much higher. As shown in Fig. 3.12 for the sample with relatively high NRC density, non-radiative recombination becomes the predominant type of events, though it really depends more on the sample properties which define the distribution of NRC and the recombination rates. For this simulation, we took the values previously obtained in fitting the temperature dependence of efficiency. At strong localization and low temperatures, the capture by NRC can be almost neglected, though the impact is nearly the same at elevated temperatures and depends on the ratio between the localization distribution parameter σ and the thermal energy kT . Despite the fact that the Arrhenius parameters are meant to represent separated recombination channels, the combinations of two or more mechanisms will alter the activation energies. Fortunately, our model can be used for the in-depth analysis of the carrier dynamics, as we are not limited by additional broadening of PL band.

Fig 3.12 shows the simulated number of recombination events. As pointed out before, the non-radiative recombination from delocalized excitons at low temperatures is by several orders of magnitude lower. With increasing temperature, the non-radiative recombination will reach the same rate as that of tunneling mechanism.

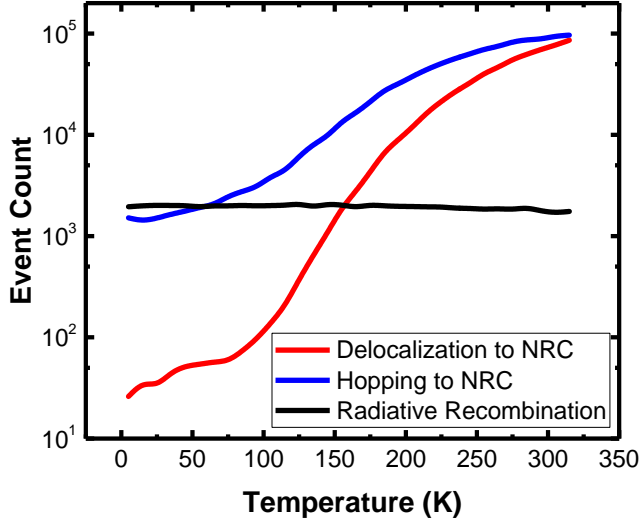


Fig 3.12. Dependence of event rate for specific mechanisms (indicated).

By using the obtained rates of recombination events and taking not into account the energy distribution of localized carriers, we can calculate the dependence of carrier lifetime on energy. Fig 3.13 illustrates the simulated total non-radiative recombination time as a function of energy below mobility edge. Furthermore, as the radiative recombination seems to have no dependence either on energy or on temperature, the overall lifetime of localized carriers should follow the same profile. The lifetime of strongly localized carriers is limited by random distribution of NRC. Therefore, the same energy states could act as the barrier protecting the carriers from reaching NRC or as a strong non-radiative recombination channel. On the other hand, carriers in shallow states tend to be captured by NRC after delocalization. As a result, the slope of the lifetime decrease with increasing carrier energy is defined by thermal energy. The value of near-band-gap recombination mirrors the $N_{\text{nrc}}/N_{\text{loc}}$ ratio.

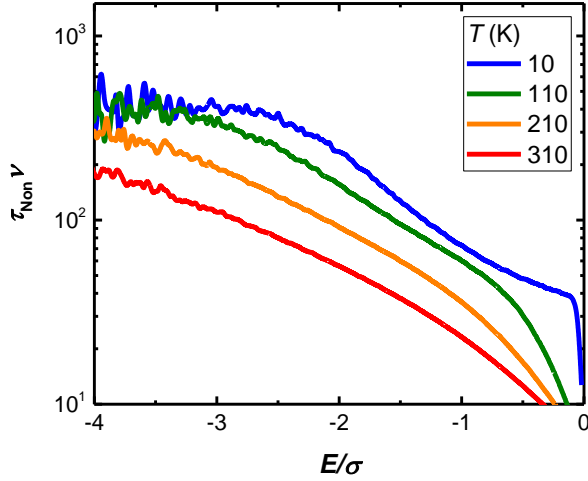


Fig 3.13. *Dependence of lifetime due to non – radiative recombination on energy simulated using parameters obtained by fitting simulated PL intensity with experimental data.*

3.1.4. Conclusions

To summarize, we simulated the dynamics of low-density exciton system using the kinetic Monte Carlo algorithm and calculated the temperature dependence of PL intensity in high-Al-content AlGa_N epilayer to fit it to the experimentally measured dependence. The temperature dependence of the Stokes shift between the mobility edge and the peak position of PL band has been exploited to estimate the parameters necessary for the simulations. The study included two nonradiative recombination mechanisms: recombination via delocalized states and direct tunneling to NRCs. The analysis and subsequent fitting with experimental results revealed the importance of the direct tunneling to NRCs in epilayers with a high ratio between the densities of nonradiative recombination centers and localized states, which might be expected in certain III-nitride epilayers, especially in high-Al-content epilayers. The tunneling to NRCs results in a substantial decrease in the absolute values of low-temperature efficiency and a gradual efficiency decrease with temperature in the range from 8 K to ~100 K. The temperature dependence of the efficiency affected exclusively by nonradiative recombination via delocalized states is negligible in this range for any reasonable material parameters. Thus, the gradual efficiency decrease, which

has been observed in the epilayer used for fitting in this study, has to be attributed to the influence of direct tunneling to NRCs. At temperatures above ~ 100 K, both mechanisms become important for the efficiency decrease with temperature, which can be described by an Arrhenius-type function. However, except for the cases when the tunneling effect might be neglected (at low densities of NRCs), the activation energy extracted from such description of experimental dependence is just an empirical parameter, which depends on the activation energies for both processes.

3.2. Free and localized carrier dynamics in AlGaN

In this section, we will discuss the carrier dynamics in a system consisting of localized excitons and free electrons and holes. Such system usually occurs at high excitation densities and/or elevated temperatures. By exploiting the kinetic Monte Carlo simulation technique, we were able to describe the temperature and excitation intensity dependent behavior of PL band in wide – band - gap AlGaN QW structures with strong carrier localization. The simultaneous fit of these dependences has been used as a figure of merit for validation of the model and the parameters used in the model. The simulations enabled us to reveal the importance of specific carrier migration and recombination mechanisms for the dynamics of the coupled system of free and localized carriers in a wide temperature range. In particular, it is shown that the efficiency droop at elevated excitations in AlGaN QWs used for fitting in this study can be caused by peculiarities of carrier localization without a significant contribution of the Auger processes.

3.2.1. Experimental details

In this section, we study the dense carrier system containing significant fractions of both localized and free carriers. The calculation results are compared with the experimental results on PL properties of AlGaN/AlGaN MQW structure exhibiting strong carrier localization. The AlGaN/AlGaN MQWs were grown by migration-enhanced metalorganic chemical vapor deposition (MEMOCVD®) technique on a c-plane sapphire substrate. Ten pairs of 5.0 nm thick $\text{Al}_{0.35}\text{Ga}_{0.65}\text{N}$ quantum wells separated by 11.5 nm thick $\text{Al}_{0.49}\text{Ga}_{0.51}\text{N}$ barriers were grown on a 1.2 μm thick n- $\text{Al}_{0.55}\text{Ga}_{0.45}\text{N}$ buffer layer.

The PL spectra were measured under excitation power density varied from 0.4 kW/cm^2 to 14 MW/cm^2 at different temperatures from 8 K to 300 K. The 4th harmonic (266 nm) of the Q-switched YAG:Nd laser radiation (pulse duration 4 ns) was used for excitation under quasi-steady-state conditions. A closed-cycle helium cryostat enabled the variation and stabilization of temperature. The PL signal was analyzed by a double monochromator (Jobin Yvon HRD-1) and detected by a UV-enhanced photomultiplier.

3.2.2.Simulation details

The simulations of carrier dynamics using the model we developed in this work require many material parameters and several assumptions on the processes of importance. To make the fitting of experimental and simulated results more reliable, we simultaneously fitted two groups of experimentally obtained dependences: i) temperature dependences of PL efficiency, PL band peak position, and PL band width measured at fixed (low) excitation power density; and ii) PL efficiency dependences on excitation power density measured at different temperatures. These dependences are commonly used to evaluate various material parameters. The band peak and FWHM dependences were partly discussed in section 3.2.1. The PL efficiency dependence on temperature is usually exploited for the estimation of the IQE under assumption that the efficiency is 100% at low temperatures, even though this assumption is not always correct, as shown in [19][75] and discussed in section 3.2.1.

To simulate the carrier dynamics at higher excitation densities, we use multi-particle kMC algorithm. The main difference from previous model is, as the name suggest, simultaneous calculation of various numbers of particles (typically in range from 1 to 10^5). Due to the large number of particles requiring time step updates, several modifications were made to simplify calculations. The localization rate is assumed to depend on the spatial distribution of unoccupied localized states. Furthermore, for the localization process to occur, both free electron and hole have to be present near a localized. Meanwhile, nonradiative recombination process was adjusted to reflect the ability of carriers to stay in free state. To the contrary to single particle simulations where free carriers have insignificant influence on PL spectra, the time a particle rests in free state is skipped in these calculations. This issue is discussed in more details in Section 2. Additionally, to compare the results with experimental data, further calculations were simulated under quasi-stationary excitation regime. The simulation time is selected to be long enough to ensure that the system stays in equilibrium state. Such upgrades allow us to study the carrier dynamics at high excitation intensities.

3.2.3.Simulation of PL spectra

It is well known that the emission peak in III-nitride LED devices depends on excitation power [76]. The filling of localized states is suggested as the fundamental mechanism behind this effect. The main optical properties in

such device are defined by the recombination of localized carriers. As follows, we seek to find out how the carrier density affects the PL shape. Figure 4.1 represents typical simulated PL spectra of AlGaN MQWs at different carrier densities. A low temperature of 10 K was selected for this purpose since the influence of localization decreases at elevated temperatures. At low excitation (in the range of carrier density of 10^{15} - 10^{17} cm^{-3}), the PL spectra stay almost unchanged and exhibits the same band shape behavior as that obtained in our single-particle simulations.

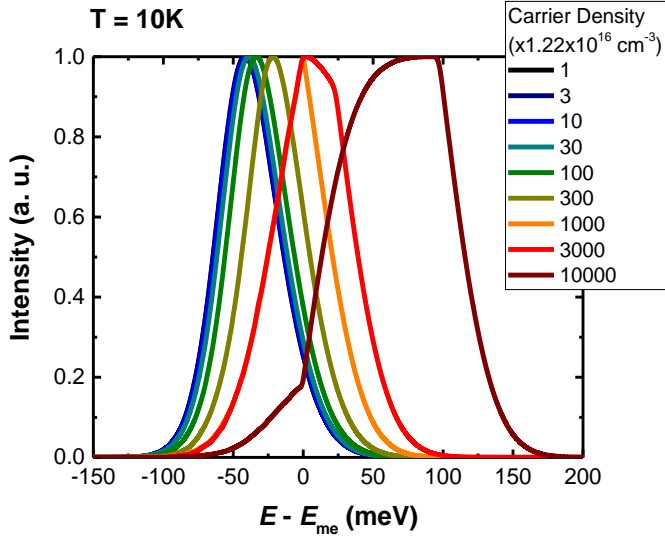


Fig. 4.1. PL spectra of AlGaN MQWs at different carrier density simulated at 10K temperature.

With increasing of carriers density, the PL peak positions move towards the mobility edge. At the same time, the low-energy tail becomes more pronounced following the energy distribution of localized states. With the rise in the density of holes and electrons, the population of localized states reaches limits, and the carriers start to occupy free band states. With increase of the free carrier density above the density of localized states ($>10^{19}\text{cm}^{-3}$ for these simulations) the PL peak moves above the mobility edge and the band-to-band recombination is enhanced. The abrupt feature in the calculated PL bands at $E = E_{me}$ is attributed to a join point of different distributions of states (Gaussian-like and Heaviside-theta for localized and 2D free states). Finally, the high-energy slope depends on free carrier energy distribution which is described using the Fermi - Dirac function. The PL band shape could be further affected by additional effects, such as LO phonon scattering.

In III-nitrides, it is also possible to observe stimulated emission [77], however, this phenomenon occurring at especially high carrier densities, is out of scope of this study. Note that such high carrier densities are hard to reach due to substantial losses due to nonradiative recombination of free carriers. Figure 4.2. shows an example of the band of simulated PL (black line) at 150 K. Here, blue and red lines represent energy distributions of localized and free carriers, respectively (normalized to the maximum total carrier density). As seen in Fig 4.2., despite that the free carrier density is larger than the density of localized ones, they have smaller influence on PL band. The calculated PL lifetime (dashed green line) decreases drastically above the mobility edge. Though the influence of bimolecular recombination increases, the radiative recombination of localized carriers remains the predominant recombination mechanism. Furthermore, the high nonradiative recombination from free carriers additionally lowers the PL lifetime. Such behavior is usually explained by the ability of localized states to prevent the carriers from reaching the nonradiative recombination centers.

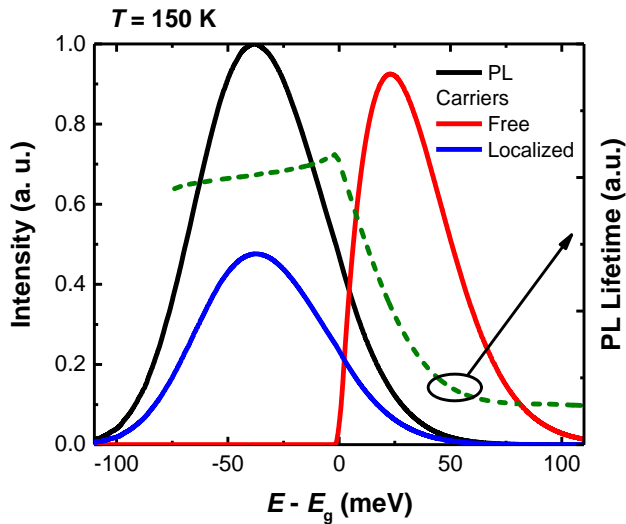


Fig 4.2. Simulated PL spectra (black), distributions of free (red) and localized (blue) carriers, and PL lifetime (dashed line).

The comparison of the calculated results with the experimental PL spectra enables revealing certain conditions for strong localization. First of all, the linear radiative recombination at a high density of localized states should surpass the band-to-band recombination. Otherwise, more than one peak should be present in PL spectra. The absence of the second PL peak at higher

excitation densities indicates the main non-radiative recombination mechanism is the capture of free carriers by NRC. This feature is studied in more detail below.

As said before, the PL shape behavior is mostly determined by the lifetimes of free and localized carriers and the ratio between the density of nonequilibrium carriers and the density of localized states. In order to obtain the values of the parameter of interest, we perform the same procedure as before: we fit the simulated PL spectra with the spectra experimentally obtained at low excitation regime. The starting point in the simulations of PL properties is reproducing the PL spectrum at the conditions corresponding to those in experiment. We repeat similar procedures as described in section 3 to simulate PL temperatures dependences. Following results were obtained using quasi -steady-state excitation regime the generation of nonequilibrium carriers occurs randomly through the entire period of simulation, in contrast to the calculations described above, when the nonequilibrium carriers were generated only at starting the calculation, at time $t = 0$.

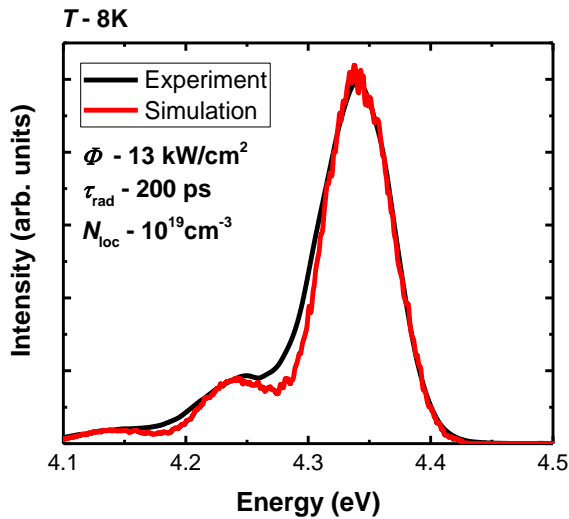


Fig 4.3. Experimental (black) and simulated (red) PL bands in AlGaIn MQWs at 8 K.

The PL spectra measured at low temperatures have a Gaussian-like band with strongly expressed LO phonon replicas, as shown in Fig. 4.3. At elevated temperatures, the phonon replicas become less distinct due to homogeneous thermal broadening [see Fig. 4.4]. At low excitations, the high-energy slope of the PL band is governed only by the distribution of localized states and

exhibits no change with increasing excitation, whereas at high carrier densities, the slope is also affected by the free carrier distribution. Moreover, the increasing excitation results in free carrier heating, which also changes the high-energy slope of the PL band. The typical experimental and simulated PL spectra are compared for the temperatures of 8 K and 300 K in Fig. 4.3 and Fig 4.4, respectively. Meanwhile, the band gap shrinkage was evaluated by the Varshni formula with parameters $\alpha = 1.04$ meV/K and $\beta = 888$ K [78] and the band gap energy of 4.417 eV at 0 K.

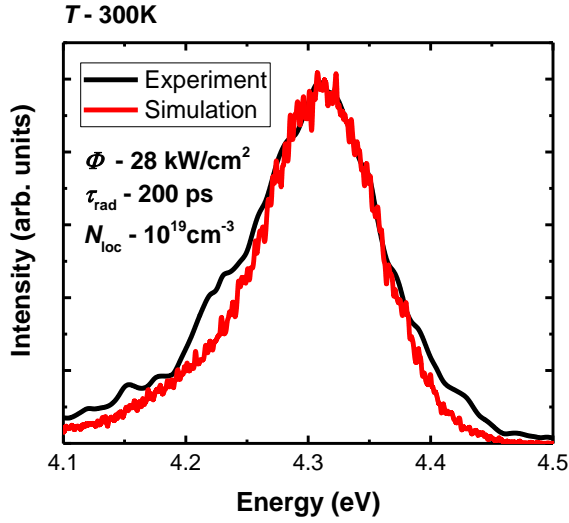


Fig. 4.4. Experimental (black) and simulated (red) PL bands in AlGaIn MQWs at 300 K.

Measured PL Stokes shift energy is shown by filled points in Fig. 4.5. The initial flat region stretches up to 120 K followed by a rise in energy towards the mobility edge. Such behavior is typical for ternary III-nitrides and indicates carrier (exciton) redistribution through the localized states [4][5][37]. The high - temperature region of the peak position dependence can be adequately described by the Eliseev formula, as shown by the dashed line in Fig. 4.5, which provides the localization parameter $\sigma = 30$ meV. Finally, we achieved the best fit of the simulated PL band peak positions with experimental data for parameter $\nu_0\tau_0$ and $N\alpha^3$ equal to 200 and 0.082, respectively. Compared to previous sample, $\nu_0\tau_0$ value is considerably lower which might be considered as an indication of higher efficiency. The value of $N\alpha^3$ remains almost the same as in bulk crystal, in spite that the nonequilibrium carriers in MQWs are confined in one direction. It is worth also noting that

the fit of simulated results with the experimental data is fairly good in the entire temperature range.

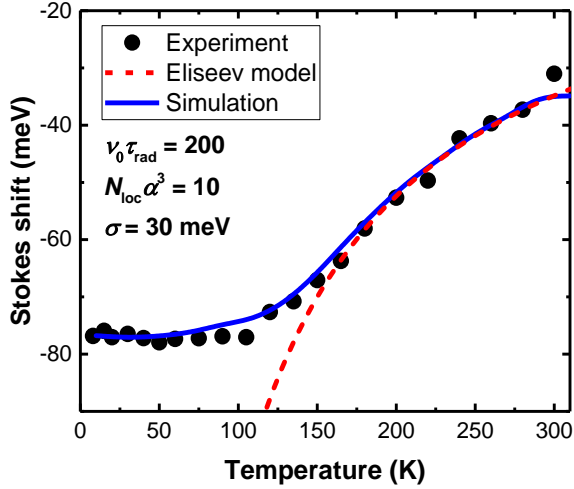


Fig 4.5. Temperature dependence of the PL band peak energy in AlGaIn MQWs obtained experimentally (points) and calculated using the current MC simulation (solid blue line) and by using Eliseev model (dashed line).

The measured temperature dependence of the PL band width is shown by points in Fig. 4.6. It exhibits a W - shaped behavior, as is usual at the strong influence of carrier localization [18][21][79]. The PL band width varies little below 60 K, rises with temperature until ~ 160 K, remains constant until ~ 200 K, and increases again at higher temperatures. The first major increase in PL band width is caused by increasing ability of localized carriers (excitons) to occupy higher energy states. The kink at ~ 160 K represents a crossover from a nonthermalized to a thermalized energy distribution of the excitons, whereas the constant band width above the crossover is an indication that a thermalized exciton energy distribution is established. Finally, the second increase in PL band width at elevated temperatures is due to strengthening carrier-phonon interaction. The blue line in Fig 4.6 shows simulated PL FWHM and red line represents simulated FWHM with additional broadening effects. To begin with, there is a constant shift in peak width attributed to double-scaled potential fluctuations. The energy dispersion parameter Γ is found to be 27 meV. With increase in temperature phonon-assisted band broadening increases. The best fit is obtained at the coupling strength

parameters with acoustic phonons $\beta = 0.04$ meV/K and LO phonon $\gamma = 0.75$ eV (for $E_{LO} = 98$ meV).

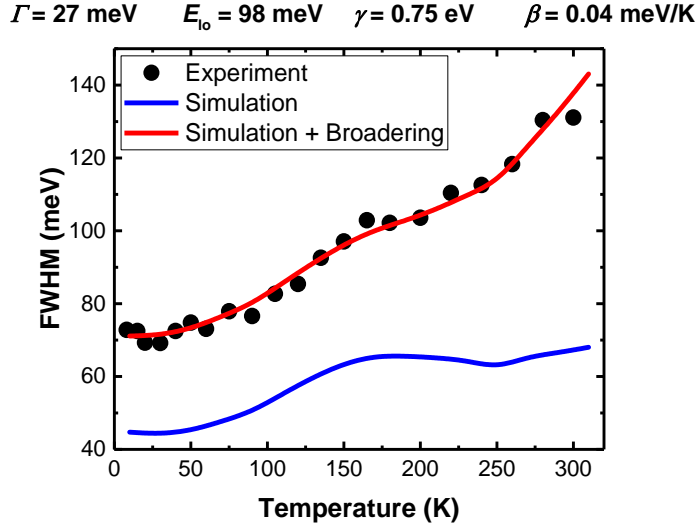


Fig 4.6. Temperature dependence of the PL band FWHM in AlGaN MQWs obtained experimentally (points) and calculated without (blue line) and with (red) broadening taken into account.

The next step is modeling the temperature dependences of the PL efficiency. Using similar procedures as in section 3, we simulate PL efficiency under low excitation (Fig 4.7). PL intensity is almost constant at temperatures below ~ 40 K and decreases by two orders of magnitude as the temperature is increased up to room temperature. The solid line in Fig. 4.7 represents the simulated dependence, which fits well. The modeling revealed that the IQE equals $\sim 90\%$ at low temperature and decreases down to less than 1% at room temperature. The PL efficiency decrease with temperature is caused by the increasing fraction of free carriers and by an increasing rate of nonradiative recombination.

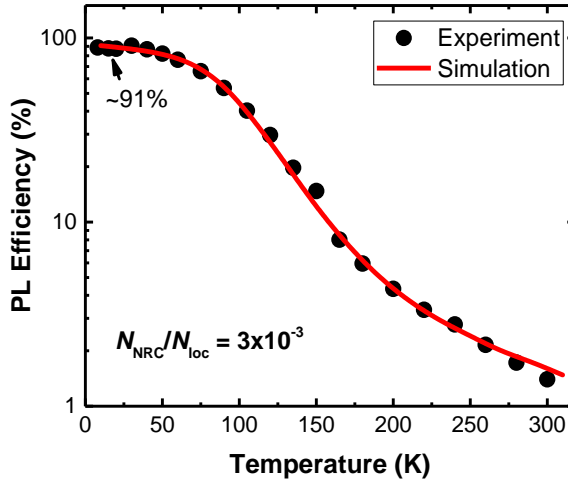


Fig 4.7. Experimental (points) and simulated (line) dependence of PL intensity on temperature in AlGaIn MQWs.

The obtained parameters were used for further simulations and evaluation of efficiency dependence on excitation power density. Unfortunately, such procedure does not guarantee the exact set of parameters for the material under study. The evaluated values are calculated by assuming that the density of free carriers is negligible, and the recombination channels of localized carriers dominate. None of this assumption is 100% certain for material under study. Nevertheless, there is little to no ways to accurately estimate these values from the experimental results. Thus, fitting the additional experimental data of PL efficiency under different excitation conditions would provide strong verification of obtained parameters.

3.2.4. PL Efficiency simulations

As a final simulation, the excitation power density dependences of PL efficiency at different temperatures were calculated by taking into account the localizing potential landscape. Therefore, the rate of recombination processes heavily depends on carrier density and temperature. The PL efficiency was calculated as the ratio of spectrally-integrated PL intensity and excitation power density. The experimental dependences (depicted by points in Fig 4.8. have two regions: a region of weak increase at low excitation power densities and the droop at elevated excitations. The droop onset shifts to lower excitation intensities as the temperature is decreased. The solid lines in

Fig. 4.8 represent the simulated dependences, which quite adequately follow the experimentally observed behavior for the selected value of localized state density $N_{loc} = 10^{19} \text{ cm}^{-3}$. The simulation shows that there is no single parameter which solely describes any particular part of the dependences. All the recombination or transport mechanisms are tied together. Hereby, for the future discussions we will have estimate two parameters: the hard-set value which corresponds to equations in section 2 and the actual value obtained from the simulated data.

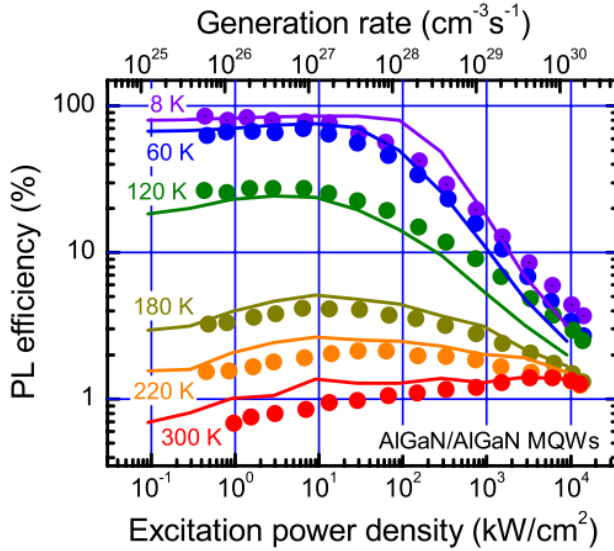


Fig 4.8. Experimental (dots) and simulated (lines) dependences of PL efficiencies on excitation power density at different temperatures [P1].

The initial increase of PL efficiency is usually attributed to several effects: the saturation of NRCs, the increasing role of radiative bimolecular recombination due to filling of localized states, and the screening of built-in electric field in QWs [19][80]. The efficiency droop is also assigned to several competing mechanisms with Auger recombination and carrier delocalization being the most important [81]. In order to understand the primary mechanisms behind the efficiency behavior, we studied the carrier dynamics. Fitting experimental data allows us to obtain the constant lifetime values for the single process but does not represent how this specific recombination will behave in presence of multiple transition channels. Besides the different processes have different dependence on excitation and temperature. This heavily affects the

theoretical description of carrier dynamics in nitride compound with strong localization. The main advantage of our simulation is the ability to see real-time values of each recombination mechanism. Below, we discuss most significant processes for free and localized carriers.

Figure 4.9. shows the simulated lifetime values of radiative recombination event for localized carriers. The points represent the obtained values, whereas the lines are obtained by smoothing the dependences and are provided as the guide for eye.

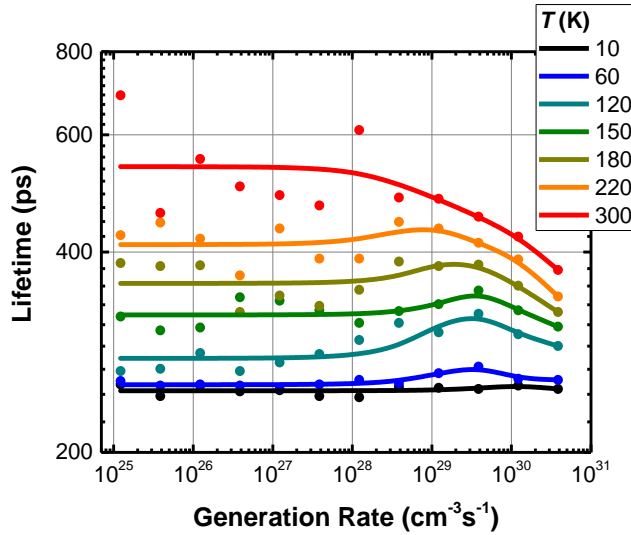


Fig 4.9. Dependence calculated radiative recombination lifetime of localized carriers on generation rate at different temperatures.

As seen in Fig 4.9., the mean lifetime of radiative recombination process increases with increasing temperature. Such behavior is caused by other two competing mechanisms: hopping and delocalization. Both of them depend on temperature. At low temperatures, their impact on the lifetime can be neglected. At elevated temperatures, the situation gradually changes, and they become the dominant processes affecting the recombination rates. There is a difference between used parameter $\tau_{\text{rad}} = 200$ ps and obtained low temperature value of radiative recombination lifetime ~ 245 ps. Such gap can be attributed to localization as the mean time of carrier capture by localized states vary around 40 ps. The increase of lifetime values with the increase of generation rate can be explained by a limited number of localized states. At significant filling of localized states, the hopping probability reduces, since the exciton can jump only to an empty state. Finally, there is a small increase in lifetime

around the generation rate of $10^{28} - 10^{29} \text{ cm}^{-3}\text{s}^{-1}$. As already shown in Fig 4.1., the mean energy of excitons increases with increasing density of generated particles. As a result, the difference between the exciton energy and the mobility edge decreases and causes an increase in the delocalization probability. The generation rate value corresponding to this increase depends on the ratio between the equilibrium carrier density and the density of localized states.

On the other hand, the nonradiative recombination of localized carriers for this sample found to be inferior compared to other mechanisms. Starting from low temperatures the hopping to NRC is almost negligible. The lifetime corresponding to this process is extremely large, exceeds 10^4 ps. Even at excitation or temperature conditions favorable for exciton hopping to NRC, this effect is overshadowed by the capture of free carriers to NRC. At elevated temperatures or high carrier densities, this mechanism can serve as an effective recombination channel with a lifetime of around 300 ps, which is comparable to the lifetime of radiative recombination. Such value could have a substantial impact. However, these conditions correspond to the situation when a major part of nonequilibrium carriers are free, thus the contribution of localized excitons is small due to their small relative density.

The capture of free carriers by NRC is a main mechanism of carrier non-radiative recombination under all excitation conditions. The simulated values of nonradiative recombination lifetime for free carriers as a function of generation rate is presented in Fig 4.10. The corresponding behavior of nonradiative recombination is qualitatively different in two cases: before and after overpopulation of localized states. The first case represents the conditions when the overall recombination of localized carriers occurs faster than new particles are generated. The nonradiative lifetime of free carriers has no dependence on carrier density. The governing factor affecting the behavior of nonequilibrium carriers in these conditions is electron and hole thermal energies. At low temperatures, the carriers are bound to excitons before reaching NRCs. At elevated temperatures the probabilities delocalization and following capture by NRC increase, so recombination lifetime decrease. This reduce in lifetime is governed by values of σ/kT and $N_{\text{nrc}}/N_{\text{loc}}$.

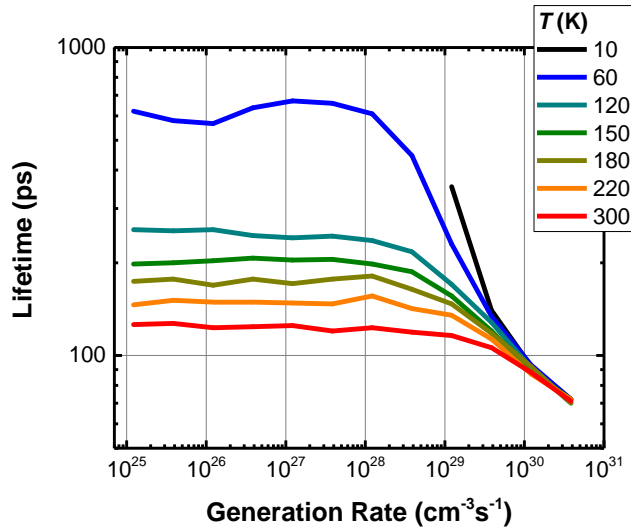


Fig 4.10. Dependence calculated nonradiative recombination lifetime of free carriers on generation rate at different temperatures.

The second case of lifetime behavior corresponds to higher generation rates when the system consists nearly fully occupied localized states. Having no localized states to occupy, a large part of generated electron-hole pairs is captured by NRC. The NR lifetime consist of particles that escaped localized state and was captured by NRC and the free carries which was captured directly. With increase of generation rate, the fraction of later ones rises, thus the obtained recombination rate moves towards its original ν_{cap} value. At highest excitation the non-radiative recombination of free carriers become predominant effect. In such conditions dependence on temperature blurs out. Our model does not include the effect of overfilling of NRC, but in the range of simulated density of free carriers such effect shouldn't have strong influence.

Both for efficiency increase and decrease, the main factor governing the PL efficiency is the ratio between the densities of localized and free carriers: the free carriers recombine radiatively via the more effective bimolecular-type transitions, however, are vulnerable to nonradiative recombination, meanwhile, the rate of nonradiative recombination of localized carriers is lower but their radiative recombination is linear. This ratio depends on the landscape of localizing potential. Recently, we proposed a parameter, which reflects the ability of localized carriers to be delocalized and migrate and determines the droop mechanism. However, this parameter does not provide the details on the contributions of different mechanisms. The simulated

excitation and temperature dependences of the ratio between the densities of localized and free carriers are presented in Fig. 4.11. As evident in the figure, the carriers are mostly localized at temperatures below 100 K. Only at elevated excitations, when the localized states start saturating, the free carriers become a dominant fraction. Furthermore, at low excitations, the fraction of localized carriers increases with excitation even at temperatures as high as 300 K.

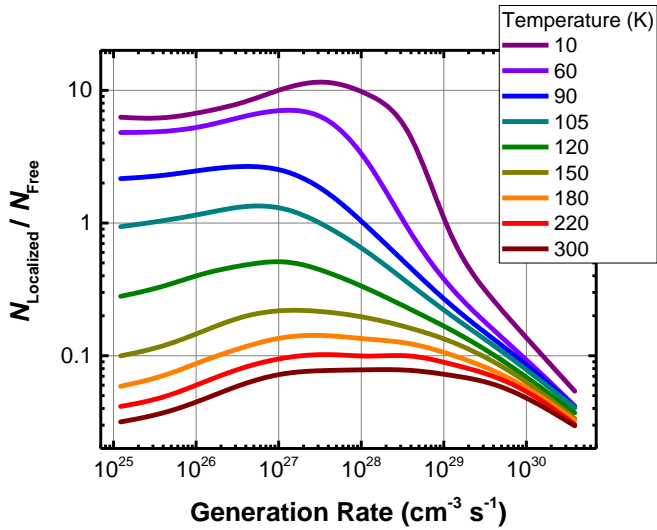


Fig 4.11. Simulated dependences of the ratio between the densities of free and localized carriers at different temperatures.

All the data discussed above imply that the major contribution to photon generation is from localized carriers (excitons) even at room temperature and high generation rate. Despite the considerable increase in free carrier density at elevated excitations, the dominant nonradiative recombination ensures that the role of bimolecular recombination remains smaller than that of the radiative recombination of localized carriers. The PL efficiency dynamics reflects the changes in the relative rates of recombination due to these mechanisms.

Summarizing, we can separate the efficiency dependence on generation rate (Fig 4.8) to four regions which are represented schematically in Fig 4.12. Each area highlights the conditions in terms of generation rate and efficiency favorable for prevalence of certain recombination mechanism or dominance of other effects determining the carrier dynamics.

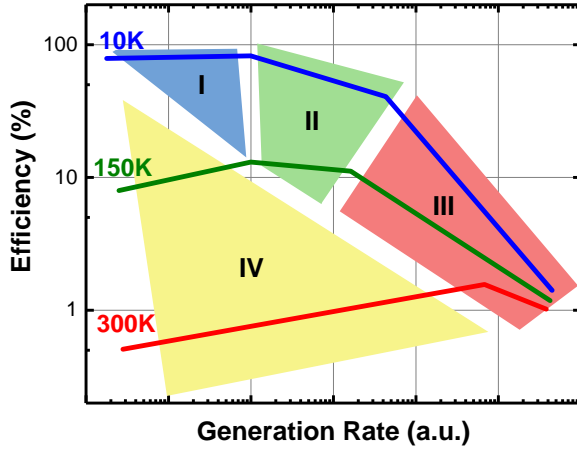


Fig 4.12. Schematic illustration of the areas in PL efficiency versus carrier generation rate plot corresponding to specific dynamics of nonequilibrium carriers [P1].

Area I. At low temperatures and carrier densities, almost all carriers are localized at the lowest energy states. Free carriers can occur for a short period of time. Since the thermal velocity of generated electron-hole pairs at these conditions is low, they stay in a close vicinity of each other and have a high probability be captured again. Furthermore, the slow particle transport strongly decreases the probability of non-radiative recombination as long as the main recombination mechanism is the capture by NRC and subsequent nonradiative recombination. In these conditions, PL spectra are completely determined by the recombination rate of localized excitons and the rate of carrier hopping. The IQE is high, weakly depended on temperature and is predominantly limited by the ratio between capture to localized states and NRCs. A higher density of localized states as well as a shorter radiative recombination time extends this area towards larger generation rates, whereas an increase in the localization parameter σ allows observing this area at higher temperatures.

Area II. The efficiency droop emerges due to the non-radiative recombination of localized carriers as a result of both the decrease in unoccupied localized states and the increase of carrier thermal energy. Though the fraction of free carriers starts increasing, it remains substantially smaller than the fraction of localized carriers. The onset of area II indicates the enhanced ability of localized carriers to reach NRCs. The rate of the enhancement with increasing carrier density depends on the density of NRCs.

The fitting within this area is rather challenging, since the distribution of state density in the energy range between localized and free states is not known well. This uncertainty is reflected in the mismatch of between simulated and experimentally measured efficiency (Fig 4.8) at low temperatures. Here even a small change in energy of several meV leads to a substantial change in the ratio of the densities of free and localized carriers and has a strong influence on PL efficiency.

Area III. This area corresponds to the efficiency droop. The lack of unoccupied localized states as well as an increase in thermal energy of localized carriers leads to a rapid increase in the fraction of the particles captured by NRCs. The onset of this area is defined by the density of localized states and the mean lifetime of localized carriers. It is worth noting that the rate of the band-to-band radiative recombination is still lower than the rate of the radiative recombination of localized carriers and is also lower than free carrier non-radiative recombination. In such conditions, the distribution of localized carriers completely follows the distribution of localized states. The PL band is broadened and is weakly affected by temperature or excitation intensity.

Area IV. The influence on IQE by free electrons and holes is of the same order of magnitude as the influence of localized carriers. The rise in PL efficiency with increasing excitation density is attributed in this area to enhanced localization. The localization probability increases with increasing density of nonequilibrium carriers, electron and hole have increasing probability to simultaneously appear near a localized state and become localized. However, the localization probability decreases as an increasing part of the localized states become populated. The carrier dynamics in this area depends on the competition of these two processes.

3.2.5. Conclusion

Kinetic Monte Carlo simulations applied for the system consisting of localized and free nonequilibrium carriers enables evaluating the contributions and rates of the main processes determining the efficiency droop, temperature dependence of luminescence efficiency, and the temperature dependences of luminescence band parameters. It has been shown that the efficiency droop in such a system can be interpreted without significant influence of Auger recombination and is mainly determined by the peculiarities of carrier localization. The droop effect is attributed to the transition of the system of nonequilibrium carriers from the state with the

dominant light emission from strongly localized states with weak nonradiative recombination to the state of predominantly free carriers with a high rate of nonradiative recombination and still a low rate of radiative bimolecular recombination. Excellent agreement between theoretical simulations and experimental data was obtained by employing the developed model for AlGaIn epilayers with high density of localized states. The model and simulation procedures are applicable for analysis of carrier dynamics in any materials, where localized and free carriers coexist.

3.3. Diffusion in a common system of free and localized carriers in InGaN

The diffusion coefficient provides an important information on the carrier localization in ternary III-nitride compounds AlGaN and InGaN. The carrier dynamics in such materials is strongly affected by the randomly fluctuating potential landscape experienced by the carriers. The diffusivity of holes is difficult to measure by electrical methods, but it can be studied using optical techniques. The diffusivity changes with increasing photoexcitation non - monotonously, this dependence being different in thick and thin layers. In this section, we present the results obtained by using theoretical and kinetic Monte-Carlo approaches to simulate the diffusion coefficient dependence on photoexcited carrier density in InGaN MQWs. The obtained results are compared with the experimentally measured data. Furthermore, we demonstrate how the potential disorder impacts the carrier diffusivity at both low and high carrier densities.

3.3.1. Experimental details

Two samples used in this work will be further referred to as "*c*-plane sample" and "*m*-plane sample". Both structures were grown by metalorganic chemical vapor deposition. The *c*-plane sample was deposited on *c*-plane sapphire substrate followed by a 3 μm -thick GaN buffer layer without intentional doping. Ten pairs of 3 nm-thick $\text{In}_{0.1}\text{Ga}_{0.9}\text{N}$ quantum wells and 5 nm-thick GaN barriers were deposited on top of this template. 2 nm of each barrier was additionally doped with silicon to the density of 10^{17} cm^{-3} . The entire structure was protected by an 8 nm GaN cap layer. The *m*-plane sample was grown on a *m*-plane GaN substrate with a -1 degree miscut towards the [0001] direction. A $\sim 1.2\ \mu\text{m}$ -thick Si-doped GaN buffer layer homoepitaxially grown on the substrate, was followed by 3 periods of 8 nm-thick $\text{In}_{0.13}\text{Ga}_{0.87}\text{N}$ quantum wells separated by 9 nm-thick GaN barriers. On top, a 7.5 nm $\text{Al}_{0.22}\text{Ga}_{0.78}\text{N}$ electron blocking layer and 143 nm *p*-doped GaN cap layer were deposited.

The light-induced transient grating (LITG) technique was used to measure the ambipolar diffusion coefficient D and the carrier lifetime τ in different directions and at various excitation intensities [82]. In the LITG experiment, an interference pattern of two laser beams is used to create in a sample a spatially periodic distribution of nonequilibrium carriers. The experimental setup was based on PHAROS (Light Conversion) laser, which emits 250 fs

duration pulses at a fundamental wavelength of 1030 nm at a 30 kHz repetition rate [83].

3.3.2. Simulation of diffusion

Figure 5.1. shows the experimentally measured diffusion coefficient D as a function of photoexcited carrier density N in m - plane sample along a and c directions, and in c -plane samples. In c -plane structure, the diffusion coefficient is constant at the value of approximately $D = 0.7 \text{ cm}^2/\text{s}$ at low densities and starts to increase with the excitation above $N = 4 \times 10^{18} \text{ cm}^{-3}$. For m - plane sample, the diffusion coefficient behaves differently: it has unexpectedly high values ($D_{\parallel a} = 8 \text{ cm}^2/\text{s}$ and $D_{\parallel c} = 2 \text{ cm}^2/\text{s}$ at $\sim 10^{18} \text{ cm}^{-3}$) at low excitation intensities, decreases with increasing excitation till the minimum value at $N \sim 10^{19} \text{ cm}^{-3}$, and begins growing afterwards. Note that the reported low - density D value is around 1 - 2 cm^2/s in bulk c - plane GaN [84][85]. We observe that the ratio between the D value in the main orthogonal directions remains approximately constant within the entire density range, which suggest that diffusion along those directions is governed by hole transport with different effective masses. While the dependence $D(N)$ in c -plane sample resembles those observed in other polar InGaN quantum well structures [86], the behavior revealed in m -plane sample has not been reported before. To better understand the processes behind it, we separately analyze the "low density" region, where $D(N)$ decreases with density, and the "high density region", where D grows with excitation.

The lines in Fig. 5.1. represents the results of our first attempts to model the diffusion coefficient dependence on carrier density. For the calculations, we used the general Einstein equation with additional correction for localization [69], as described in detail in section 2. The obtained values fit well for c - plane sample (blue line). The low diffusion coefficient D_0 was found to be $0.09 \text{ cm}^2/\text{s}$. The density of localized states was set at $2 \times 10^{18} \text{ cm}^{-3}$, whereas the Urbach energy was estimated to be $E_U = 70 \text{ meV}$. However, this model could not properly describe the behavior of diffusion in m -plane sample (red and black lines). The mass parameter along a and c axes was set as 0.38 and 1.91, respectively. The best fit was obtained with the initial diffusivity value of $0.29 \text{ cm}^2/\text{s}$, $N_{\text{loc}} = 10^{19} \text{ cm}^{-3}$ and $E_U = 65 \text{ meV}$.

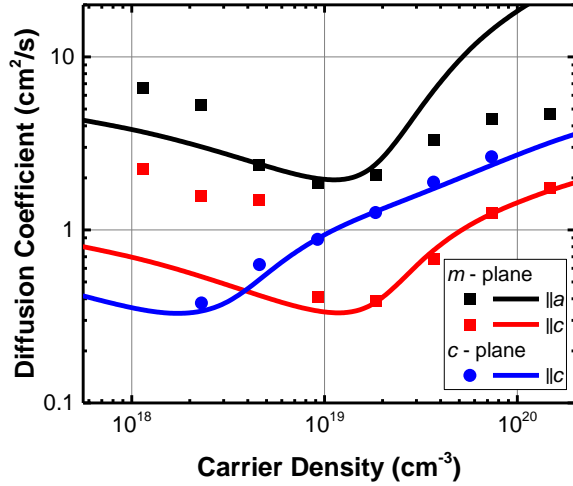


Fig 5.1. Measured diffusion coefficient in InGaN MQWs as a function of photoexcited carrier density in *m*-plane sample along the crystallographic axes *a* (black squares) and *c* (red squares), and in *c*-plane sample (blue circles). Solid lines show the fits obtained by simulations.

The equation 2.23 fails to explain the sharp decrease in diffusion at low excitation. Furthermore, there seems to be additional effects affecting the carrier diffusion at higher excitation, since the increase is different for light and heavy holes. The main problem with this model is its strong dependence on the ratio between free and localized carriers. For the calculations, we assume that the electron-hole pairs are localized instantaneously. The results show that considering the rates of transitions between free and localized states are important for a better fit of calculation and experimental results. On the other hand, the obtained values of the density of localized states and the Urbach energy could be used as the initial values for our kMC simulations.

3.3.3. Simulation of diffusion using Monte – Carlo method

In order to simulate the diffusion coefficient dependence on photoexcited carrier density, we use adjusted kMC model described in sections 3 and 4. The calculations were performed at pulsed particle generation regime, as exploited in experimental setup. The range of the densities of generated particles varied from 10^{18} to 10^{20} cm^{-3} and the maximum calculation time was limited to 10 ns with 10 cycles for each point. Such procedure results in a total of 1×10^6 - 3×10^8

updates for the system providing enough data to obtain reliable results. Note that the lower number of cycles compared to previous calculations is compensated by the larger amount of generated electron-hole pairs. The simulations were applied for m -plane InGaN MQWs with high a potential fluctuation parameter σ and at room temperature satisfying the condition $\sigma \gg k_B T$. Another peculiarity of calculation conditions is a high thermal velocity of free carriers. Particles can move for distance by orders of magnitude farther than the localization radius (for finite localization times). This leads to the situation when single free electrons and holes are spatially separated most of the time. Such assumption could help us to further decrease the calculation time of localization rates. Basically, we use same expression as in section 3.2, assuming that free electrons and holes are randomly displaced in space due to large thermal velocity:

$$v_{loc} = \begin{cases} v_0 \frac{p}{N'}, & \frac{p}{N'} < 1 \\ v_0 & , \frac{p}{N'} \geq 1 \end{cases} \quad 3.1.$$

where v_0 is the initial localization rate and p is the number of free holes. The ratio p/N' reflects the probability for electron to find an unoccupied localized state and free hole at same space cell. At low excitation, the localization rate is lower since free holes and electrons are spatially separated. With increasing particle density, the probability for both electron and hole to be at proximity to localized states increases, thus the limitation for localization disappear.

In this simulation, we predominantly focus on carrier diffusion. Thus, the lifetime and the distance from initial spawn coordinates for each particle is registered. Using this data, the diffusion coefficient is calculated as:

$$D = \frac{\hat{L}^2}{\hat{t}} \quad 3.2.$$

As starting point for further simulations, we observe the diffusion coefficient behavior at two extreme cases. Figure 5.2. shows the values of diffusion coefficient obtained with free only and localized only carriers at different nonequilibrium carrier density. In case without localized states, the diffusion is mainly limited by carrier recombination rates. We assume carrier mean path is defined by thermal velocity. With typical lifetime of 400 ps simulation reveals the value of diffusion coefficient near $10 \text{ cm}^2/\text{s}$. At low carrier densities, the diffusion stays constant. With rising free carrier band-to-

band recombination rate both mean path and lifetime decrease. These effects will be neglected in our simulations since the calculations are performed at carrier densities lower than those sufficient for these effects to be important.

The blue line in Fig. 5.2. represents the diffusion coefficient calculated with only excitonic propagation through localized states. The value obtained at low excitation $D \approx 10^{-2} \text{ cm}^2/\text{s}$. At elevated exciton densities it drops to $10^{-5} \text{ cm}^2/\text{s}$ due to state filling. The main mechanism behind such low value can be attributed to fairly large potential fluctuation dispersion parameter. The value of $kT/\sigma \approx 0.3$ characterizes the system of localized carriers as close to the lowest energy (see Fig. 3.2.). At these conditions, carriers are deeply localized and the nearest other localized states with similar energy are located far away (distributed due to a random Gaussian distribution). Thus, despite a comparably fast transition rate, the excitons tend to move around states within local minimum point. Also, due to large difference in energy of localized states even at higher carrier densities, the increase of nearby possible hopping paths is insufficient to noticeably affect transfer rate. With increasing density of localized carriers, the number of empty localized states decreases. With the limited number of free states to move overall transfer rate falls rapidly. The simulations show that after the carrier density overcomes the density of localized states (10^{19} cm^{-3}), the exciton displacement drops to almost zero despite that the lifetime stays the same.

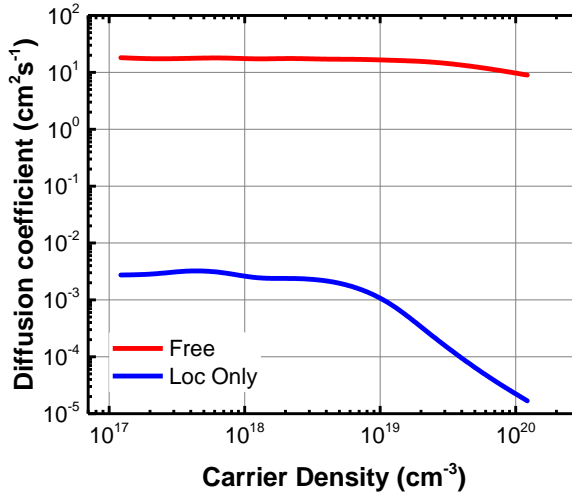


Fig. 5.2. Simulated diffusion coefficient dependence on photoexcited carrier density for free only (red line) and localized only (blue line) Carriers.

Fundamentally, we study the system of both localized and free carriers, so the diffusion coefficient is strongly affected by the ratio between the densities of both the particles. We can distinguish two essential parameters which have an impact on the carrier distribution: the dispersion parameter of potential fluctuations and the density of localized states.

Figure 5.3. represents the diffusion coefficient dependence on initial the carrier density at different parameters σ . Here, the density of localized states was set to 10^{19} cm^{-3} . The shape of the dependence remains similar for all σ , however, the higher perturbations in potential field decrease the ability of particle to move for a greater distance. In contrary, shallow localized states encourage the hopping process leading to the rise in the efficiency of transfer of localized excitons, but also increase the delocalization rate. The low excitation range shows a strong decrease of the diffusion coefficient with larger distortions of the potential field. That could be attributed to exponential drop-in hopping rate as the energy difference between states increases. At higher excitation intensities, the diffusion tends to return to classical “free carrier only” regime as the localized states acts more like traps rather than a transport route.

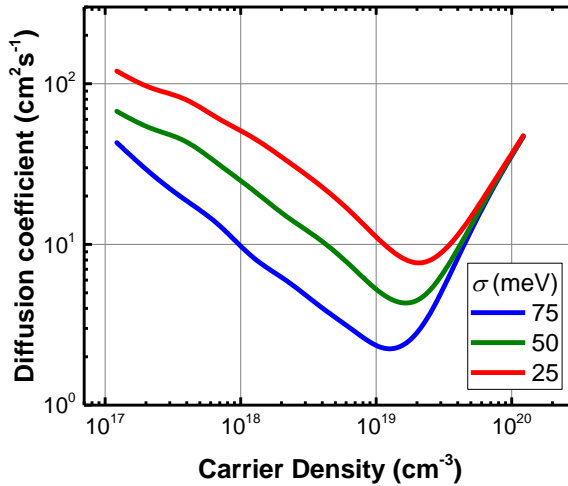


Fig. 5.3. Simulated diffusion coefficient dependence on photogenerated carrier density at different dispersion parameters (indicated).

While the energy distribution of localized states strongly influences the slope of the divergence of D parameter, it is also affected by a number of possible transition routes. For MQWs, there is a limited number of possible

neighboring localized states, reducing the efficiency of carrier transport even more due to a finite well width. Figure 5.4. shows the simulated dependence of diffusion coefficient on carrier density for samples with different MQW well widths. For better comparison, the photoexcited carrier density in all QWs was normalized to the sample volume and the generation rate was fixed at the same level for each individual simulation. The obtained data show a strong difference in diffusion in 2D-limited space (~ 1 nm), whereas the impact decreased with increasing well width 8 to 16 nm. The main factor of such diffusion behavior is the rise in the number of nearest localized states providing more freedom for both free and localized carriers to move.

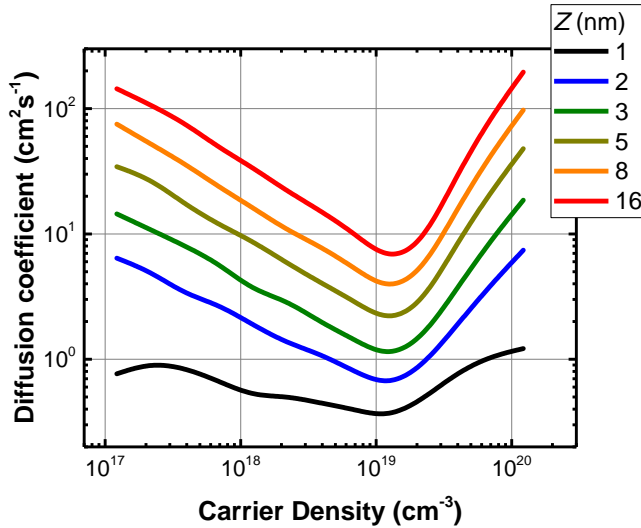


Fig. 5.4. Simulated dependence of diffusion coefficient on photogenerated carrier density at different MQW well widths.

As mentioned above, the density of localized states is another parameter important in these simulations. With a decrease in the density of localized states, the ratio between the densities of free and localized states changes drastically. However, before simulating the dependence of the diffusion coefficient on N_{loc} we need to include a limiting factor for free carrier lifetime. The nonradiative recombination rates are also affected by the density of localized states, thus, might potentially influence the results. The impact of bimolecular recombination on the diffusion coefficient dependence on carrier density is shown in Fig. 5.5. The band-to-band recombination is insignificant at low excitation. However, the rising of the density of free carriers results in a drastic rise of recombination rate leading to a substantial drop in both lifetime and diffusion.

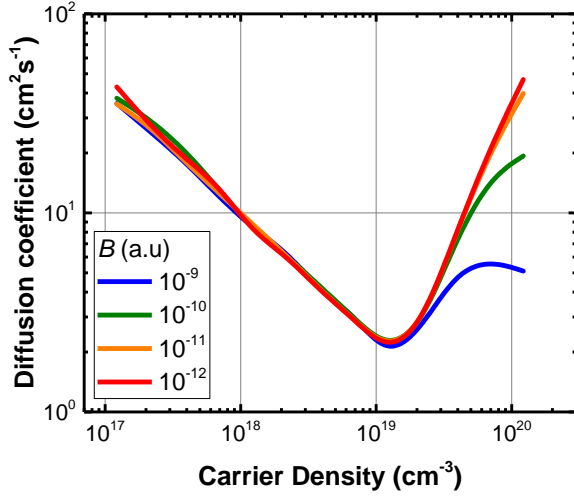


Fig. 5.5. Simulated dependence of diffusion coefficient on photogenerated carrier density at different values of bimolecular recombination coefficient.

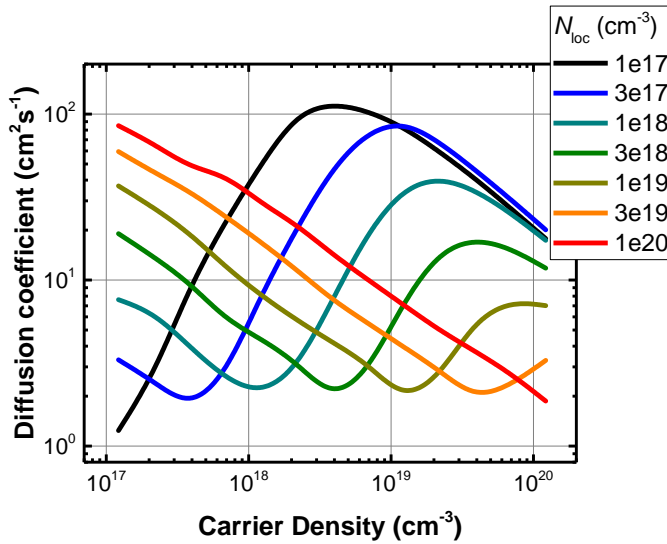


Fig. 5.6. Simulated dependence of diffusion coefficient on photogenerated carrier density at different densities of localized states.

In the next step, we simulate how N_{loc} affects D behavior. Figure 5.6. shows the dependence of the diffusion coefficient on the of density photoexcited carriers at different densities of localized states. The increase in the density of localized states steadily shifts the lines along X axis. The slope of decrease

and rise of diffusion coefficient remains the same. This is an indication that the shape of diffusivity is unaffected by hopping, as D value stays constant despite changes in the mean distance between the localized states. The minimal value of the diffusion coefficient corresponds to the largest ratio of $N_{\text{loc}}/N_{\text{free}}$. At such conditions, all localized states are almost completely occupied. In these conditions, the predominant part of carriers is localized and the diffusion is governed by the lifetime of localized carriers.

On the other hand, the radiative recombination from localized states affects the diffusion at all carrier densities (see Fig. 5.7.). The lower the lifetime of localized carriers, the smaller is the diffusion coefficient. Such behavior can be interpreted by several mechanisms. Firstly, due localization, the longer time does not mean particle could travel longer distance. Secondary, the longer lifetime means the localized states are filled more efficiently. As a result, the localization probability decreases, and this decrease leads to a larger number of free particles. Note, that we mainly focus on the diffusion behavior, thus we do not analyze, which type of recombination limits the exciton lifetime.

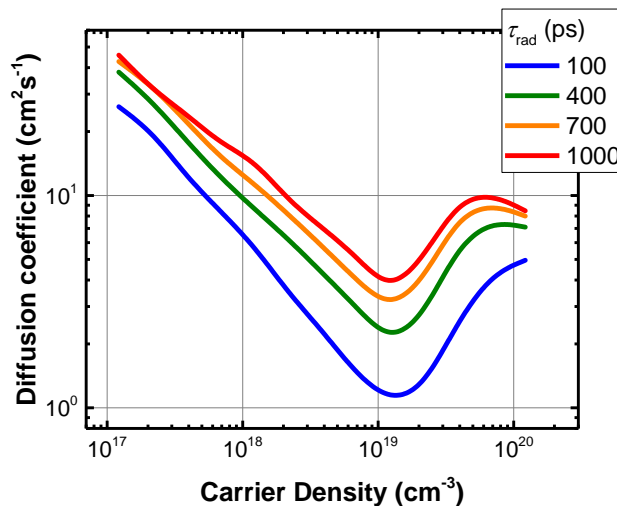


Fig. 5.7. Simulated dependence of diffusion coefficient on photogenerated carrier density at different radiative recombination lifetimes.

Finally, let us discuss the effects of non-radiative recombination for free carriers. Figure 5.8. represents the simulated diffusion coefficient as a function of photogenerated carrier density at different non-radiative recombination lifetimes. In the entire range studied, a higher rate of carrier

capture by NRC leads to a decrease in diffusivity. The influence of this process can be separated in two parts: before and after filling of localized states. At low excitation, the non-radiative recombination competes mainly with the carrier localization events, and the prevalence depends on the ratio between the densities of non-radiative recombination centers and localized states. Meanwhile at high carrier density, the diffusion coefficient is predominantly affected by the influence of free carriers due to their band-to-band recombination. The role of NRCs in the decrease of the diffusion coefficient is caused by reduction in free carrier lifetime, whereas the velocity remains unaffected.

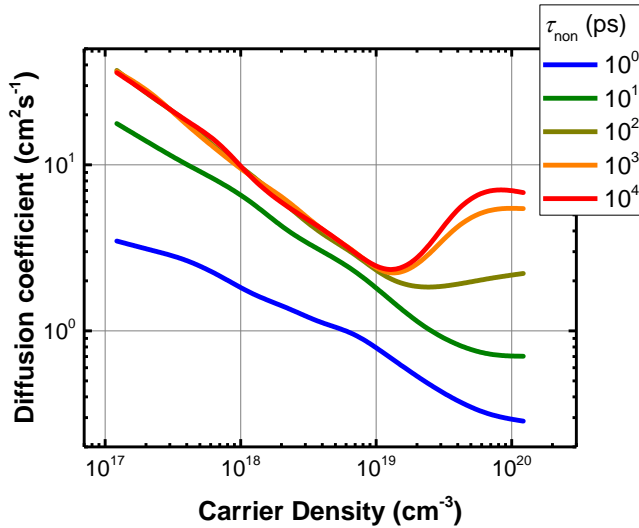


Fig. 5.8. Simulated dependence of diffusion coefficient on photogenerated carrier density at different non - radiative recombination lifetimes.

Summing up, the obtained results explain the measured decrease of diffusivity at low excitations followed by growth at elevated excitations. Due to a large velocity, free electrons and holes are spatially separated. As a result, their localization probability is limited and, consequently, they travel longer distances. The grow of the diffusivity at higher carrier densities is attributed to the overflow of localized states. This is in inconsistency with our early model. Previously, the high initial diffusion coefficient was interpreted to be a signature of efficient transport of localized holes. However, the simulated dependences presented in Fig. 5.2 show otherwise. It seems that the low diffusion coefficient D_0 used in calculations is actually the signature of strong localization. This interpretation also explains why the theoretical model is

better suitable for describing diffusion in c -plane sample where the localized states are already almost filled.

3.3.4. Fitting of the calculated dependences with those obtained experimentally

The simulation results were used to fit with the measured data. By applying such fitting in m -plane InGaN we have to take into account that light and heavy holes exist in this semiconductor. The energy of localized carriers is affected by their masses. Therefore, we can treat the material as consisting of two subsystems of localized states. Figure 5.9. shows the fit of simulated and experimental results. The carrier density dependences of the diffusion coefficient along a and c axes have been fitted separately.

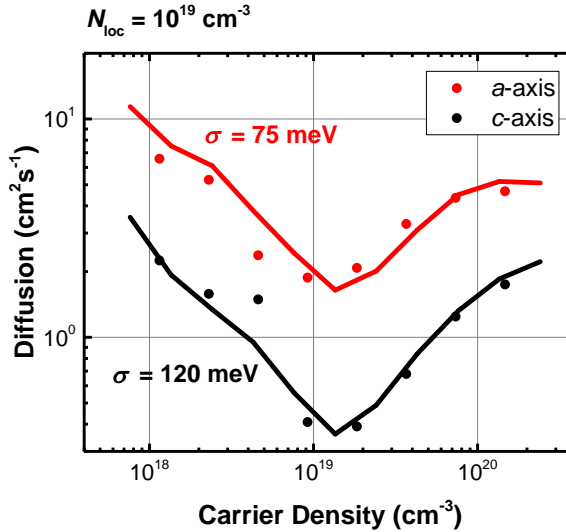


Fig. 5.9. Experimentally measured (points) and simulated (lines) diffusion coefficient of InGaN MQW as a function of carrier density along c and a axes.

The assumed value of the density of localized states $N_{loc} = 10^{19} \text{ cm}^{-3}$. The main difference between the dependences in the direction perpendicular and parallel to the crystallographic axis c was the different potential fluctuation parameter σ with values of 75 and 120 meV for $\parallel a$ and $\parallel c$, respectively. The radiative lifetime of localized carriers was set to be 200 ps, whereas the frequency of attempt (also used as localization/delocalization rate) ν_0 was equal to 10^{13} s^{-1} . The best fit value of non-radiative recombination lifetime at the density of

non – radiative recombination centers of 10^{16} cm^{-3} was found to be 40 ps along *c*-axis and 200 ps along *a*-axis. It is worth noting that the difference of lifetimes corresponds to the difference between hole masses Shockley-Read-Hall recombination rate depends on the capture of particles by NRCs, thus, heavy and light holes have different probabilities due to the differences in velocity and energy. Furthermore, due to difference in potential landscape fluctuation parameter the light holes have different localization/delocalization probabilities. The carrier interchange between first and second valence bands might be pointed out as another important effect [87]. If holes reallocate to another band, the carrier density in first band decreases faster than that in the second one. Finally, we simulate the holes propagating along different axes as separate systems, so, their contributions should be added.

For further examination, we exploited the advance of our model - the capability to follow the carrier dynamics, which is not revealed experimentally. We have already shown that the decrease in the diffusion coefficient is governed by the ratio of densities of free and localized carriers. Figure 5.10. displays how this ratio evolves in time. Red and blue lines represent the fraction of free and localized carriers in respect to the total number of generated particles. Two kinetics are selected for analyses. Figure 5.10 represents kinetics of free (red) at localized (blue) carrier densities at a) 10^{19} cm^{-3} and b) the point with lowest diffusivity under density of photogenerated carriers 10^{19} cm^{-3} . Figure 5.10 b) 10^{20} cm^{-3} . First one represents the point with lowest diffusivity, second the point with high diffusion coefficient, before the bimolecular recombination become predominant process.

At lower excitation, the carrier localization is instantaneous. The density of localized carriers is much higher than the density of free carriers. Consequently, the carrier diffusion is determined predominantly by the slower transport of localized carriers (excitons). Initially, the number of particles decreases linearly due to radiative recombination. At certain time after excitation, the density of free electrons and holes becomes too low for the localization to be important and has no significant influence on the overall carrier dynamics as the carrier density decreases approximately by three orders of magnitude. At higher excitation, all the localized states are filled, and the main part of carriers are free. Their density decreases rapidly due to non – radiative recombination compared to substantially slower decrease in the density of localized carriers. The value of the diffusion coefficient here is influenced by both processes, thermal movement of free carriers and hopping of excitons.

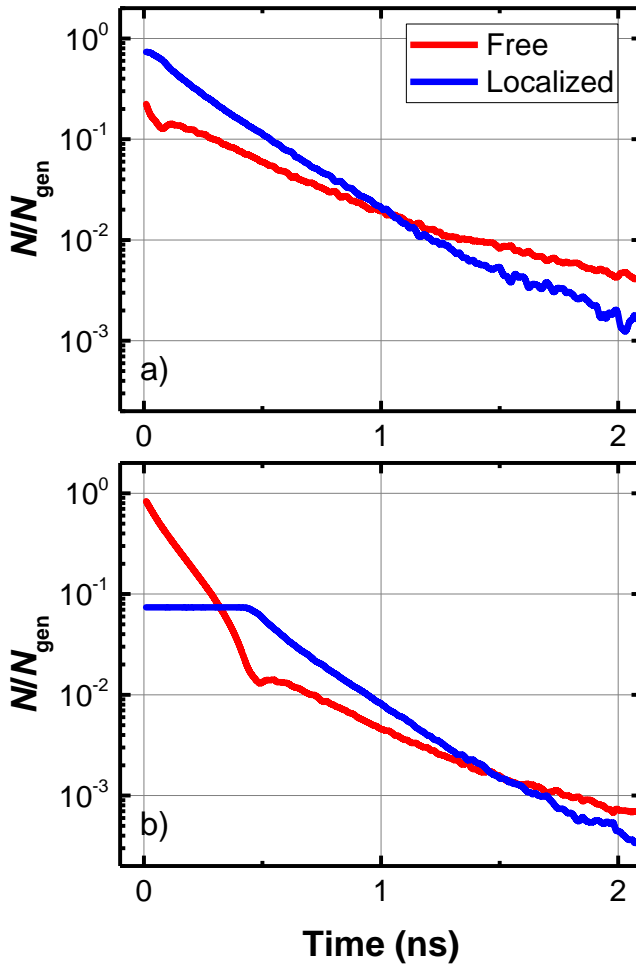


Fig. 5.10. Kinetics of free (red) and localized (blue) carrier densities at photoexcited carrier density of 10^{19} cm^{-3} (a) and 10^{20} cm^{-3} (b).

To get a better insight in the processes behind this kinetics, we studied the intensities of specific processes. Figure 5.11. represents the number of registered events for each separate recombination process. Radiative recombination from localized states (green line) is important at all excitations in the range studied. The event number increases linearly before reaching the limit corresponding to the situation when all localized states become filled. Bimolecular recombination (blue line) is negligible at low excitation as the localization process is actually instantaneous. This recombination mechanism becomes increasingly important at elevated excitation intensities but does not

become dominant even at the highest excitation intensities. Finally, the carrier density dependence of non-radiative recombination (red line) has three specific parts. The slow increase at the lowest carrier densities is dominated by “unlucky events” when generated particle is captured by NRC despite the large number of free localized states. The sharp increase represents the case when filling of deep localized states leads to the increase in the probability of thermal activation of localized carriers with lower activation energy. Note that each time the particle is delocalized provides another chance to be captured by nonradiative recombination centers. The slower increase at the highest excitation corresponds to the situation which occurs after all localized states are filled, whereas the carrier density is still too low for band-to-band recombination to become dominant. That means that the carrier lifetime is limited mainly by the linear radiative recombination at low and by the capture by NRC at high densities.

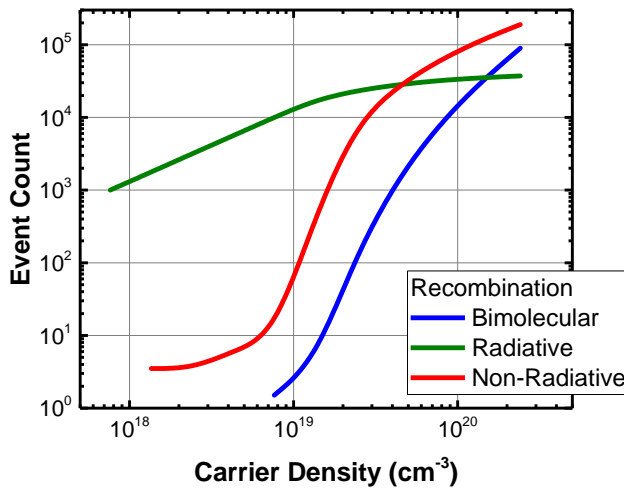


Fig. 5.11. Number of registered events for specific recombination process (indicated) as a function of photoexcited carrier density.

The simulated dependencies were calculated separately for a and c axis. To estimate the total carrier lifetime in the sample, two recombination channels working simultaneously have to be taken into account. The total lifetime is calculated as $1/\tau = 1/\tau_1 + 1/\tau_2$. Here, τ is total lifetime, and τ_1 , τ_2 are the lifetimes due to the two recombination processes discussed above. Figure 5.12. shows calculated carrier lifetime dependence on generated carrier density. The solid lines represent the lifetime for light (red) and heavy (black)

holes. The blue dashed line calculated under assumption that the impact of two particles is equal. We can expect to have the carrier lifetime around 800 ps at lowest excitation gradually decreasing with increasing carrier density to 150 ps. These values seem to fit nicely with experimentally obtained (points) at 90 and 360 $\mu\text{J}/\text{cm}^2$ with lifetime 500 and 220 ps respectively.

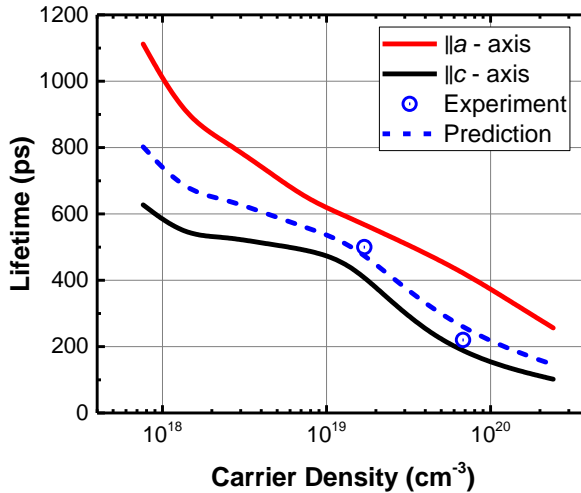


Fig. 5.12. Calculated (lines) and experimentally measured (points) carrier lifetime dependence on photoexcited carrier density for InGaN MQW.

Both diffusivity and lifetime dependences on photoexcited carrier density fits the experimental results with a good precision. This means that our model could be considered as a reliable tool for gaining new knowledge on the carrier behavior in ternary nitride compounds.

3.3.5. Conclusion

In InGaN quantum wells with strong potential fluctuations, both in polar and non-polar structures, the diffusion coefficient strongly depends on carrier density. This dependence cannot be explained in terms of valence band degeneracy alone. We demonstrate that carrier localization plays an important role in hole transport, even at very high carrier densities. The differences in the diffusion coefficient at different excitation densities can be attributed to a large difference in particle transport efficiency through free and localized states. In a system with strong localization, the diffusion of free carriers is by

several orders of magnitude more efficient than the diffusion localized excitons. The shape of the carrier density dependence of the diffusion coefficient at low densities is predominantly affected by the ratio between the densities of free and localized carriers. The dependence at elevated carrier densities is defined by the competition between localization and transfer. The lifetime of both free and localized carriers overall acts as the limiting factor for the diffusion coefficient. The simulation results are partially validated by a good fit between simulated and measured results.

CONCLUDING STATEMENTS

The developed kinetic Monte-Carlo model describes the dynamics in a system of nonequilibrium carriers containing both free and localized carriers and is capable to simulate the experimentally observed photoluminescence behavior in III-nitrides. Summing up the major results obtained in this study enables us to do the following key conclusions:

1. The dynamics of photoluminescence spectra depends on the ratio between the thermal energy and the energy dispersion parameter of localized states. Deeper localization energy leads to a higher luminescence efficiency and more pronounced *S* and *W* features in the temperature dependence of the PL band peak and band width, respectively.
2. At low densities of non-radiative recombination centers or localized states, the dominating process decreasing the PL intensity is the capture of free carriers by nonradiative recombination centers. This process is gradually enhanced with increasing temperature.
3. At high densities of both nonradiative recombination centers and localized states, the main channel for non-radiative recombination is tunneling of localized carriers to the nonradiative centers. In such cases the internal quantum efficiency can be low even at near zero temperatures.
4. The temperature dependences of photoluminescence intensity in AlGa_N rates can be properly described by the Arrhenius equation with two activation energies. The lower activation energy is smaller than the dispersion parameter of potential fluctuations and occurs due to the excitons hopping to non-radiative recombination centers. The higher activation energy occurs due to the capture of free carriers by non-radiative recombination centers.
5. Four typical areas with qualitatively different dependences of emission efficiency on the density of nonequilibrium carriers can be distinguished: the radiative recombination of localized carriers dominates in I and II areas, whereas the nonradiative recombination of free carriers is dominant in areas III and IV. The growing density

of localized and free carriers results in stronger delocalization and localization processes, which decrease the photoluminescence efficiency in area II and increase it in area IV.

6. The efficiency droop effect in AlGa_N can be attributed to a carrier-density-dependent transition of the system of nonequilibrium carriers from the state with majority of the carriers being localized and isolated from nonradiative recombination centers to the state with predominant part of the carriers being free and recombining as a result of capture by nonradiative recombination centers.
7. The changes in hopping rate does not affect the diffusion coefficient. The difference in diffusivity for free and localized carriers is so large that the diffusion coefficient depends exclusively on the ratio of the densities of free and localized carriers.
8. Increasing density of nonequilibrium carriers in InGa_N results initially to a decrease of the diffusion coefficient due to a rising probability of capturing electron-hole pairs to localized states and to a subsequent increase at elevated densities due to increasing fraction of free pairs. The minimal value of the diffusion coefficient corresponds to situation when all carriers are localized.
9. The anisotropy of the diffusion coefficient in non-polar InGa_N structures is determined by different localization energies for heavy and light holes.

LIST OF REFERENCES

- [1] S. Nakamura, M. Senoh, and T. Mukai, "P-gan/n-ingan/n-gan double-heterostructure blue-light-emitting diodes," *Japanese Journal of Applied Physics*, vol. 32, no. 1 A, 1993, doi: 10.1143/JJAP.32.L8.
- [2] K. Ahi, "Review of GaN-based devices for terahertz operation," *Optical Engineering*, vol. 56, no. 09, p. 1, 2017, doi: 10.1117/1.oe.56.9.090901.
- [3] M. Shahmohammadi *et al.*, "Enhancement of Auger recombination induced by carrier localization in InGaN/GaN quantum wells," *Physical Review B*, vol. 95, no. 12, pp. 1–10, 2017, doi: 10.1103/PhysRevB.95.125314.
- [4] J. Mickevičius, G. Tamulaitis, M. Shur, M. Shatalov, J. Yang, and R. Gaska, "Correlation between carrier localization and efficiency droop in AlGaIn epilayers," *Applied Physics Letters*, vol. 103, no. 1, 2013, doi: 10.1063/1.4813259.
- [5] E. Kuokstis, W. H. Sun, M. Shatalov, J. W. Yang, and M. A. Khan, "Role of alloy fluctuations in photoluminescence dynamics of AlGaIn epilayers," *Applied Physics Letters*, vol. 88, no. 26, pp. 1–4, 2006, doi: 10.1063/1.2218275.
- [6] N. I. Bochkareva, Y. T. Rebane, and Y. G. Shreter, "Efficiency droop and incomplete carrier localization in InGaIn/GaN quantum well light-emitting diodes," *Applied Physics Letters*, vol. 103, no. 19, 2013, doi: 10.1063/1.4828780.
- [7] K. Kazlauskas *et al.*, "Exciton hopping in In_xGa_{1-x}N multiple quantum wells," *Physical Review B - Condensed Matter and Materials Physics*, vol. 71, no. 8, 2005, doi: 10.1103/PhysRevB.71.085306.
- [8] S. Baranovskii, R. Eichmann, and P. Thomas, "Temperature-dependent exciton luminescence in quantum wells by computer simulation," *Physical Review B - Condensed Matter and Materials Physics*, vol. 58, no. 19, 1998, doi: 10.1103/PhysRevB.58.13081.
- [9] J. Piprek, "Efficiency droop in nitride-based light-emitting diodes," *physica status solidi (a)*, vol. 207, no. 10, pp. 2217–2225, Oct. 2010, doi: 10.1002/pssa.201026149.
- [10] M. Hugues, B. Damilano, J. Y. Duboz, and J. Massies, "Exciton dissociation and hole escape in the thermal photoluminescence quenching of (Ga,In)(N,As) quantum wells," *Physical Review B - Condensed Matter and Materials Physics*, vol. 75, no. 11, 2007, doi: 10.1103/PhysRevB.75.115337.

- [11] T. Hanada, "Basic Properties of ZnO, GaN, and Related Materials." pp. 1–19, 2009. doi: 10.1007/978-3-540-88847-5_1.
- [12] P. Waltereit *et al.*, "Nitride semiconductors free of electrostatic fields for efficient white light-emitting diodes," *Nature*, vol. 406, no. 6798, 2000, doi: 10.1038/35022529.
- [13] P. Waltereit *et al.*, "Nitride semiconductors free of electrostatic fields for White LEDs," *Letters to Nature*, vol. 406, 2000.
- [14] I. Vurgaftman, J. R. Meyer, and L. R. Ram-Mohan, "Band parameters for III-V compound semiconductors and their alloys," *Journal of Applied Physics*, vol. 89, no. 11 I, pp. 5815–5875, 2001, doi: 10.1063/1.1368156.
- [15] Y. P. Varshni, "Temperature dependence of the energy gap in semiconductors," *Physica*, vol. 34, no. 1, 1967, doi: 10.1016/0031-8914(67)90062-6.
- [16] K. Kazlauskas *et al.*, "Double-scaled potential profile in a group-III nitride alloy revealed by Monte Carlo simulation of exciton hopping," *Applied Physics Letters*, vol. 83, no. 18, pp. 3722–3724, Nov. 2003, doi: 10.1063/1.1625111.
- [17] P. G. Eliseev, P. Perlin, J. Lee, and M. Osinski, "'Blue' temperature-induced shift and band-tail emission in InGaN-based light sources," *Applied Physics Letters*, vol. 71, no. 5, pp. 569–571, 1997, doi: 10.1063/1.119797.
- [18] T. Ozaki, M. Funato, and Y. Kawakami, "Origin of temperature-induced luminescence peak shifts from semipolar $(11\bar{2})$ $\text{In}_x\text{Ga}_{1-x}\text{N}$ quantum wells," *Physical Review B*, vol. 96, no. 12, p. 125305, 2017, doi: 10.1103/physrevb.96.125305.
- [19] J. Mickevičius, G. Tamulaitis, M. Shur, M. Shatalov, J. Yang, and R. Gaska, "Internal quantum efficiency in AlGaN with strong carrier localization," *Applied Physics Letters*, vol. 101, no. 21, 2012, doi: 10.1063/1.4767657.
- [20] A. Bell *et al.*, "Exciton freeze-out and thermally activated relaxation at local potential fluctuations in thick Al_xGa_{1-x}N layers," *Journal of Applied Physics*, vol. 95, no. 9, pp. 4670–4674, 2004, doi: 10.1063/1.1689736.
- [21] K. Kazlauskas *et al.*, "Exciton hopping and nonradiative decay in AlGaN epilayers," *Applied Physics Letters*, vol. 87, no. 17, 2005, doi: 10.1063/1.2112169.
- [22] A. Kaneta, M. Funato, and Y. Kawakami, "Nanoscale recombination processes in InGaN/GaN quantum wells emitting violet, blue, and

- green spectra,” *Physical Review B - Condensed Matter and Materials Physics*, vol. 78, no. 12, 2008, doi: 10.1103/PhysRevB.78.125317.
- [23] Y. Lin *et al.*, “Interplay of point defects, extended defects, and carrier localization in the efficiency droop of InGaN quantum wells light-emitting diodes investigated using spatially resolved electroluminescence and photoluminescence,” *Journal of Applied Physics*, vol. 115, no. 2, 2014, doi: 10.1063/1.4861150.
- [24] J. Mickevičius, D. Dobrovolskas, J. Aleknavičius, T. Grinys, A. Kadys, and G. Tamulaitis, “Spatial redistribution of photoexcited carriers in InGaN/GaN structures emitting in a wide spectral range,” *Journal of Luminescence*, vol. 199, 2018, doi: 10.1016/j.jlumin.2018.03.078.
- [25] F. Hitzel, G. Klewer, S. Lahmann, U. Rossow, and A. Hangleiter, “Localized high-energy emissions from the vicinity of defects in high-efficiency Ga_xIn_{1-x}N GaN quantum wells,” *Physical Review B - Condensed Matter and Materials Physics*, vol. 72, no. 8, 2005, doi: 10.1103/PhysRevB.72.081309.
- [26] A. Pinos *et al.*, “Aging of AlGa_N quantum well light emitting diode studied by scanning near-field optical spectroscopy,” *Applied Physics Letters*, vol. 95, no. 18, pp. 16–19, 2009, doi: 10.1063/1.3262964.
- [27] A. Pinos, V. Liuolia, S. Marcinkevičius, J. Yang, R. Gaska, and M. S. Shur, “Localization potentials in AlGa_N epitaxial films studied by scanning near-field optical spectroscopy,” *Journal of Applied Physics*, vol. 109, no. 11, 2011, doi: 10.1063/1.3594239.
- [28] S. Marcinkevičius, R. Jain, M. Shatalov, J. Yang, M. Shur, and R. Gaska, “High spectral uniformity of AlGa_N with a high Al content evidenced by scanning near-field photoluminescence spectroscopy,” *Applied Physics Letters*, vol. 105, no. 24, 2014, doi: 10.1063/1.4904710.
- [29] J. Wang *et al.*, “An improved carrier rate model to evaluate internal quantum efficiency and analyze efficiency droop origin of InGa_N based light-emitting diodes,” *Journal of Applied Physics*, vol. 112, no. 2, 2012, doi: 10.1063/1.4736591.
- [30] Y. Iwata, R. G. Banal, S. Ichikawa, M. Funato, and Y. Kawakami, “Emission mechanisms in Al-rich AlGa_N/AlN quantum wells assessed by excitation power dependent photoluminescence spectroscopy,” *Journal of Applied Physics*, vol. 117, no. 7, 2015, doi: 10.1063/1.4908282.
- [31] W. Hahn *et al.*, “Evidence of nanoscale Anderson localization induced by intrinsic compositional disorder in InGa_N/Ga_N quantum wells by

- scanning tunneling luminescence spectroscopy,” *Physical Review B*, vol. 98, no. 4, pp. 2–6, 2018, doi: 10.1103/PhysRevB.98.045305.
- [32] R. A. Oliver *et al.*, “Microstructural origins of localization in InGaN quantum wells,” *Journal of Physics D: Applied Physics*, vol. 43, no. 35, 2010, doi: 10.1088/0022-3727/43/35/354003.
- [33] S. Chichibu, T. Azuhata, T. Sota, and S. Nakamura, “Spontaneous emission of localized excitons in InGaN single and multiquantum well structures,” *Applied Physics Letters*, vol. 69, no. 27, 1996, doi: 10.1063/1.116981.
- [34] M. Shatalov *et al.*, “Efficiency of light emission in high aluminum content AlGaN quantum wells,” *Journal of Applied Physics*, vol. 105, no. 7, 2009, doi: 10.1063/1.3103321.
- [35] J. Mickevičius *et al.*, “Stimulated emission due to localized and delocalized carriers in Al_{0.35}Ga_{0.65}N/Al_{0.49}Ga_{0.51}N quantum wells,” *Applied Physics Letters*, vol. 101, no. 4, 2012, doi: 10.1063/1.4738791.
- [36] E. Francesco Pecora *et al.*, “Sub-250 nm room-temperature optical gain from AlGaN/AlN multiple quantum wells with strong band-structure potential fluctuations,” *Applied Physics Letters*, vol. 100, no. 6, 2012, doi: 10.1063/1.3681944.
- [37] J. Mickevičius *et al.*, “Influence of carrier localization on high-carrier-density effects in AlGaN quantum wells,” *Optics Express*, vol. 22, no. S2, p. A491, 2014, doi: 10.1364/OE.22.00A491.
- [38] F. Nippert *et al.*, “Auger recombination in AlGaN quantum wells for UV light-emitting diodes,” *Applied Physics Letters*, vol. 113, no. 7, 2018, doi: 10.1063/1.5044383.
- [39] M. A. Hopkins, D. W. E. Allsopp, M. J. Kappers, R. A. Oliver, and C. J. Humphreys, “The ABC model of recombination reinterpreted: Impact on understanding carrier transport and efficiency droop in InGaN/GaN light emitting diodes,” *Journal of Applied Physics*, vol. 122, no. 23, 2017, doi: 10.1063/1.4986434.
- [40] K. A. Bulashevich and S. Y. Karpov, “Is Auger recombination responsible for the efficiency rollover in III-nitride light-emitting diodes?,” *Physica Status Solidi (C) Current Topics in Solid State Physics*, vol. 5, no. 6, pp. 2066–2069, 2008, doi: 10.1002/pssc.200778414.
- [41] J. Hader, J. v. Moloney, S. W. Koch, L. Fan, and M. Fallahit, “Carrier recombination in semiconductor lasers: Beyond the ABC,” *2006 International Conference on Numerical Simulation of Semiconductor*

- Optoelectronic Devices, NUSOD '06*, no. February 2006, pp. 39–40, 2006, doi: 10.1109/NUSOD.2006.306730.
- [42] M. Filoche, M. Piccardo, Y. R. Wu, C. K. Li, C. Weisbuch, and S. Mayboroda, “Localization landscape theory of disorder in semiconductors. I. Theory and modeling,” *Physical Review B*, vol. 95, no. 14, pp. 1–18, 2017, doi: 10.1103/PhysRevB.95.144204.
- [43] M. Piccardo *et al.*, “Localization landscape theory of disorder in semiconductors. II. Urbach tails of disordered quantum well layers,” *Physical Review B*, vol. 95, no. 14, pp. 1–12, 2017, doi: 10.1103/PhysRevB.95.144205.
- [44] F. Nippert *et al.*, “Determination of recombination coefficients in InGaN quantum-well light-emitting diodes by small-signal time-resolved photoluminescence,” *Japanese Journal of Applied Physics*, vol. 55, no. 5, pp. 1–6, 2016, doi: 10.7567/JJAP.55.05FJ01.
- [45] C. R. Haughn *et al.*, “Highly radiative nature of ultra-thin c-plane Al-rich AlGaIn/AlN quantum wells for deep ultraviolet emitters,” *Applied Physics Letters*, vol. 114, no. 10, pp. 2–7, 2019, doi: 10.1063/1.5087543.
- [46] T. Langer *et al.*, “Room temperature excitonic recombination in GaInN/GaN quantum wells,” *Applied Physics Letters*, vol. 103, no. 20, 2013, doi: 10.1063/1.4830366.
- [47] K. Jandieri *et al.*, “Nonexponential photoluminescence transients in a Ga(NAsP) lattice matched to a (001) silicon substrate,” *Physical Review B - Condensed Matter and Materials Physics*, vol. 87, no. 3, 2013, doi: 10.1103/PhysRevB.87.035303.
- [48] J. Mickevičius *et al.*, “Efficiency droop and carrier transport in AlGaIn epilayers and heterostructures,” *Physica Status Solidi (B) Basic Research*, vol. 252, no. 5, pp. 961–964, 2015, doi: 10.1002/pssb.201451542.
- [49] A. Yasan, R. McClintock, K. Mayes, D. H. Kim, P. Kung, and M. Razeghi, “Photoluminescence study of AlGaIn-based 280 nm ultraviolet light-emitting diodes,” *Applied Physics Letters*, vol. 83, no. 20, 2003, doi: 10.1063/1.1626808.
- [50] D. Bimberg and J. Mycielski, “Recombination-induced heating of free carriers in a semiconductor,” *Physical Review B*, vol. 31, no. 8, pp. 5490–5493, 1985, doi: 10.1103/PhysRevB.31.5490.
- [51] Y. Yang, P. Ma, X. Wei, D. Yan, Y. Wang, and Y. Zeng, “Design strategies for enhancing carrier localization in InGaIn-based light-emitting diodes,” *Journal of Luminescence*, vol. 155, 2014, doi: 10.1016/j.jlum.2014.05.002.

- [52] H. D. Sun, S. Calvez, M. D. Dawson, J. A. Gupta, G. C. Aers, and G. I. Sproule, "Thermal quenching mechanism of photoluminescence in 1.55 μm GaInNAsSb/Ga(N)As quantum-well structures," *Applied Physics Letters*, vol. 89, no. 10, 2006, doi: 10.1063/1.2345240.
- [53] K. L. Teo *et al.*, "An analysis of temperature dependent photoluminescence line shapes in InGaN," *Applied Physics Letters*, vol. 73, no. 12, 1998, doi: 10.1063/1.122249.
- [54] X. H. Zheng *et al.*, "Influence of the deposition time of barrier layers on optical and structural properties of high-efficiency green-light-emitting InGaN/GaN multiple quantum wells," *Journal of Applied Physics*, vol. 96, no. 4, 2004, doi: 10.1063/1.1769099.
- [55] M. A. Sousa *et al.*, "Luminescence studies on green emitting InGaN/GaN MQWs implanted with nitrogen," *Scientific Reports*, vol. 5, pp. 6–11, 2015, doi: 10.1038/srep09703.
- [56] O. Rubel *et al.*, "Model of temperature quenching of photoluminescence in disordered semiconductors and comparison to experiment," *Physical Review B - Condensed Matter and Materials Physics*, vol. 73, no. 23, 2006, doi: 10.1103/PhysRevB.73.233201.
- [57] M. Baranowski, M. Latkowska, R. Kudrawiec, and J. Misiewicz, "Model of hopping excitons in GaInNAs: Simulations of sharp lines in micro-photoluminescence spectra and their dependence on the excitation power and temperature," *Journal of Physics Condensed Matter*, vol. 23, no. 20, 2011, doi: 10.1088/0953-8984/23/20/205804.
- [58] T. Jansen, "Kinetic Monte Carlo," in *Computational Methods in Catalysis and Materials Science: An Introduction for Scientists and Engineers*, vol. 95, no. 1991, 2009, pp. 183–197. doi: 10.1002/9783527625482.ch10.
- [59] J. Stephan, S. Schrader, and L. Brehmer, "Monte Carlo simulations of charge transport in molecular solids: a modified Miller Abrahams type jump rate approach," *Synthetic Metals*, vol. 111, pp. 353–357, 2000, doi: 10.1016/S0379-6779(99)00323-9.
- [60] T. Saxena *et al.*, "Spectral dependence of carrier lifetime in high aluminum content AlGaN epitaxial layers," *Journal of Applied Physics*, vol. 118, no. 8, pp. 19646–19655, 2015, doi: 10.1063/1.4929499.
- [61] M. A. Reshchikov and H. Morkoç, "Luminescence properties of defects in GaN," *Journal of Applied Physics*, vol. 97, no. 6, 2005, doi: 10.1063/1.1868059.
- [62] A. David, N. G. Young, C. Lund, and M. D. Craven, "Review—The Physics of Recombinations in III-Nitride Emitters," *ECS Journal of*

- Solid State Science and Technology*, vol. 9, no. 1, p. 016021, 2020, doi: 10.1149/2.0372001jss.
- [63] C. E. Dreyer, A. Alkauskas, J. L. Lyons, J. S. Speck, and C. G. van de Walle, "Gallium vacancy complexes as a cause of Shockley-Read-Hall recombination in III-nitride light emitters," *Applied Physics Letters*, vol. 108, no. 14, 2016, doi: 10.1063/1.4942674.
- [64] A. Hangleiter *et al.*, "Radiative recombination in polar, non-polar, and semi-polar III-nitride quantum wells," *Gallium Nitride Materials and Devices XII*, vol. 10104, no. February 2017, p. 101040Q, 2017, doi: 10.1117/12.2252036.
- [65] A. David, N. G. Young, C. Lund, and Craven Michael D., "The physics of recombinations in III-nitride emitters," *This Issue*, 2020, doi: 10.1149/2.0372001JSS.
- [66] S. Rudin, "Temperature-dependent exciton linewidths in semiconductors," *Physical Review B*, vol. 42, no. 17, pp. 218–231, 1990.
- [67] K. B. Nam, J. Li, J. Y. Lin, and H. X. Jiang, "Optical properties of AlN and GaN in elevated temperatures," *Applied Physics Letters*, vol. 85, no. 16, pp. 3489–3491, Oct. 2004, doi: 10.1063/1.1806545.
- [68] R. Kim, X. Wang, and M. Lundstrom, "Notes on Fermi-Dirac Integrals 4th Edition," *arXiv*, no. 1, pp. 1–15, 2019.
- [69] P. Ščajev *et al.*, "Diffusion Enhancement in Highly Excited MAPbI₃ Perovskite Layers with Additives," *Journal of Physical Chemistry Letters*, vol. 9, no. 12, pp. 3167–3172, 2018, doi: 10.1021/acs.jpcclett.8b01155.
- [70] M. Ansari-Rad, J. A. Anta, and J. Bisquert, "Interpretation of diffusion and recombination in nanostructured and energy-disordered materials by stochastic quasiequilibrium simulation," *Journal of Physical Chemistry C*, vol. 117, no. 32, pp. 16275–16289, 2013, doi: 10.1021/jp403232b.
- [71] A. H. Hill, K. E. Smyser, C. L. Kennedy, E. S. Massaro, and E. M. Grumstrup, "Screened Charge Carrier Transport in Methylammonium Lead Iodide Perovskite Thin Films," *Journal of Physical Chemistry Letters*, vol. 8, no. 5, pp. 948–953, 2017, doi: 10.1021/acs.jpcclett.7b00046.
- [72] S. Chichibu, T. Azuhata, T. Sota, and S. Nakamura, "Spontaneous emission of localized excitons in InGaN single and multiquantum well structures," *Applied Physics Letters*, vol. 69, no. 27, pp. 4188–4190, 1996, doi: 10.1063/1.116981.

- [73] M. Baranowski, R. Kudrawiec, J. Misiewicz, H. Turski, and C. Skierbiszewski, "Photoluminescence characterization of InGaN/InGa_N quantum wells grown by plasma-assisted molecular beam epitaxy: Impact of nitrogen and gallium fluxes," *Physica Status Solidi (B) Basic Research*, vol. 252, no. 5, 2015, doi: 10.1002/pssb.201451588.
- [74] J. Wang, L. Wang, W. Zhao, Z. Hao, and Y. Luo, "Understanding efficiency droop effect in InGaN/GaN multiple-quantum-well blue light-emitting diodes with different degree of carrier localization," *Applied Physics Letters*, vol. 97, no. 20, 2010, doi: 10.1063/1.3520139.
- [75] O. Kravcov, J. Mickevičius, and G. Tamulaitis, "Origin of thermal quenching of exciton photoluminescence in algan epilayers," *Lithuanian Journal of Physics*, vol. 61, no. 2, pp. 84–90, 2021, doi: 10.3952/physics.v61i2.4437.
- [76] E. Kuokstis, J. W. Yang, G. Simin, M. A. Khan, R. Gaska, and M. S. Shur, "Two mechanisms of blueshift of edge emission in InGaN-based epilayers and multiple quantum wells," *Applied Physics Letters*, vol. 80, no. 6, pp. 977–979, 2002, doi: 10.1063/1.1433164.
- [77] J. Mickevičius *et al.*, "Stimulated emission in AlGa_N/AlGa_N quantum wells with different Al content," *Applied Physics Letters*, vol. 100, no. 8, 2012, doi: 10.1063/1.3688051.
- [78] N. Nepal, J. Li, M. L. Nakarmi, J. Y. Lin, and H. X. Jiang, "Temperature and compositional dependence of the energy band gap of AlGa_N alloys," *Applied Physics Letters*, vol. 87, no. 24, pp. 1–3, 2005, doi: 10.1063/1.2142333.
- [79] G. Tamulaitis *et al.*, "Study of exciton hopping in AlGa_N epilayers by photoluminescence spectroscopy and Monte Carlo simulation," *Physica Status Solidi (C) Current Topics in Solid State Physics*, vol. 3, no. June, pp. 2099–2102, 2006, doi: 10.1002/pssc.200565334.
- [80] T. H. Gfroerer, R. Chen, G. Watt, Z. Liu, and Y. Zhang, "Impact of superlinear defect-related recombination on LED performance at low injection," *Journal of Applied Physics*, vol. 125, no. 20, 2019, doi: 10.1063/1.5089125.
- [81] J. Mickevičius *et al.*, "Temperature-dependent efficiency droop in AlGa_N epitaxial layers and quantum wells," *AIP Advances*, vol. 6, no. 4, 2016, doi: 10.1063/1.4947574.
- [82] H. J. Eichler, "Laser-Induced Dynamic Gratings and Four Wave Mixing-Material Investigations and Coherent Light Amplification," in *Spectroscopy of Solid-State Laser-Type Materials*, 1987. doi: 10.1007/978-1-4613-0899-7_14.

- [83] R. Aleksiejūnas *et al.*, “Impact of Alloy-Disorder-Induced Localization on Hole Diffusion in Highly Excited c -Plane and m -Plane (In, Ga) N Quantum Wells,” *Physical Review Applied*, vol. 14, no. 5, 2020, doi: 10.1103/PhysRevApplied.14.054043.
- [84] T. Malinauskas, K. Jarasiunas, M. Heuken, F. Scholz, and P. Brückner, “Diffusion and recombination of degenerate carrier plasma in GaN,” *Physica Status Solidi (C) Current Topics in Solid State Physics*, vol. 6, no. SUPPL. 2, 2009, doi: 10.1002/pssc.200880856.
- [85] P. Ščajev, K. Jarašinas, Ü. Özgür, H. Morkoç, J. Leach, and T. Paskova, “Anisotropy of free-carrier absorption and diffusivity in m-plane GaN,” *Applied Physics Letters*, vol. 100, no. 2, 2012, doi: 10.1063/1.3674306.
- [86] R. Aleksiejunas, P. Scajev, S. Nargelas, T. Malinauskas, A. Kadys, and K. Jarasiunas, “Impact of diffusivity to carrier recombination rate in nitride semiconductors: From bulk GaN to (In,Ga)N quantum wells,” *Japanese Journal of Applied Physics*, vol. 52, no. 8 PART 2, 2013, doi: 10.7567/JJAP.52.08JK01.
- [87] V. Liuolia, S. Marcinkevičius, Y. da Lin, H. Ohta, S. P. Denbaars, and S. Nakamura, “Dynamics of polarized photoluminescence in m-plane InGaN/GaN quantum wells,” *Journal of Applied Physics*, vol. 108, no. 2, 2010, doi: 10.1063/1.3460278.

SANTRAUKA

Šviestukai (angl. *Ligt Emitting Diodes, LEDs*) tampa svarbiu šviesos šaltiniu daugelyje plačiai vartojamų prietaisų: videoekranuose, eismo šviesose, šiltnamių apšvietime ir kitose srityse, bet, svarbiausia, bendrajame apšvietime, kur diegiant šviestukinius baltos šviesos šaltinius tikimasi sutaupyti iki 10 procentų šiuo metu pasaulyje suvartojamos elektros energijos. Nors pirmieji šviestukai (šviesos diodai) buvo atrasti prieš daugiau nei pusę amžiaus, svarbiu šviesos šaltiniu jie tapo tik 1993 m. sukūrus didelio ryškio mėlynos spalvos šviestuką, pagamintą galio nitrido pagrindu [1]. Nuo tada prasidėjo itin plataus masto III grupės nitridų tyrimai ir aktyvus jų technologijų tobulinimas.

Nitridinės technologijos turi ir daug privalumų. Šie junginiai yra atsparūs jonizuojančiai spinduliuotei, o jų pagrindu sukurti puslaidininkiniai prietaisai gali veikti ne tik regimojoje spektro dalyje, bet ir terahercinių dažnių ruože [2]. Keičiant trinarių nitridinių junginių, tokių kaip AlGaN ar InGaN, sudėtį galima derinti draustinio tarpo energiją plačiame energijų ruože kas leidžia apimti visą regimosios šviesos spektrą bei ultravioletinės ir infra-raudonosios šviesos ruožus. Šiose medžiagose pasireiškia nepusiausvirųjų krūvininkų lokalizacija. Tai galima charakterizuoti matuojant ir aprašant liuminescencijos priklausomybes nuo temperatūros. Yra žinoma, kad liuminescencijos juostos smailės padėtis ir tos juostos plotis turi specifines „S“ ir „W“ formas [3][4]. Šios savybės lemtos lokalizuotų būsenų, kurios atsiranda dėl potencialo fluktuacijų medžiagoje, susijusių su daugiakomponentės medžiagos nehomogeniška sudėtimi [5]. Didelė problema yra tai, kad didėjant žadinimui šių darinių vidinis kvantinis našumas ženkliai krenta dėl taip vadinamo našumo nuokryčio efekto [6].

Geresnis šių procesų ir mechanizmų supratimas gali padėti pagerinti bei patobulinti nitridinių medžiagų pagrindu sukurtus optoelektroninius prietaisus. Šio disertacinio darbo tikslu buvo suprasti, kaip laisvi ir lokalizuoti krūvininkai įtakoja fotoliuminescencines savybes trinariuose nitridų dariniuose ir išskirti mechanizmus, lemiančius specifines krūvininkų dinamikos savybes. Tuo tikslu buvo sukurtas modelis, pritaikantis kinetinio Monte – Karlo algoritmą modeliuoti sistemą su laisvais ir lokalizuotais krūvininkais. Iki šiol publikuotuose darbuose lokalizuoti ir laisvieji krūvininkai buvo aprašomi kaip atskiros krūvininkų sistemos. Modelis buvo optimizuojamas lyginant gautus duomenis su išmatuotais rezultatais.

Darbo tikslai

Pagrindinis šio darbo tikslas yra ištirti laisvų ir lokalizuotų krūvininkų dinamiką III grupės nitridiniuose dariniuose taikant kinetinio Monte-Karlo algoritmą. Tuo pačiu metu modeliuojant laisvų ir lokalizuotų nepusiausvirųjų krūvininkų evoliuciją laike siekiama atskleisti sąveiką tarp skirtingų rekombinacijos procesų ir fotoluminescencijos parametrų bei efektyvumo epitaksiniuose sluoksniuose ir kvantiniuose lakštuose su skirtingomis krūvininkų lokalizacijos sąlygomis. Tapatinant sumodeliuotas priklausomybes su kitų autorių išmatuotais rezultatais panaudojamos verifikuoti modelį ir išgauti skaičiavimams reikalingus parametrus. Ypatingas dėmesys skiriamas unikalioms trinarių nitridų fotoluminescencijos parametrų priklausomybėms nuo temperatūros ir priežastims, lemiančioms efektyvumo nuokrytį didėjant nepusiausvirųjų krūvininkų tankiui.

Darbo užduotys

- I. Sukurti teorinį modelį, leidžiantį aprašyti sistemą, vienu metu sudarytą iš laisvų ir lokalizuotų krūvininkų III grupės nitridų epitaksiniuose sluoksniuose ir kvantiniuose lakštuose.
- II. Pritaikyti kinetinio Monte-Karlo algoritmą siekiant aprašyti fotoluminescencijos dinamiką III grupės nitridų dariniuose su skirtingu lokalizacijos stiprumu plačiame nepusiausvirųjų krūvininkų tankio ruože.
- III. Sutapatinti modeliavimo metu gautus rezultatus su išmatuotomis fotoluminescencijos parametrų priklausomybėmis nuo temperatūros ir krūvininkų tankio AlGaIn epitaksiniame sluoksnyje.
- IV. Ištirti lokalizacijos sąlygų ir rekombinacijos mechanizmų įtaką fotoluminescencijos efektyvumui ir spektro formai esant žemo žadinimo sąlygoms.
- V. Ištirti sistemą, sudarytą iš laisvų ir lokalizuotų krūvininkų ir nustatyti procesų joje įtaką fotoluminescencijos spektrui bei efektyvumui.
- VI. Atskleisti efektyvumo nuokryčio priežastis.
- VII. Įvertinti lokalizacijos poveikį krūvininkų difuzijai.

Mokslinis naujumas ir svarba

Monte-Karlo algoritmas yra dažnai taikomas siekiant nustatyti fotoluminescencijos savybes III grupės nitriduose [7][8]. Deja, literatūroje randami rezultatai apsiriboja viendalelinio modelio variantais, todėl lieka neįvertinta laisvųjų krūvininkų įtaka. Toks metodas gerai tinka prie žemų žadinių, tačiau nėra tinkamas siekiant nustatyti lokalizacijos įtaką efektyvumo nuokryčiui, kuris yra svarbi savybė daugelyje šių medžiagų pritaikymo sričių. Monte-Karlo tipo algoritmai, aprašantys sudėtingas sistemas, stipriai priklauso nuo sistemoje vykstančių procesų spartų, kurias gana sudėtinga tinkamai nustatyti ar įvertinti. Tokiais atvejais vidinis kvantinis našumas aprašomas empirinėmis ABC [9] arba Arenijaus [10] formulėmis. Nepaisant gero šių modelių sutapimo prie aukštesnių žadinimo tankių, jie neaprašo nepusiausvirųjų krūvininkų dinamikos plačiame krūvininkų tankio diapazone. Pagrindiniai trūkumai, ribojantis ABC modelio produktyvumą, yra tai, kad jis aprašo tik laisvuosius krūvininkus ir neatsižvelgia į rekombinacijos koeficientų galimą priklausomybę nuo žadinimo sąlygų. Kita vertus, Arenijaus formulė aprašo sistemą su skirtingais rekombinacijos kanalais, tačiau gaunami tapatinimo parametrai nėra tiesiogiai susieti su atskirais rekombinacijos mechanizmais, o daugiau atspindi bendrą visų procesų įtaką.

Šiame darbe pritaikytas kinetinio Monte-Karlo modelis suteikia unikalią galimybę stebėti atskyrų pernašos ir rekombinacijos procesų įtaką realių laiku, įskaitant nepusiausvirųjų krūvininkų pasiskirstymus pagal energiją ir erdvėje. Gauti modeliavimo rezultatai, vienu metu aprašantys keturias išmatuotas fotoluminescencijos parametrų priklausomybes, leido įvertinti III grupės nitriduose vykstančių procesų parametrus ir tų procesų svarbą šių medžiagų liuminescencijos savybėms, ko nebuvo įmanoma padaryti vien iš eksperimento rezultatų.

Ginamieji teiginiai

- I. Sistemoje su stipria lokalizacija ir dideliu nespindulinės rekombinacijos centrų tankiu fotoluminescencijos efektyvumo kritimą lemia lokalizuotų eksitonų tuneliavimas į nespindulinės rekombinacijos centrus. Dėl šios priežasties vidinis kvantinis našumas yra žemesnis nei 100% netgi prie žemų temperatūrų ar esant mažam nepusiausvirųjų krūvininkų tankiui.
- II. Efektyvumo nuokrytis didėjant nepusiausvirųjų krūvininkų tankiui III grupės nitriduose su stipria krūvininkų lokalizacija vyksta dėl stiprėjančios krūvininkų delokalizacijos ir delokalizuoatų krūvininkų nespindulinės rekombinacijos. Tai pasireiškia prie mažesnių nepusiausvirųjų krūvininkų tankių nei reikalingas ženkliai pasireikšti nespindulinei Ožė rekombinacijai.
- III. Augantis nepusiausvirųjų krūvininkų tankis InGaN iš pradžių mažina difuzijos koeficiento vertę dėl stiprėjančios lokalizacijos, bet po to lemia jos augimą dėl didėjančios laisvųjų krūvininkų dalies. Difuzijos koeficiento anizotropija nepoliniuose InGaN dariniuose atsiranda dėl lokalizacijos energijos lengvosioms ir sunkiosioms skylėms skirtumo.

Autoriaus indėlis

Autorius sukūrė modelį ir atliko visus darbe pateiktus teorinius skaičiavimus. Programa, skirta atlikti kMC modeliavimus, buvo parašyta nuo nulio naudojant C++ ir tobulinama per visą doktorantūros laikotarpį.

Darbe panaudoti eksperimentiniai rezultatai, gauti kolegų iš Vilniaus universiteto Fizikos fakulteto Fotonikos ir nanotechnologijų instituto.

1. TEORINIS MODELIS

Sukurtas teorinis modelis, skirtas aprašyti nepusiausvirųjų krūvininkų sistemai su laisvais elektronais ir skylėm bei lokalizuotomis elektrono-skylės poromis. Laisvieji krūvininkai juda nepriklausomai vienas nuo kito erdvėje, o jų energija aprašoma pagal Fermi – Dirako statistiką. Tuo tarpu lokalizuota elektrono – skylės pora yra aprašoma kaip viena dalelė, eksitonas, kurio energija yra fiksuota ir ligi lokalizuotos būsenos energijai. Eksitonas gali judėti erdvėje šokuodamas per lokalizuotas būsenas. Kiekvienai dalelei priskiriama grupė rekombinacijos procesų, kurie gali įvykti su atitinkama sparta priklausomai nuo esamos sistemos būsenos. Pritaikydami Monte – Karlo algoritmo metodus modeliavome krūvininkų dinamiką ir tokios sistemos evoliuciją laike.

1.1. Monte-Karlo algoritmas

Kinetinis Monte-Karlo algoritmas dažnai taikomas norint aprašyti sudėtingų sistemų evoliuciją. Naudojant atsitiktinių skaičių generatorių sistemos būseną yra atnaujinama priklausomai nuo galimų įvykių spartos. Fotoluminescencijos dinamiką aprašantys modeliai iki šiol buvo paremti viendaleliais Monte-Karlo algoritmais [8][56][57]. Priklausomai nuo paskirties, algoritmai skirtingi, bet yra iš esmės nulemti dviejų problemų: pasirinkti įvykį, kuris pagal savo tikimybę nutiks, ir nustatyti laiką kuriuo metu tai įvyks [58]. Galutinis rezultatas gaunamas iš duomenų kartojant skaičiavimus daugybę kartų (10^5 ir daugiau). Supaprastina algoritmo procedūrą, naudotą skaičiavimuose, galima aprašyti taip:

1. *Inicializuoti pradines reikšmes.*
2. *Sugeneruoti būsenas.*
3. *Nustatyti pradinę laiko atskaitą $t = 0$.*
4. *Atnaujinti modeliavime dalyvaujančias daleles:*
 - a) *generuoti naujas daleles;*
 - b) *atnaujinti esamų dalelių būsenas;*
 - c) *užtikrinti, kad nėra konfliktų tarp procesų;*
 - d) *atsižvelgti į šiluminius procesus.*
5. *Išsaugoti duomenis ir padidinti laiką pasirinktu žingsniu: $t = t + dt$.*
6. *Pakartoti skaičiavimus nuo ketvirtojo žingsnio, kol nesibaigia nustatytas skaičiavimo laikas: $t < t_{max}$*

7. Kartoti skaičiavimus nuo antrojo žingsnio N kartų, kol bus surinkta pakankamai duomenų.

Šis algoritmas tinka modeliuoti kiek viendalelius, tiek daugiadalelius procesus. Siekiant paspartinti skaičiavimus sukurtas algoritmas praleisti kai kuriuos žingsnius, kurie neturi įtakos skaičiavimo rezultatui.

1.2. Būsenų generavimas

Skaičiavimo metu naudojamas keturdimensinis tinklelis, aprašantis modeliuojamų dalelių pasiskirstymą erdvėje ir pagal energijas. Kiekvienas šio tinklelio narvelis yra parenkamas taip, kad jame tilptų tik viena būseną. Tinklelio tūryje atsitiktinai generuojamos lokalizuotos būsenos su tam tikru tankiu N_{Loc} ir nespindulinės rekombinacijos centrai su tankiu N_{NRC} . Visos būsenos su energija, didesne nei mobilumo kraštas E_{me} yra laikomos laisvomis. Lokalizuotų būsenų energijos yra generuojamos žemiau E_{me} pagal Gausso pasiskirstymą [17][21]:

$$f(E) = \frac{1}{\sigma\sqrt{2\pi}} e^{-\frac{1}{2}\left(\frac{E-E_{me}}{\sigma}\right)^2} \quad 1.1.$$

Čia σ yra lokalizuotų būsenų energijos standartinio nuokrypio parametras. Erdvinės lokalizuotų būsenų ir NRC koordinatės parenkamos atsitiktinai. Siekiant užtikrinti spartesnę būsenų bei jas užimančių dalelių paiešką buvo taikoma medžio tipo hierarchinės duomenų struktūros.

1.3. Dalelių generavimas ir atnaujinimas

Šiame darbe dalelėmis vadinami objektai yra elektronai ir skylės arba lokalizuota elektrono ir skylės pora (eksitonai). Laisvieji krūvininkai gali laisvai judėti erdvėje virš mobilumo krašto, tuo tarpu lokalizuoti eksitonai yra erdviškai pririšti prie lokalizuotų būsenų ir gali judėti tik šokuodami per lokalizuotas būsenas. Dalelės generuojamos tik kiekvieno žingsnelio pradžioje prieš atnaujinant jau esamų dalelių būsenas. Laisvos dalelės visada sukuriama poromis (elektronas-skylė) su tais pačiais erdviniais parametrais. Tuo tarpu eksitonai generuojami kaip viena dalelė.

Skaičiavimo metu galimi trys žadinimo režimai: impulsinis, kvazi-nuostovus ir pastovios koncentracijos. Žadinant impulsiniame režime, dalelės

yra generuojamos tik naujo ciklo pradžioje ($t = 0$). Kvazinuostoviam režime daleles generuojamos su tam tikra tikimybe viso skaičiavimo metu. Pastovios koncentracijos režimas užtikrina, kad kiekvieno laiko žingsnelio pradžioje esamų dalelių skaičius yra fiksuotas.

Dalelių atnaujinimą galimas modeliuojamas dviejų atsitiktinių skaičių generavimu. Pirmasis etapas skirtas nustatyti, ar ši dalelė per esantį laiko žingsnelį gali atlikti bent vieną įvykį. Jeigu gali, tada naudojant antrą atsitiktinį skaičių iš lentelės su visais įmanomais procesais atrenkamas atitinkamas įvykis. Tikimybė W , kad bent vienas procesas įvyks per laiko vienetą Δt yra aprašoma taip:

$$W = \int_0^{\Delta t} v \exp(-vt) dt = 1 - \exp(-v\Delta t) \quad 1.2.$$

Čia $v = \sum v_i$ yra visų įmanomų įvykių spartos suma. Laiko žingsnis skaičiavimuose Δt yra parenkamas pakankamai mažas, kad užtikrintų, jog tik vienas įvykis atsitiktų per laiko žingsnelį. Ši tikimybė nepriklauso nuo pradinio laiko nustatymo. Įvykis yra laikomas priimtu, jei pastarojo tikimybė W yra didesnė nei atsitiktinai generuotas skaičius $P \in (0, 1]$. Antrasis atsitiktinis skaičius $R \in (0, 1]$ skirtas nustatyti, kuris procesas (su indeksu i) įvyko naudojant kumuliatyvinę pasiskirstymo funkciją:

$$\sum_{i=1}^{n-1} v_i < vR \leq \sum_{i=1}^n v_i \quad 1.3.$$

Šio tipo paieškas galima atlikti kur kas greičiau taikant binominės struktūras. Svarbu, kad tokio tipo vienai daleliai skaičiavimus kur kas efektyviau atlikti generuojant atsitiktinį laiko intervalą dt , po kurio procesas įvyks:

$$dt = \frac{1}{v} \ln\left(\frac{1}{P}\right) \quad 1.4.$$

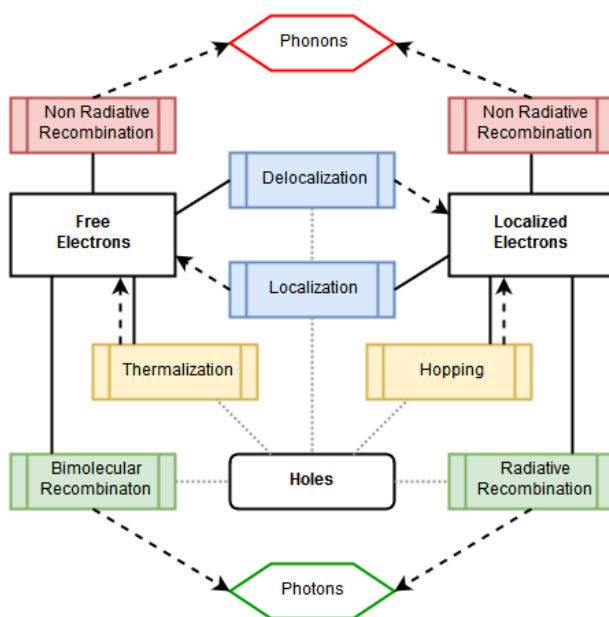
Skirtingai nuo prieš tai aprašyto metodo, čia praleidžiami laiko žingsneliai, per kuriuos nevyksta jokie dalelių būsenos pakitimai.

1.5. Įvykių tipai

Paveiksle 1.1 parodyti visi procesai, į kuriuos atsižvelgiama mūsų modelyje. Šiuos procesus galima suskirstyti į trys kategorijas. Į pirmąją kategoriją patenka įvykiai, kurių metu dalelė yra eliminuojama. Norint supaprasti modelį, tikimybių skaičiavimai buvo atlikti elektronui ir buvo laikoma, kad elektronai rekombinuoja kartu su skylė. Vienintelis skirtumas tarp spindulinės ir nespindulinės rekombinacijos yra tai, kad fotonas yra generuojamas tik pirmuoju atveju. Kaupiant informaciją apie išspinduliuotų fotonų energiją ir laiką gaunami fotoluminescencijos spektrai ir kinetikos.

Antrajai grupei priskiriami procesai, kurie lemia nepusiausvirųjų krūvininkų pernašą. Įvykio metu gali pasikeisti dalelės koordinatės bei energija. Laisvi elektronai ir skylės gali judėti nepriklausomai, tačiau lokalizuoti eksitonai juda kaip elektronų ir skylių poros.

Trečioji kategorija aprašo, kaip laisvos ir lokalizuotos dalelės gali keistis tarpusavyje.



Pav 1.1. Schematiškai atvaizduoti galimi dalelių įvykiai.

Lokalizuotomis dalelėmis vadiname elektrono ir skylės porą, esančią lokalizuotoje būsenoje. Šiuos būsenos turi fiksuotas energijas ir koordinates. Pagrindinės lokalizuotų krūvininkų savybės yra spindulinė rekombinacija ir šokavimas per lokalizuotas būsenas, tačiau taip pat reikia atsižvelgti į

delokalizacija ir galimus tunelinius šuolius į nespindulinės rekombinacijos centrus.

Šokavimo tarp dviejų lokalizuotų centrų sparta aprašoma klasikine Miller-Abraham formule [59]:

$$v_{i \rightarrow j} = v_0 \exp\left(-\frac{2R_{i \rightarrow j}}{\alpha}\right) \exp\left(-\frac{(E_j - E_i) + |E_j - E_i|}{2k_B T}\right) \quad 1.5.$$

Čia v_0 iššokimo sparta (angl. *attempt to escape frequency*), kuri siejasi su šiluminių virpesių dažniu. Tuneliavimo tikimybė priklauso nuo atstumo tarp dviejų būsenų R_{ij} ir banginių funkcijų persiklojimo parametro α . Pradinės ir galutinės būsenos energijos E_i ir E_j nulemia šiluminio šuolio per barjerą tikimybę esant šiluminei energijai $k_B T$.

Norint apskaičiuoti bendrą šokavimo tikimybę reikia susumuoti visų įmanomų šuolių spartas:

$$v_{hopp} = \sum_{i \neq j}^{N_{loc}} v_{i \rightarrow j} \quad 1.6.$$

Kadangi šokavimo sparta nuo atstumo priklauso eksponentiškai, labai toli esančias būsenas modeliavimo metu galima atmesti.

Spindulinės rekombinacijos sparta lokalizuotiems krūvininkams yra aprašoma kaip tiesinė rekombinacija:

$$v_{rad} = \frac{1}{\tau_{rad}} \quad 1.7$$

kur τ_{rad} - spindulinės rekombinacijos trukmė. Laikoma, kad ši sparta nepriklauso nuo energijos [60].

Miller-Abraham išraišką galima pritaikyti ir apskaičiuojant šuolių į NRC arba delokalizacijos spartas. Modelyje priimama, kad nespindulinės rekombinacijos centrų energija daug žemesnė, tad nespindulinės rekombinacijos spartą lokalizuotoms dalelėms galima perrašyti kaip:

$$v_{nonrad} = v_0 \sum_{NRC} \exp\left(-\frac{2R_{i \rightarrow NRC}}{\alpha}\right) \quad 1.8.$$

Delokalizacijos procesas aprašo daleles, kurios išsoka iš lokalizuotos būsenos į energetiškai aukštesnę laisvą būseną ties mobilumo kraštu E_{me} toje pat erdvės vietoje:

$$v_{deloc} = v_0 \exp\left(-\frac{(E_{me} - E_i)}{k_B T}\right) \quad 1.9.$$

Laisvieji elektronai ir skylės gali judėti nepriklausomai, ir jų energija nėra fiksuota. Krūvininkų sąveikos su fononais sparta ženkliai didesnė nei visų kitų procesų. Dėl to praktiškai neįmanoma nusakyti, kokią energiją turi dalelė fiksuotu laiko momentu. Siekiant to išvengti laisvųjų krūvininkų energija yra generuojama naudojant atsitiktinių skaičių generatorių su Fermi-Dirako pasiskirstymu

$$F(E, T) = \frac{1}{\exp\left(\frac{E - E_F}{k_B T}\right) + 1} \quad 1.10$$

Čia, T – temperatūra, k_B – Boltzmanno konstanta, o E_F – kvazifermi lygmens energija, kuri yra skaitmeniškai apskaičiuojama naudojant sąryšį

$$n(E_F) = \int_{-\infty}^{\infty} F(E, E_F) g(E) dE \quad 1.11.$$

kur $g(E)$ yra būsenų tankio funkcija. Tuo tarpu koordinatės yra atnaujinamos taikant atsitiktinį Brauno judėjimą.

Pagrindinis spindulinės rekombinacijos mechanizmas laisviems krūvininkams yra tarpjuostiniai šuoliai. Tai kitaip vadinama bimolekuline rekombinacija. Spartos yra skaičiuojamos elektronų atžvilgių, tad formulė perrašoma kaip:

$$v_{non} = v_{cap} N_{NRC} \equiv v_{th} \sigma N_{NRC} \quad 1.12$$

Čia, p – skylių koncentracija, o B^* yra normuotas bimolekulinės rekombinacijos koeficientas. Sumuojant per visus esančius elektronus, gaunamas kvadratinis narys proporcingas sandaugai np .

Yra daug skirtingų būdų aprašyti nespindulinės rekombinacijos spartai. Šiame modelyje mes apsiribojame paprasčiausia tiesine rekombinacija.

$$v_{non} = v_{cap} N_{NRC} \equiv v_{th} \sigma N_{NRC} \quad 1.13$$

kur N_{NRC} yra nespindulinės rekombinacijos centrų tankis.

Analogiška procedūra atliekama ir skaičiuojant lokalizacijos spartą.

$$v_{loc} = v_{cap} N_{loc} \quad 1.14.$$

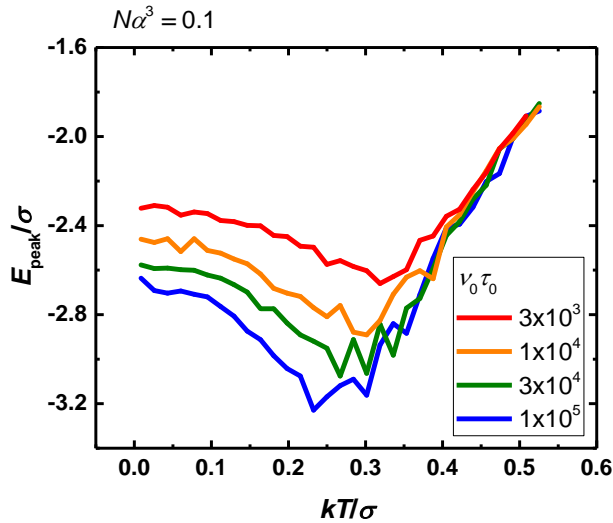
2. REZULTATAI IR JŲ APTARIMAS

2.1. Lokalizuotų krūvininkų dinamika AlGaIn

Šiame skyriuje nagrinėjama lokalizuotų krūvininkų dinamika trinariuose nitridiniuose junginiuose esant silpnam sužadimui. Šiuo tikslu buvo naudojama sukurta skaičiavimo programa, paremta kinetinio Monte – Karlo algoritmu. Paskaičiuotos fotoluminescencinės priklausomybės buvo lyginamos su kolegų Fotonikos ir nanotechnologijų institute išmatuotais rezultatais. Tiriamas bandinys buvo $\text{Al}_{0.65}\text{Ga}_{0.35}\text{N}$ epitaksinis sluoksnis užaugintas MEMOCVD metodu ant safyro padėklo. Matavimai buvo atlikti žadinant YAG:Nd lazerio spinduliuotės 5 harmonikos (213 nm) 4 ns trukmės impulsais. Temperatūra buvo keičiama nuo 8 iki 300 K.

2.1.1. Fotoluminescencijos spektro modeliavimas

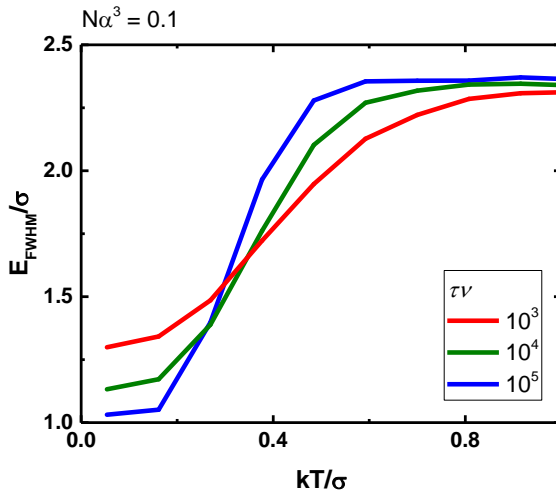
Modeliuojant fotoluminescencijos spektrus buvo naudojamas žemo žadinimo artinys. Esant mažam fotogeneruotų krūvininkų tankiui, pagrindines optines savybes lemia lokalizuotų krūvininkų spindulinė rekombinacija. Tokioje situacijoje spektro forma beveik nepriklauso nuo nespindulinės rekombinacijos ar lokalizacijos/delokalizacijos spartų. Norint aprašyti juostos pusplėčio ar smailės padėties priklausomybes nuo temperatūros dažniausiai užtenka dviejų parametrų rinkinio, $\nu_0\tau_0$ ir $N\alpha^3$, kuris, atitinkamai, nusako eksitonų šokavimo procesą laike ir erdvėje [8][57]. Paveikslas 2.1.1 rodo sumodeliuotą FL piko poslinkio priklausomybę nuo temperatūros. Stiprios lokalizacijos požymis yra ženkliai mažesnė FL juostos spektrinė padėtis lyginant su mobilumo krašto energija. Žemuose temperatūrose lokalizuoti krūvininkai beveik nejuda. Augant temperatūrai, dalelės gali peršokti į artimas žemesnės energijos būsenas, dėl ko spektras slenka į raudonąją pusę. Igaunant daugiau energijos dalelės sugeba įveikti potencialinį barjerą, pradeda laisviau judėti ir galų gale tolygiai pasiskirsto per visas lokalizuotas būsenas, kas lemia jog FL juostos smailė artėja prie mobilumo krašto energijos. Toks elgesys dažnai vadinamas S-formos priklausomybe ir yra tipinis trinariams nitridiniams junginiams.



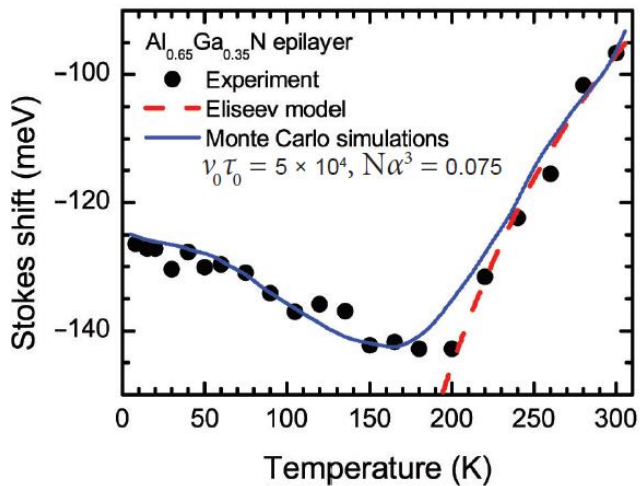
Pav 2.1.1. Fotoluminescencijos juostos smailės padėties priklausomybė nuo temperatūros, esant skirtingoms parametro $v_0\tau_0$ vertėms.

Paskaičiuotas FL juostos pusplotis atvaizduotas pav. 2.1.2. Kylant temperatūrai juosta plečiasi, tačiau vėliau šis plėtėjimas įsisotina. Tai lemia lokalizuotų būsenų energetinis pasiskirstymas. Tapatinant su eksperimentiniais duomenimis, gautos reikšmės yra mažesnės, nes neįskaito dvigubos skalės potencialo formos ir fononinės sąveikos. Pastaroji ypač stipriai iškraipo FL spektrą aukštuose temperatūrose. Įskaičius šiuos veiksnius stebima kreivė pradžioje auga, vidutinėse temperatūrose įsisotina, o paskui vėl auga dėl sąveikos su fononais. Toks elgesys vadinamas W-formos priklausomybe.

Didesnės $v_0\tau_0$ ir $N\alpha^3$ reikšmės lemia stipriau pasireiškiančias „S“ ir „W“ formas. Tapatinant sumodeliuotas kreives su eksperimentiniais rezultatais galime nustatyti pagrindinius lokalizacijos parametrus, kuriais bus paremti tolimesni skaičiavimai. Paveikslai 2.1.3 ir 2.1.4 vaizduoja tapatinimo rezultatus. Juose pateiktos ir gautų parametų reikšmės.

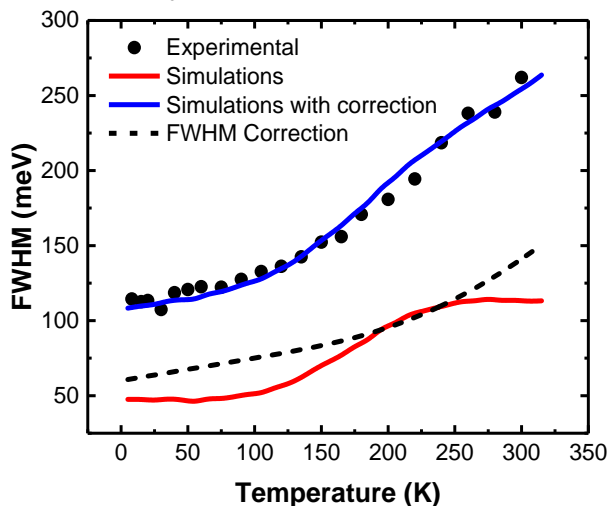


Pav 2.1.2. Fotoluminescencijos juostos pusplėčio priklausomybė nuo temperatūros, esant skirtingoms parametro $v_0\tau_0$ vertėms.



Pav 2.1.3. Išmatuota (taškai) ir sumodeliuota (linija) fotoluminescencijos juostos smailės priklausomybė nuo temperatūros AlGaIn epitaksiniam sluoksnyje. [P3].

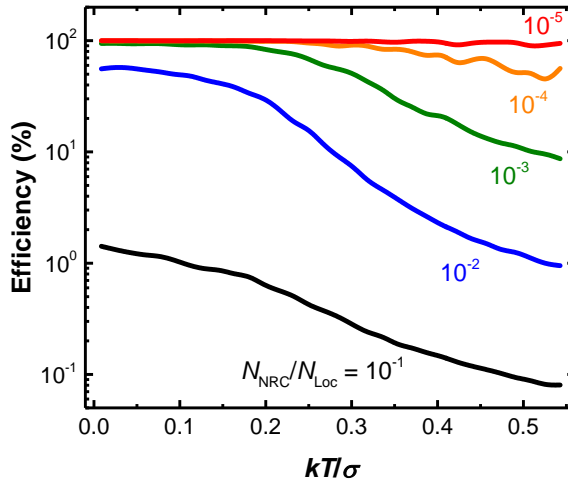
$$\Gamma = 60\text{meV} \quad E_{\text{LO}} = 97\text{meV} \quad \beta = 0.15\text{meV/K} \quad \gamma = 1500\text{meV}$$



Pav 2.1.4. Išmatuota (taškai) ir sumodeliuota (raudona linija) fotoluminescencijos juostos smailės priklausomybė nuo temperatūros AlGaN epitaksiniame sluoksnyje. Mėlyna linija rodo pusplėčio priklausomybę įskaičiuojant sklaidą fononais (punktyrinė linija).

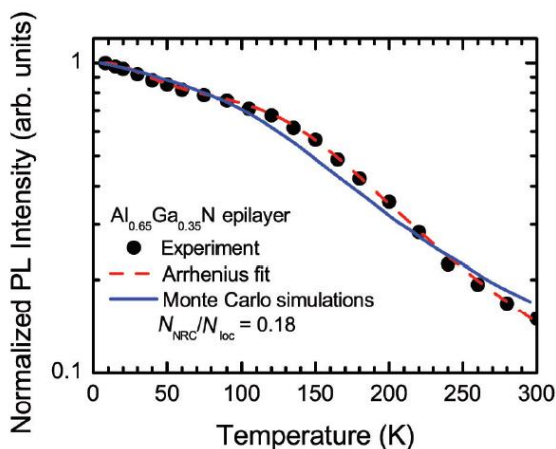
2.1.2. Fotoluminescencijos našumo priklausomybės nuo temperatūros modeliavimas

Skirtingai nei fotoluminescencijos spektro formos skaičiavimuose, norint nustatyti intensyvumo priklausomybę nuo temperatūros reikia atsižvelgti ir į nespindulinę rekombinaciją. Šiame modelyje mes tyrinėjome du galimus nespindulinės rekombinacijos mechanizmus: eksitonų tuneliavimas į nespindulinės rekombinacijos centrus (NRC) ir laisvųjų krūvininkų pagavimas į NRC. Paveiksle 2.1.5 atvaizduotos FL intensyvumo priklausomybės nuo temperatūros įskaičiuojant nespindulinę rekombinaciją ir esant skirtingoms NRC tankiams. Krūvininkų tuneliavimą į NRC daugiausiai lemia pastarųjų tankis, pats procesas gali pasireikšti net itin žemose temperatūrose. Tuo tarpu laisvųjų krūvininkų pagavimas į NRC eksponentiškai priklauso nuo šiluminės energijos ir lokalizuotų būsenų energijos dispersijos parametro santykio. Ši savybė pasireiškia dėl to, jog, esant stipriai lokalizacijai, laisvų krūvininkų beveik nėra, o laisvomis elektronu ir skylės poromis tampa tik eksitonai, turintys pakankamai energijos įveikti barjerą.



Pav 2.1.5. Modeliuotos fotoluminescencijos efektyvumo priklausomybės nuo temperatūros esant skirtingiems nespindulinės rekombinacijos centrų tankiams.

Taigi, pasirenkant teisingus lokalizacijos parametrus, gautus iš FL spektro tapatinimo, ir varijuojant nespindulinės rekombinacijos centrų ir lokalizuotų būsenų santykį galime sumoduliuoti FL intensyvumo priklausomybę AlGaIn epitaksiniam sluoksnyje (žr. 2.1.6. pav.). Šią eksperimentinę priklausomybę taip pat galima aprašyti naudojant Arenijaus formulę su dviem aktyvacijos energijoms, lygioms 6 ir 69 meV. Darbo metu nustatyta, kad ženkliai mažesnė aktyvacijos energija lyginant su potencialo fluktuacijų dispersija atspindi spartų lokalizuotų krūvininkų tuneliavimą į nespindulinės rekombinacijos centrus. Tuo tarpu antrasis energijos barjeras siejasi su laisvų krūvininkų pagavimu į nespindulinės rekombinacijos centrus.



Pav. 2.1.6. Išmatuota (taškai) ir suskaičiuota (mėlyna linija) fotoluminescencijos intensyvumo priklausomybė nuo temperatūros AlGaN epitaksiniame sluoksnyje. Punktyrine linija vaizduoja priklausomybę pagal Arenijaus dėsnį [P3].

2.1.3. Išvados

Sumoduliuota krūvininkų dinamika AlGaN epitaksiniame sluoksnyje žemo žadinimo sąlygomis. Skaičiavimai atlikti pagal modelį, aprašantį sistemą, sudarytą iš laisvų ir lokalizuotų krūvininkų. Naudotas kinetinio Monte – Karlo algoritmas. Modeliuojant temperatūrinės fotoluminescencijos spektro priklausomybes ir tapatinant jas su eksperimentiniais rezultatais įvertintos lokalizaciją apibūdinančių parametų reikšmės. Jomis remiantis sumodeliuotos FL našumo temperatūrinės priklausomybės. Šie rezultatai leidžia nusakyti sąsajas tarp parametų Arenijaus formulėje ir krūvininkų dinamikos parametų: mažesnioji aktyvacijos energija atspindi spartų lokalizuotų krūvininkų tuneliavimą į nespindulinės rekombinacijos centrus, o antrasis energijos barjeras siejasi su laisvųjų krūvininkų pagavimu į nespindulinės rekombinacijos centrus.

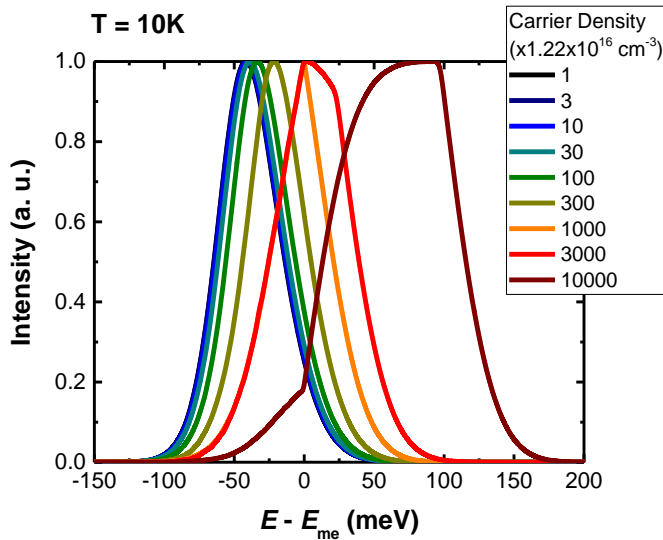
2.2. Laisvųjų ir lokalizuotųjų krūvininkų dinamikos AlGaN kristale modeliavimas

Šiame skyriuje tyrinėjama laisvųjų ir lokalizuotųjų krūvininkų dinamika trinariuose nitridiniuose dariniuose esant skirtingam nepusiausvirųjų krūvininkų tankiui. Šiam tikslui naudojamas daugiadalelis kinetinio Monte – Karlo modelis, kuriame laikui bėgant dalelių skaičius gali keistis. Papildomai atsižvelgta į lokalizacijos spartą kintant lokalizuotųjų būsenų užpildos sąlygoms. Laikoma, kad lokalizuota elektrono skylės pora gali susidaryti tik kai abi dalelės yra netoli laisvos lokalizuotos būsenos. Siekiant paaiškinti efektyvumo nuokrytį, šalia jau aptartų fotoluminescencinės spektro temperatūrinių savybių modeliuojama FL efektyvumo priklausomybė nuo sužadavimo kvazistacionariame režime.

Siekiant pagrįsti modelio veiksnumą modeliuojami rezultatai buvo tapatinami su išmatuotomis priklausomybėmis. Tapatinimui buvo pasirinktas ant 1.2 μm storio $\text{Al}_{0.49}\text{Ga}_{0.51}\text{N}$ padėklo užaugintas $\text{Al}_{0.35}\text{Ga}_{0.65}\text{N}$ bandinys, sudarytas iš dešimties sluoksnių 5 nm storio kvantinių lakštų, atskirtų 11.5 nm $\text{Al}_{0.49}\text{Ga}_{0.51}\text{N}$ barjeriais. Matavimai buvo atlikti žadinant YAG:Nd lazerio spinduliuotės 4 harmonikos (266 nm), 4 ns trukmės impulsais. Matavimo metu buvo keičiama temperatūra nuo 8 iki 300 K bei žadinimo galios tankis nuo 0.4 kW/cm^2 iki 14 MW/cm^2 .

2.2.1. Fotoluminescencijos spektro modeliavimas

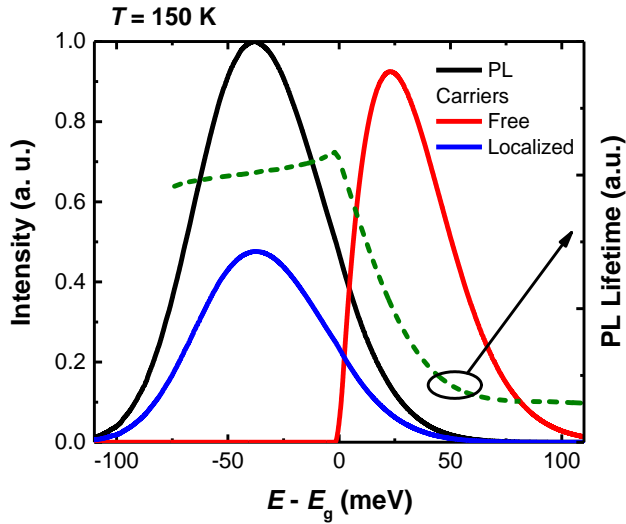
III grupės nitridinių šviestukų spinduliuotės spektras priklauso nuo žadinimo intensyvumo [76]. Pagrindinė šio efekto priežastis yra lokalizuotųjų būsenų užpildymas. Siekiant nustatyti, kaip sužadinimas paveikia FL formą, buvo modeliuojami FL spektrai esant skirtingiems fotosužadintųjų krūvininkų tankiams (pav. 2.2.1). Esant nedideliame sužadimui, FL forma beveik nekinta ir atkartoja viendalelio kMK modeliavimo rezultatus. Didėjant dalelių koncentracijai, juostos smailės padėtis pradeda judėti link mėlynosios spektro pusės. Tuo pačiu žemųjų energijų šlauto forma vis labiau atspindi lokalizuotųjų būsenų energetinį pasiskirstymą. Pasiekus krūvininkų tankius, kai visos lokalizuotos būsenos yra užimtos, tolesnę spektro formą lemia būsenų tankio ir laisvųjų krūvininkų pasiskirstymo funkcijos sandauga.



Pav. 2.2.1. AlGaIn kvantinių lakštų fotoluminescencijos spektrai sumodeliuoti 10K temperatūroje.

Aukštesnėse temperatūrose didėjant krūvininkų šiluminei energijai, juostos plotis didėja. Taip pat stiprėja sklaida fotonais, tad vien tik iš FL spektro sunku nusakyti, kokio tipo dalelės turi didžiausią įtaką. Taikomas modelis leidžia atskirti laisvų ir lokalizuotų krūvininkų įtaką fotoluminescencijos spektrui.

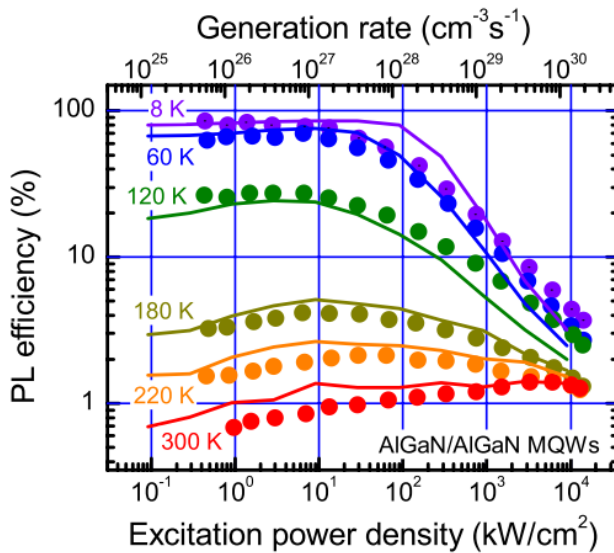
Paveiksle 2.2.2 pavaizduotas tipinis suskaičiuoti laisvų ir lokalizuotų krūvininkų pasiskirstymai pagal energiją kartu su FL intensyvumo ir gyvenimo trukmės spektrais. Nepaisant gana didelės laisvųjų krūvininkų tankio, FL spektras atkartoja lokalizuotų krūvininkų pasiskirstymą. Nors bimolekulinės rekombinacijos įtaka stiprėja, ji vis dar kelis kartus silpnesnė nei eksitonų įtaka. Kita vertus, lokalizuoti krūvininkai dažniausiai yra izoliuoti nuo nespindulinės rekombinacijos centrų. Atsižvelgiant į tokių sistemos elgesį galima lengviau nusakyti, kokia bus FL efektyvumo priklausomybė nuo žadinimo.



Pav 2.2.2. Sumodeliuotas fotoluminescencijos spektras (juoda linija) ir pasiskirstymas pagal energiją laisviems (raudona) ir lokalizuotiems (mėlyna) krūvininkams. Punktyrinė linija vaizduoja fotoluminescencijos gyvavimo trukmę

2.2.2. Fotoluminescencijos našumo modeliavimas

Siekiant aprašyti FL našumo priklausomybę nuo žadinimo intensyvumo visų pirma reikia atlikti 2.1. skyriuje aprašytą procedūrą. Tapatinant fotoluminescencijos juostos smailės padėtis, puspločio bei intensyvumo temperatūrinės priklausomybes su modeliavimo metu gautais rezultatais, nustatėme pagrindinius lokalizuotų būsenų ir nespindulinės rekombinacijos centrų parametrus. Likusieji parametrai, tokie kaip rekombinacijos bei lokalizacijos/delokalizacijos trukmės, parenkamos tapatinant FL efektyvumo priklausomybes nuo žadinimo intensyvumo esant skirtingoms temperatūroms. Paveiksle 2.2.3. pavaizduoti eksperimentiniai ir modeliavimo rezultatai.

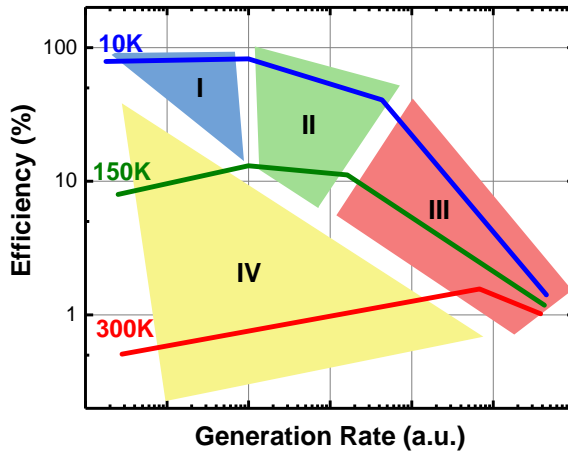


Pav. 2.2.3. Išmatuotos (taškai) ir sumodeliuotos (linijos) fotoluminescencijos našumo priklausomybės nuo žadinimo intensyvumo esant skirtingoms temperatūroms [P1].

Remiantis šiais rezultatais buvo tirta krūvininkų pasiskirstymai pagal energijas ir gyvavimo trukmės bei atskleistos atskirų rekombinacijos procesų įtakos. Išanalizavus šias priklausomybes buvo išskirtos keturios sritys, atitinkančios kokybiškai skirtingą krūvininkų dinamiką. Tai schematiškai atvaizduota 2.2.4. pav.

Pirmoji sritis atitinka sistemą, kurioje beveik visi krūvininkai yra giliai lokalizuoti. Tokia situacija susidaro, kai krūvininkų šiluminė energija yra daug mažesnė už lokalizuotų būsenų energinę dispersiją, o krūvininkų tankis yra mažesnis nei lokalizuotų būsenų tankis. Tokiomis sąlygomis vidinis kvantinis našumas yra gana didelis, o FL juostos smailės energija yra mažesnė nei mobilumo krašto.

Didėjant krūvininkų tankiui, užsipildo vis daugiau lokalizuotų būsenų. Tokią situaciją aprašo antroji sritis. Dėl neužimtų lokalizuotų būsenų skaičiaus sumažėjimo didėja tikimybė krūvininkams patekti į nespindulinės rekombinacijos centrus. Taip pat didėja skaičius dalelių, esančių sekliose būsenose, iš kurių dėl mažesnio energijos barjero lengviau delokalizuotis į laisvasias būsenas. FL efektyvumas pradeda kristi, o juostos smailė slenkasi į didesnių energijų pusę.



Pav. 2.2.4. Keturios sritys našumo priklausomybės nuo nepusiausvirųjų krūvininkų generacijos spartos ir temperatūros diagramoje, atitinkančios kokybiškai skirtingą krūvininkų dinamiką [P1].

Toliau augant krūvininkų tankiui, pasiekama situacija, kai neužimtų lokalizuotų būsenų praktiškai nebelieka. Todėl kiekviena naujai generuota elektrono ir skylės pora lieka nelokaluota. Ši trečioji sritis atitinka našumo nuokryčio situaciją. Laisvų krūvininkų koncentracija dar nepakankama pasireikšti stipriai tarpjuostinei rekombinacijai, todėl šioje srityje dominuoja krūvininkų pagavimas nespindulinės rekombinacijos centrais. Toliau augant žadimui, lokalizuotų krūvininkų tankio santykis su laisvųjų krūvininkų tankiu mažėja, todėl efektyvumas stipriai mažėja. Svarbu pažymėti, kad našumo nuokryčio efektas sumodeliuotas netgi neįskaitant Ožė rekombinacijos, kuria šis nuokrytis dažniausiai yra aiškinamas.

Situaciją, kai temperatūra yra santykinai aukšta, o nepusiausvirųjų krūvininkų tankis mažas, atitinka ketvirtoji sritis. Nepaisant didelio neužimtų lokalizuotų būsenų tankio, čia dominuoja laisvos dalelės. Tai lemia didelis šiluminis greitis. Elektronas ir skylė stipriai išskiriami erdvėje, dėl ko eksitonui sunkiau susidaryti. Didėjant krūvininkų tankiui, tikimybė, kad laisvi elektronas ir skylė susitiks prie neužimtos lokalizuotos būsenos auga. Formuojantis lokalizuotiems eksitonams, atitinkamai didėja spindulinės rekombinacijos atvejų, todėl našumas nežymiai auga. Priklausomai nuo temperatūros ir lokalizacijos sąlygų ši sritis gali palaipsniui pereiti į antrąją arba trečiąją.

2.2.3. Išvados

Sukurtas kinetinio Monte – Karlo modelis buvo pritaikytas aprašyti sistemai, susidedančiai iš laisvų ir lokalizuotų krūvininkų. Rezultatai leido įvertinti pagrindinius veiksnius, lemiančius fotoluminescencijos spektro priklausomybę nuo temperatūros ir nustatyti efektyvumo nuokryčio priežastį. Parodyta, kad pastarąjį efektą galima aprašyti deramai aprašius lokalizacijos ypatumus netgi neįskaitant Ožė rekombinacijos. Didėjant nepusiausvirųjų krūvininkų tankiui, dominuojanti spindulinė rekombinacija iš lokalizuotų būsenų įsisotina, tuo tarpu laisvų krūvininkų pagavimas į nespindulinės rekombinacijos centrus auga. Pasiekus krūvininkų tankius, prie kurių visos lokalizuotos būsenos yra užpildytos, naujai generuotos dalelės daugiausiai rekombinuoja nespinduliniais kanalais, kas ir lemia efektyvumo nuokrytį. Šias išvadas patvirtina geras modeliavimo rezultatų sutapimas su išmatuotomis fotoluminescencijos parametru priklausomybėmis nuo temperatūros ir jos intensyvumo priklausomybe nuo žadinimo intensyvumo.

2.3. Difuzijos modeliavimas sistemuose su laisvais ir lokalizuotais krūvininkais

Difuzijos koeficientas yra svarbus parametras aprašant krūvininkų dinamiką trinariuose III grupės nitridų dariniuose, tokiose kaip AlGaN ar InGaN. Eksperimentiniai difuzijos matavimai yra gana sudėtingi, o pats koeficientas netiesiškai priklauso nuo sužadintų krūvininkų tankio bei lokalizacijos sąlygų. Šiame skyriuje aptartas kinetinio Monte – Karlo modelio pritaikymas modeliuojant difuzijos koeficiento priklausomybę nuo žadinimo intensyvumo. Gauti rezultatai lyginami su eksperimentiškai išmatuotais duomenimis InGaN kvantiniuose lakštuose.

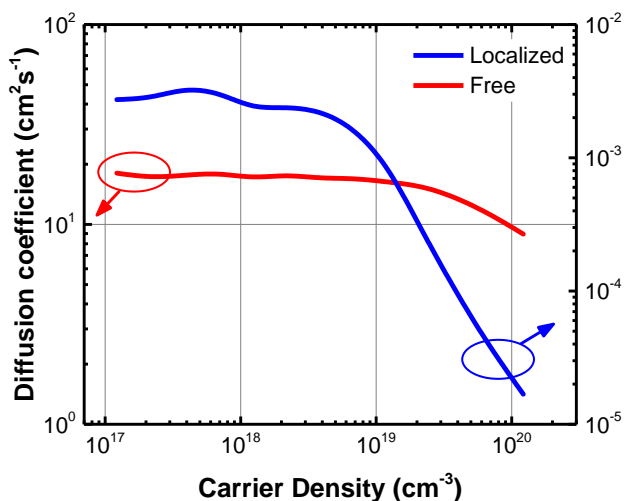
Tapatinimui buvo pasirinkti m plokštuma auginti, 8 nm storio $\text{In}_{0.13}\text{Ga}_{0.87}\text{N}$ kvantiniai lakštai. Eksperimentiniai rezultatai buvo gauti VU Fotonikos ir nanotechnologijų instituto kolegų panaudojant šviesa sužadintų dinaminių gardelių (LITG) metodiką, leidžiančią vienu metu išmatuoti ambipolinį difuzijos koeficientą ir nepusiausvirųjų krūvininkų gyvavimo trukmę [82].

2.3.1. Difuzijos modeliavimas

Siekiant aprašyti difuzijos koeficientą sistemoje su laisvais ir lokalizuotais krūvininkais aukščiau aprašytas krūvininkų lokalizaciją ir rekombinaciją aprašantis tokios sistemos modelis atlikti skaičiavimus pasitelkiant kinetinio Monte – Karlo metodą buvo optimizuotas atlikti skaičiavimus esant didesniems dalelių skaičiams. Be to, šiuose skaičiavimuose buvo renkama statistika apie dalelių nukeliautą atstumą ir gyvavimo trukmę. Pirmu artėjimu buvo modeliuojama, kaip difuzijos koeficientas priklauso nuo žadinimo, kai sistemoje egzistuoja tik vieno tipo dalelės. Ši priklausomybė pateikta 2.3.1. pav. Tik laisviems krūvininkams sumodeliuotas difuzijos koeficientas prie žemų žadinimų beveik nepriklauso nuo krūvininkų tankio ir yra apie $10 \text{ cm}^2/\text{s}$. Nedidelis difuzijos koeficiento mažėjimas atsiranda dėl spartėjančios juosta-juosta rekombinacijos, kuri sutrumpina dalelių gyvenimo trukmę.

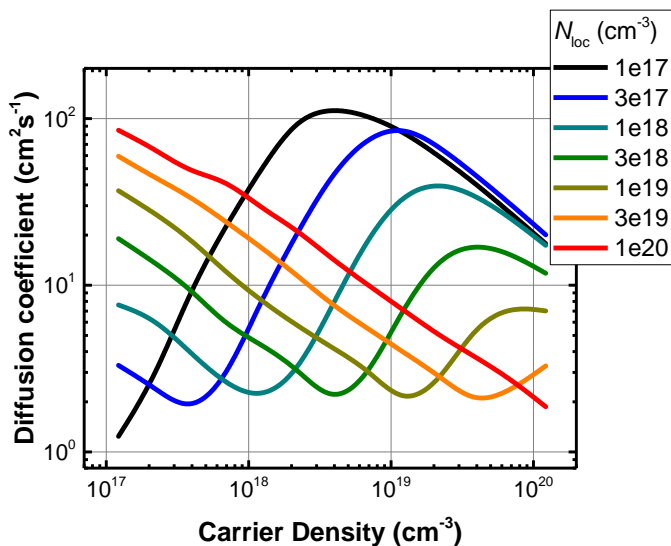
Sistemoje, kurioje egzistuoja tik lokalizuoti krūvininkai, difuzija yra daug mažesnė. Difuzijos koeficientas esant mažiems tankiams išlieka pastovus, tačiau pradeda stipriai priklausyti pasiekus tam tikrą krūvininkų koncentraciją. Toks elgesys siejamas su lokalizuotų būsenų užpilda, kadangi dalelių šokavimui per lokalizuotas būsenas yra būtina, kad galutinė būsena privalo būtų laisva. Santykinai maža difuzijos koeficiento vertė tokiomis sąlygomis

yra nulemta gana didelio lokalizuotų būsenų energijos dispersijos parametro lyginant su šilumine energija.



Pav. 2.3.1 Sumodeliuota difuzijos koeficiento priklausomybė nuo krūvininkų tankio tik laisvoms (raudona linija, kairioji skalė) ir tik lokalizuotoms (mėlyna linija, kairioji skalė) dalelėms.

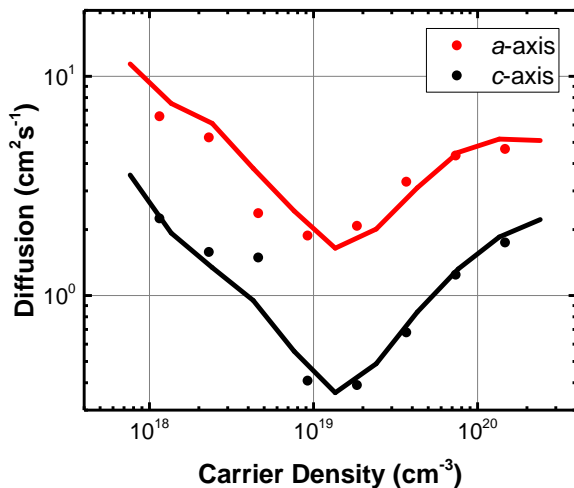
Modeliuojant difuzijos koeficientą sistemoje su laisvais ir lokalizuotais krūvininkais svarbus parametras yra lokalizuotų būsenų tankis. Difuzijos koeficiento priklausomybė nuo krūvininkų tankio prie skirtingo lokalizuotų būsenų tankio parodyta 2.3.2. pav. Bendra tendencija esant skirtingiems lokalizuotų būsenų tankiams yra difuzijos koeficientas mažėjimas didėjant nepusiausvirųjų krūvininkų tankiui. Šis ypatumas yra susijęs su augančia tikimybe susidaryti lokalizuotų dalelių poroms didėjant laisvųjų koncentracijai. Kai visos lokalizuotos būsenos tampa užpildytos, difuzijos koeficientas pasiekia savo mažiausią reikšmę. Pažymėtina, kad mažiausia difuzijos koeficiento vertė beveik nepriklauso nuo lokalizuotų būsenų tankio, nepaisant to, jog vidutinis atstumas tarp šių būsenų keičiasi. Tai parodo, kad šiuo atveju krūvininkų šokavimas nėra lemiantis krūvininkų dinamikos faktorius. Toliau didėjant žadinimo intensyvumui, difuzijos koeficientas auga, nes vis didesnė dalis dalelių tampa laisvos ir lengviau juda. Prie dar didesnių krūvininkų tankio stebimas difuzijos kritimas yra susijęs su bimolekulinės rekombinacijos stiprėjimu, mažinančiu dalelių gyvavimo trukmę.



Pav. 2.3.2. Sumodeliuota difuzijos koeficiento priklausomybė nuo krūvininkų tankio esant skirtingoms nespindulinės rekombinacijos centrų tankiams.

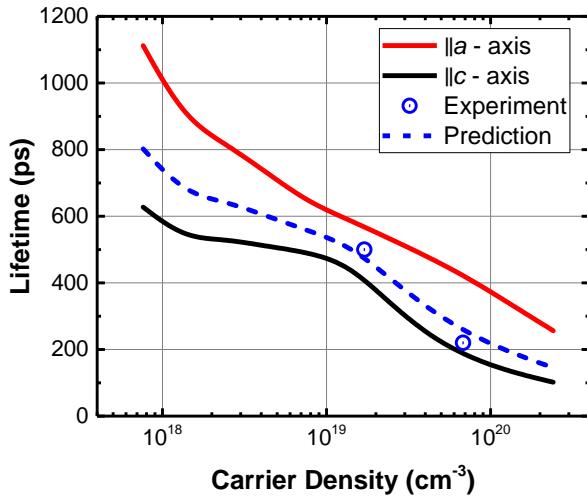
2.3.2. Modeliavimo rezultatų tapatinimas su eksperimentiniais

Tapatinant suskaičiuotas difuzijos koeficiento priklausomybes su eksperimentiniais rezultatais buvo atsižvelgta į sunkiųjų ir lengvųjų skylių įtaką lokalizacijos energijai. Modeliavimo rezultatai gana gerai sutampa su eksperimentiniais (žr. 2.3.3 pav.). Buvo nustatytas lokalizuotų krūvininkų tankis – 10^{19}cm^{-3} , o lokalizacijos energija 75 ir 120 meV, atitinkamai lengvosios ir sunkiosios skylėms. Geriausiais sutapimais su eksperimentiniais rezultatais buvo gautas 200 ps spindulinės rekombinacijos trukmei, o nespindulinės rekombinacijos trukmės prilygintos 40 ps lengvoms ir 200 ps sunkioms skylėms. Skirtumas tarp laisvųjų dalelių pagavimo į nespindulinės rekombinacijos centrus gali būti paaiškintas pastarųjų masės skirtumu, bei tuo jog modelis neatsižvelgia į galimus skylių mainus tarp valentinių pajuosčių. Sutapatinus modeliavimo duomenis su eksperimentiniais rezultatais įmanoma įvertinti kur kas daugiau parametrų nei yra galimybių juos išmatuoti, kas padeda geriau suprasti procesus, vykstančius nitridiniuose dariniuose.



Pav 2.3.3. Išmatuota (taškai) ir sumodeliuota (linijos) ambipolinio difuzijos koeficiento priklausomybė nuo generuoto krūvininkų tankio InGaN daugialypiuose kvantiniuose lakštuose.

Iš modeliavimo rezultatų galima nustatyti, kaip krūvininkų gyvavimo trukmė priklauso nuo sužadintų krūvininkų tankio. Be to, palyginimas su eksperimentiniais rezultatais leidžia patvirtinant modelio tikslumą. Sumodeliuota ir eksperimentiškai išmatuota krūvininkų gyvavimo trukmių priklausomybė nuo generuoto nepusiausvirojo krūvininkų tankio parodyta 2.3.4. pav. Kadangi modelis aprašo lengvasias ir sunkiasias skyles atskirai ir jų koncentracijų santykis nėra žinomi, gauname dvi ribiniais vertes (juoda ir raudona kreivė 2.3.4 pav.). Priimant, kad abiejų dalelių tankiai yra lygūs, galime įvertinti tikrąją gyvenimo trukmę (mėlyna kreivė). Pastaroji gerai sutampa su eksperimentiniais rezultatais.



Pav. 2.3.4. Sumodeliuota (linijos) ir išmatuota (taškai) krūvininkų gyvavimo trukmių priklausomybė nuo nepusiausvirujų krūvininkų tankio InGaN daugialyptuose kvantiniuose lakštuose.

2.3.3. Išvados

Naudodami sukurtą modelį nustatėme, kokie procesai lemia difuzijos koeficiento priklausomybes nuo krūvininkų dinamikos parametrų ir parodėme, kaip šios priklausomybės priklauso krūvininkų lokalizacijos stiprumo. Tapatinant modeliavimo ir matavimo rezultatus nustatyta, kad eksperimentiškai išmatuotų InGaN polinių ir nepolinių kvantinių lakštų difuzijos koeficiento priklausomybė nuo žadinimo iš esmės yra nulemta laisvų ir lokalizuotų dalelių tankio santykiu. Pradinis difuzijos koeficiento mažėjimas yra nulemtas lokalizacijos spartos augimu didėjant laisvų krūvininkų tankiui. Tokia difuzijos priklausomybė gali būti stebima, kai šiluminė energija yra žymiai mažesnė nei potencialo fluktuacijų dispersija, o žemiausia difuzijos koeficiento vertė yra pasiekama, kai visos lokalizuotos būsenos yra užimtos. Toliau augant žadinimui laisvų krūvininkų dalis auga ir atitinkamai didėja ir difuzijos koeficientas.

3. APIBENDRINIMAS

Sukurtas kinetinio Monte – Karlo modelis leidžia aprašyti sistemą sudarytą iš sąveikaujančių nepusiausvirujų laisvų ir lokalizuotų krūvininkų. Skaičiavimais parodyta, kad modelis gerai aprašo eksperimentiškai stebimus vyksmus III grupės nitridiniuose dariniuose. Gauti rezultatai leido išskirti atskirus procesus ir parodyti jų įtaką fotoluminescencijos spektrams ir jos gesimo kinetikai bei aprašyti liuminescencijos parametrų priklausomybes nuo temperatūros ir krūvininkų tankio. Žemiau pateikiami pagrindiniai šio darbo rezultatai.

- 1) Fotoluminescencijos spektro dinamika priklauso nuo santykio tarp šiluminės energijos ir lokalizacijos energetinės dispersijos vertės. Esant stipresnei lokalizacijai, labiau pasireiškia „S“ ir „W“ formos liuminescencijos juostos smailės padėties ir pločio priklausomybėse nuo temperatūros.
- 2) Esant nedideliame nespindulinės centrų arba lokalizuotų būsenų tankiui, fotoluminescencijos intensyvumas yra lemtas laisvųjų krūvininkų pagavimu į nespindulinius rekombinacijos centrus. Augant temperatūrai šis procesas stiprėja.
- 3) Esant dideliems nespindulinės rekombinacijos ir lokalizuotų būsenų tankiams fotoluminescencijos intensyvumą riboja lokalizuotų krūvininkų tuneliavimas į nespindulinės rekombinacijos centrus. Tokiu atveju vidinis kvantinis našumas gali būti labai mažas netgi žemose temperatūrose.
- 4) Fotoluminescencijos intensyvumo priklausomybė nuo temperatūros AlGaIn gali būti aprašoma Arenijaus formule su dviem aktyvacijos energijomis. Pirmoji energija yra mažesnė nei lokalizacijos energija ir atspindi lokalizuotų krūvininkų tuneliavimą į nespindulinės rekombinacijos centrus. Antroji yra aukštesnė ir nulemia laisvųjų krūvininkų pagavimą nespinduliniais rekombinacijos centrais.
- 5) Fotoluminescencijos efektyvumo priklausomybėse nuo nepusiausvirujų krūvininkų tankio galima išskirti keturias sritis. I ir II srityse dominuoja spindulinė rekombinacija iš lokalizuotų

būsenų, o III ir IV srityse – nespindulinė laisvųjų krūvininkų rekombinacija. Augantis nepusiausvirųjų krūvininkų tankis didina delokalizacijos ir lokalizacijos spartas, kas lemia efektyvumo kritimą II srityje ir augimą IV srityje.

- 6) Sistemoje su stipria krūvininkų lokalizacija efektyvumo nuokryčio efektas didėjant nepusiausvirųjų krūvininkų tankiui atsiranda dėl krūvininkų delokalizacijos ir laisvų krūvininkų pagavimo į nespindulinius rekombinacijos centrus. Tai įvyksta prie mažesnių krūvininkų tankių nei reikalingas ženkliai pasireikšti Ožė rekombinacijai.
- 7) Difuzijos koeficientas praktiškai nepriklauso nuo lokalizuotų krūvininkų šokavimo ir yra nulemtas santykio tarp laisvų ir lokalizuotų krūvininkų tankių.
- 8) Augantis nepusiausvirųjų krūvininkų tankis InGaN iš pradžių mažina difuzijos koeficiento vertę dėl stiprėjančios lokalizacijos, bet po to lemia jo augimą dėl didėjančios laisvųjų krūvininkų dalies. Žemiausia koeficiento reikšmė stebima kai visi nepusiausvirieji krūvininkai yra lokalizuoti.
- 9) Difuzijos koeficiento anizotropija nepoliniuose InGaN dariniuose atsiranda dėl lokalizacijos energijos lengvosioms ir sunkiosioms skylėms skirtumo.

CURRICULUM VITAE

Vardas, pavardė	Oleg Kravcov
Gimimo data	1990-09-14
El. paštas	oleg.kravcov@ff.vu.lt

Išsilavinimas

2009-2013	<u>Bakalauro studijos:</u> Fizikos bakalauras Vilniaus Universitetas, Fizikos fakultetas
2013-2015	<u>Magistro studijos:</u> Medžiagotyra ir puslaidininkų fizika, Vilniaus Universitetas, Fizikos fakultetas
2016-2021	<u>Doktorantūros studijos:</u> Gamtos mokslai, Fizika, Vilniaus Universitetas, Fotonikos ir Nanotechnologijų Institutas

Darbo patirtis

Nuo 2016	Inžinierius / vyr. laborantas: Fotonikos ir Nanotechnologijų Institutas
----------	---

LIST OF PUBLICATIONS AND THEIR COPIES

- P1) O. Kravcov, J. Mickevičius, G. Tamulaitis, [*Kinetic Monte Carlo simulations of the dynamics of a coupled system of free and localized carriers in AlGaN*](#), Journal of Physics: Condensed Matter, vol. **32**, no. 14, p. 145901, (2020).
- P2) R. Aleksiejūnas, K. Nomeika, O. Kravcov, S. Nargelas, et al, [*Impact of Alloy-Disorder-Induced Localization on Hole Diffusion in Highly Excited c-Plane and m-Plane \(In, Ga\) N Quantum Wells*](#), Physical Review Applied, vol. **14**, no. 5, pp. 1–11, (2020).
- P3) O. Kravcov, J. Mickevičius, G. Tamulaitis, [*Origin of thermal quenching of exciton photoluminescence in AlGaN epilayers*](#), Lithuanian Journal of Physics, vol. **61**, no. 2, pp. 84–90, (2021).

1st publication

**Kinetic Monte Carlo simulations of the dynamics of a coupled system
of free and localized carriers in AlGaN**

O. Kravcov, J. Mickevičius, G. Tamulaitis

Journal of Physics: Condensed Matter, vol. **32**, no. 14, p. 145901, (2020).

DOI: <https://dx.doi.org/10.1088/1361-648X/ab61cb>

Reprinted with permission from IOP Publishing

PAPER

Kinetic Monte Carlo simulations of the dynamics of a coupled system of free and localized carriers in AlGaN

To cite this article: O Kravcov *et al* 2020 *J. Phys.: Condens. Matter* **32** 145901

View the [article online](#) for updates and enhancements.



IOP | ebooks™

Bringing you innovative digital publishing with leading voices to create your essential collection of books in STEM research.

Start exploring the collection - download the first chapter of every title for free.

Kinetic Monte Carlo simulations of the dynamics of a coupled system of free and localized carriers in AlGaN

O Kravcov[✉], J Mickevičius[✉] and G Tamulaitis

Institute of Photonics and Nanotechnology, Vilnius University, Saulėtekio al. 3, LT-10257, Vilnius, Lithuania

E-mail: kravcovas@gmail.com and juras.mickevicius@ff.vu.lt

Received 20 September 2019, revised 29 November 2019

Accepted for publication 12 December 2019

Published 8 January 2020



Abstract

A model for the dynamics of a coupled system of free and localized carriers in semiconductors with strong carrier localization is suggested. Kinetic Monte Carlo technique is exploited for simulations. The model is verified by fitting the simulated and experimental temperature dependences of photoluminescence (PL) band intensity, peak position, and band width, and the carrier density dependence of PL efficiency in AlGaN quantum wells. The influence of carrier localization conditions on the dominating carrier migration and recombination processes is revealed. The efficiency droop effect is shown to be caused by peculiarities of carrier localization without significant influence of Auger recombination.

Keywords: AlGaN, carrier localization, Monte Carlo simulations, efficiency droop

(Some figures may appear in colour only in the online journal)

1. Introduction

Spatial band gap variations due to inhomogeneities in composition, quantum well (QW) thickness, and strain strongly affect the performance of photonic devices based on ternary and quaternary III-nitride alloys. Localization of the nonequilibrium carriers at the minima of the potential fluctuations can be beneficial for the light emission efficiency: localized carriers are isolated from nonradiative recombination centers (NRCs) [1, 2], and high internal quantum efficiency (IQE) can be achieved despite the large dislocation densities [3, 4]. On the other hand, the carrier localization influences the carrier dynamics even at high densities of nonequilibrium carriers [5–15]. The localization affects the radiative and Auger recombination rates [5, 6]. Delocalization-activated nonradiative recombination and incomplete carrier localization have been suggested as the efficiency droop mechanisms [7–11]. The band potential fluctuation profile has been shown to influence the stimulated emission threshold [12–14]. The carrier localization might also induce current crowding and premature device degradation [15].

Experimentally, the potential fluctuations are evident by a strong inhomogeneous broadening of the photoluminescence (PL) spectra [16]. Additionally, the carrier localization induces unusual temperature dependences of the PL band peak position and width: S-shaped and W-shaped dependences, respectively, have been observed for InGaN [6, 17–19] and AlGaN [7, 12, 14, 16, 20, 21] alloys. The spatial variations of emission intensities and/or peak positions have been studied directly by confocal microscopy [2, 11, 22], scanning near-field optical microscopy (SNOM) [1, 15, 23, 24], and cathodoluminescence (CL) [9, 25]. The potential fluctuations on several spatial scales were revealed with the largest domains of a micron size and the smallest on the scale of a few nm [25–27].

The dynamics of nonequilibrium carriers in the localizing potential is that of the coupled system of the localized and free carriers. However, due to the random nature of the band potential fluctuations, modeling of the carrier dynamics within the localizing potential is a formidable task. Usually, it requires solving the Schrödinger equation for electrons and holes in random localizing potential and determining the energies and

the spatial structure of the localized quantum states. Recently, a method based on localization landscape theory has been proposed, which somewhat reduces the complexity by replacing the Schrödinger equation with a simpler one [28–30].

Simplified approaches to modeling the system consisting of free and localized carriers are typically based on reducing the system to a single dominant constituent of either free or localized carriers at certain conditions. The former are analyzed using the standard ABC model [31–34] with modified recombination rates to allow for the localized carrier migration and recombination [9–11] and/or excitonic recombination [35, 36]. This model relies on the statistical averages describing the thermalized distributions of carriers. Alternatively, for the case of dominant population of localized carriers, Monte Carlo simulations of exciton hopping through a random localizing potential are used [18, 19, 21, 37]. This approach fails at high carrier densities when the contribution of free carriers becomes significant as well as at high temperatures when carriers easily delocalize.

The current study is aimed at developing a method combining both approaches, which is capable of modeling the free and localized carriers simultaneously. Exploiting the kinetic Monte Carlo simulation technique, we were able to describe the temperature- and excitation-dependent behavior of PL band in wide-band-gap AlGaIn QWs structure with strong carrier localization. The simultaneous fit of these dependences has been used as a figure of merit for validation of the model and the parameters used in the model. The simulations enabled us to reveal the importance of certain carrier migration and recombination mechanisms for the dynamics of the coupled system of free and localized carriers in a wide temperature range. In particular, it is shown that the efficiency droop at elevated excitations in AlGaIn QWs used for fitting in this study can be caused by peculiarities of carrier localization without a significant contribution of the Auger processes.

2. Kinetic Monte Carlo simulations

In our model, we consider the following carrier subsystems: free electrons and holes, and exciton-like localized electron–hole pairs. The free carriers can move independently, whereas, the excitons are supposed to behave like single particles that can be trapped by localizing potential [18, 37].

The localized carriers (excitons) can recombine radiatively, hop to another localized state or to the mobility edge (and become delocalized), or tunnel to NRC. The rate of the radiative recombination is calculated as an inverse of the exciton radiative lifetime:

$$\nu_{\text{rad}} = \frac{1}{\tau_{\text{rad}}}. \quad (1)$$

The hopping rate from site i to site j is calculated according to the well-known Miller–Abrahams formula:

$$\nu_{i \rightarrow j} = \nu_0 \exp\left(-\frac{2R_{ij}}{\alpha}\right) \exp\left(-\frac{(E_j - E_i) + |E_j - E_i|}{2k_B T}\right), \quad (2)$$

where E_i and E_j are the energies of the initial and final states, respectively, R_{ij} is the distance between the states in space, α is the decay length of exciton wavefunction, ν_0 is the attempt-to-escape frequency, k_B is the Boltzmann constant, and T is the temperature. The exciton hopping takes place only to an unoccupied localized state.

Carrier delocalization occurs as a transition to mobility edge at the rate:

$$\nu_{\text{deloc}} = \nu_d \exp\left(-\frac{\Delta E}{k_B T}\right). \quad (3)$$

Here, $\Delta E = E_{\text{me}} - E_i$ is the energy difference between mobility edge E_{me} and localized state E_i , and ν_d is the attempt-to-delocalize frequency, which is similar to ν_0 , but includes also the rate of exciton dissociation as well as reflects the probabilities to hop above the mobility edge and relax to it.

The rate of exciton tunneling to NRCs depends on the spatial distribution of both localized states and NRCs, and can be calculated using equation (2) under assumption that the energies of all NRCs serving as the final state E_j are equal. The contribution of all NRCs have to be included:

$$\nu_{\text{nonrad}} = \sum_{\text{NRCs}} \nu_{i \rightarrow \text{NRC}}. \quad (4)$$

The total decay rate of an exciton at a given localized state is calculated as:

$$\nu_i = \nu_{\text{rad}} + \sum_{j \neq i} \nu_{i \rightarrow j} + \nu_{\text{deloc}} + \nu_{\text{nonrad}}. \quad (5)$$

The free carriers are also handled as single particles, but within a large ensemble. Since the carrier thermalization is assumed to be much faster than the recombination and localization processes, the carrier–carrier and carrier–phonon interactions are neglected. The energy distribution of the thermalized ensemble is described by the Fermi–Dirac distribution function $f(E; E_F)$, where E_F is the quasi-Fermi level energy.

The free carriers can move in space, recombine radiatively or nonradiatively, or become localized. Since the spatial distribution of carriers is random, the diffusion processes can be neglected, and the random motion of carriers is simulated as the movement of independent Brownian particles with thermal velocity v_{th} . As the processes of recombination and localized exciton formation require the participation of both electron and hole, we calculate the transition rates for electrons and assume that the required hole emulates the same behavior.

The bimolecular radiative recombination rate for a single electron is calculated as:

$$\nu_{\text{bimol}} = Bp, \quad (6)$$

where p is the free hole concentration, and B is the bimolecular recombination coefficient. The nonradiative recombination rate is expressed using Shockley–Read–Hall model as:

$$\nu_{\text{SRH}} = v_{\text{th}} N_t \sigma_t, \quad (7)$$

where N_t and σ_t are the density and cross-section of NRCs, respectively. The capture of free carriers to the localized state is similar to exciton hopping down to lower energy state, except that only the unoccupied localized states within the

Table 1. Dynamic processes included in the calculations of event rate. The numbers in parentheses indicate the equations used to calculate the corresponding rate.

Localized carriers (excitons)			Free carriers		
Radiative linear recombination	ν_{rad}	(1)	Radiative bimolecular recombination	ν_{bimol}	(6)
Nonradiative recombination	ν_{nonrad}	(4)	Nonradiative recombination	ν_{SRH}	(7)
Delocalization	ν_{deloc}	(3)	Capture to a localized state	ν_{cap}	(8)
Hopping	$\nu_{i \rightarrow j}$	(2)			

radius R_{loc} are considered and both electrons and holes must be present nearby. The capture rate in this case can be calculated as:

$$\nu_{\text{cap}} = \nu_{\text{cap}0} \sum_{j, R_j < R_{\text{loc}}} \exp\left(-\frac{R_j}{R_{\text{loc}}}\right), \quad (8)$$

where $\nu_{\text{cap}0}$ is the capture rate in the limit of carriers being at the same place as the localized state. The total decay rate of a free electron is calculated as:

$$\nu_{\text{free}} = \nu_{\text{bimol}} + \nu_{\text{SRH}} + \nu_{\text{cap}}. \quad (9)$$

The summary of the dynamic processes included in the calculations of carrier decay rates is provided in table 1.

The simulations of carrier dynamics were performed using kinetic Monte Carlo algorithm and following the flow chart shown in figure 1. The detailed simulation procedure is as follows.

- (i) 4D space-energy grid with three spatial dimensions and one energy dimension is created. The grid size is $128 \times 128 \times 5 \times 1000 \text{ nm}^3 \text{ meV}$. The localized states with density N_{loc} and nonradiative recombination centers with density N_{t} are generated randomly within the grid. The energies of the localized states are chosen in such a way that a Gaussian density of localized states is obtained. No correlation between the energies of the localized states and their spatial positions is allowed.
- (ii) Free carriers are generated randomly within the grid. To make the simulations closer to steady-state conditions, the carrier generation is uniformly distributed in time, instead of generating all free carriers at time $t = 0$. For the instantaneous free carrier concentration n_{free} , the quasi-Fermi level E_{F} is calculated using the equation:

$$n_{\text{free}} = \int_0^{\infty} g(E) f(E; E_{\text{F}}) dE, \quad (10)$$

where $g(E)$ is the density of states for the free carriers. Random energy values are assigned to the free carriers according to the Fermi–Dirac distribution $f(E; E_{\text{F}})$.

- (iii) A particle is randomly selected. The rates of all possible transition are calculated, as described above. The probability of any event happening is calculated using the expression:

$$W = 1 - \exp(-\nu \Delta t), \quad (11)$$

where ν is the total decay rate ν_{free} or ν_i for a free carrier or a localized exciton, respectively, and Δt is the time step. A random number taken from a uniform distribution between 0 and 1 determines the event occurrence. If no event occurs, the free carrier moves randomly in space, and the next particle is picked. Otherwise, the type of the process is determined using another random number and the decay rates described by equations (5) and (9) for excitons and free carriers, respectively. After the particle state update, the procedure is repeated to check for the second successive event during the same time step. To reduce the probability of such events, the time step is chosen small enough. If the process of radiative recombination takes place, the spatial coordinates, time moment, and energy of the emitted photon are all recorded.

- (iv) Step (iii) is repeated for all the particles. Afterwards, a new time step begins: a new portion of free carriers is generated, and the procedure is repeated from step (ii), until the final time step value is reached.
- (v) For a new simulation cycle, a new grid with a different random distribution of localized states is generated by starting the procedure from step (i).

The PL spectrum is accumulated by summing the contribution of each radiative recombination event. To obtain each PL spectrum, the simulations were repeated with 10000 different grids. The time step of 1 ps was selected, since it acceptably reduces the probability of a second successive event for a particle during a single time step. The evolution of the system was simulated for 5000 time steps (or 5 ns), which is sufficient to achieve an equilibrium state in a quasi-steady-state excitation regime.

To fit the experimental dependences with the simulation results, the excitation power densities are converted to the carrier generation rates. The fitting range covers 5 orders of magnitude from 1.2×10^{25} to $3.9 \times 10^{30} \text{ cm}^{-3} \text{ s}^{-1}$ in generation rate, corresponding to the calculated carrier density between 2×10^{15} and $2.4 \times 10^{20} \text{ cm}^{-3}$. The essential parameters used in our simulations are $\nu_0 \tau_{\text{rad}}$, $\nu_d \tau_{\text{rad}}$, $\nu_{\text{cap}0} \tau_{\text{rad}}$, $N_{\text{loc}} \alpha^3$, and $N_{\text{t}} \sigma_{\text{t}}$. To estimate the value of $\nu_0 \tau_{\text{rad}}$, we assumed that ν_0 is of the order of 10^{12} s^{-1} [38]. According to the typical experimental results, the exciton lifetime in AlGaIn MQWs was taken to be 200 ps [39], which gives $\nu_0 \tau_{\text{rad}} = 200$. The other parameters were obtained by fitting multiple experimental dependences simultaneously, as described below. The low-temperature bimolecular recombination coefficient B was equal to $4 \times 10^{-10} \text{ cm}^3 \text{ s}^{-1}$ [40], and its dependence on

carrier density due to degeneracy was taken into account as $B = B_0/(1 + n/n^*)$ [31]. Here, B_0 is the low-density coefficient, and n^* is the carrier density at saturation threshold equal to $3 \times 10^{19} \text{ cm}^{-3}$. The values of all the parameters are listed in table 2.

3. Experimental details

To study the dense carrier system containing significant fractions of both localized and free carriers, PL measurements have been carried out on AlGaN/AlGaN multiple quantum wells (MQWs) structure exhibiting strong carrier localization. The AlGaN/AlGaN MQWs were grown by migration-enhanced metalorganic chemical vapor deposition (MEMOCVD[®]) technique on a *c*-plane sapphire substrate. Ten pairs of 5.0 nm thick $\text{Al}_{0.35}\text{Ga}_{0.65}\text{N}$ quantum wells separated by 11.5 nm thick $\text{Al}_{0.49}\text{Ga}_{0.51}\text{N}$ barriers were grown on a 1.2 μm thick *n*- $\text{Al}_{0.55}\text{Ga}_{0.45}\text{N}$ buffer layer.

The PL spectra were measured under excitation power density varied from 0.4 kW cm^{-2} to 14 MW cm^{-2} at different temperatures from 8 K to 300 K. The 4th harmonic (266 nm) of the Q-switched YAG:Nd laser radiation (pulse duration 4 ns) was used for excitation under quasi-steady-state conditions. A closed-cycle helium cryostat ensured the variation and stabilization of temperature. The PL signal was analyzed by a double monochromator (Jobin Yvon HRD-1) and detected by a UV-enhanced photomultiplier.

4. Results and discussion

The simulations of carrier dynamics using the model we developed in this work require many material parameters and several assumptions on the processes of importance. To make the fitting of experimental and simulated results more reliable, we simultaneously fitted two groups of experimentally obtained dependences: (i) temperature dependences of PL efficiency, PL band peak position, and PL band width measured at fixed (low) excitation power density; and (ii) PL efficiency dependences on excitation power density measured at different temperatures. These dependences are commonly used to evaluate various material parameters. The PL efficiency dependence on temperature is usually exploited for the estimation of the IQE under assumption that the efficiency is 100% at low temperatures, even though this assumption is not always true [41]. The S-shaped PL band peak position and W-shaped PL band width dependences indicate carrier localization, and are typically used to quantify the band potential fluctuation profile [6, 7, 12, 14, 16–21]. The PL efficiency dependences on excitation power density generally exhibit efficiency droop, and are used to evaluate the contribution of Auger recombination [31, 33], which is commonly accepted as the main origin of the efficiency droop in InGaN materials [42, 43], and has been suggested to be important also in AlGaN [33]. Nevertheless, the Auger processes have also been shown to be affected by carrier localization [5, 6, 34], while recently, the importance of carrier localization to efficiency droop has reemerged [30, 44, 45]. This situation motivated us for an attempt to simulate

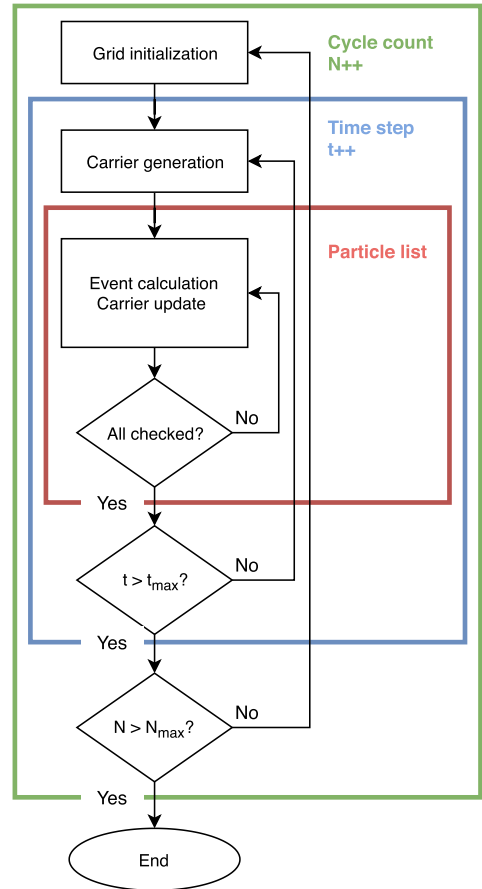


Figure 1. The flow chart of simulation algorithm.

the carrier dynamics in AlGaN by properly describing the influence of carrier localization and without the involvement of the Auger processes.

The starting point in the simulations of PL properties is reproducing the PL spectrum at the conditions corresponding to those in experiment. The PL spectra measured at low temperatures have a Gaussian-like band with strongly expressed LO phonon replicas, as shown in figure 2(a). At elevated temperatures, the phonon replicas become less distinct due to homogeneous thermal broadening (see figure 2(b)). At low excitations, the high-energy slope of the PL band is governed only by the distribution of localized states and exhibits no change with increasing excitation, whereas at high carrier densities, the slope is also affected by the free carrier distribution. Moreover, the increasing excitation results in free carrier heating, which also changes the high-energy slope of the PL band. The typical experimental and simulated PL spectra are illustrated in figure 2 for the temperatures of 8 K and 300 K.

The next step is modeling the temperature dependences of the PL band properties. The experimentally obtained temperature dependence of the spectrally-integrated PL intensity is

Table 2. Values of parameters used in simulations.

Parameter	Value	Parameter	Value	Parameter	Value
τ_{rad}	200 ps	N_{loc}	10^{19} cm^{-3}	σ	30 meV
$\nu_0 \tau_{\text{rad}}$	200	N_i	$3 \times 10^{16} \text{ cm}^{-3}$	Γ	26 meV
$\nu_d \tau_{\text{rad}}$	2000	$N_i \sigma_i$	300 cm^{-1}	$\hbar\omega_{\text{LO}}$	98 meV
$\nu_{\text{cap0}} \tau_{\text{rad}}$	6	B_0	$4 \times 10^{-10} \text{ cm}^3 \text{ s}^{-1}$	β	0.04 meV K^{-1}
$N_{\text{loc}} \alpha^3$	10	n^*	$3 \times 10^{19} \text{ cm}^{-3}$	γ	0.75 eV

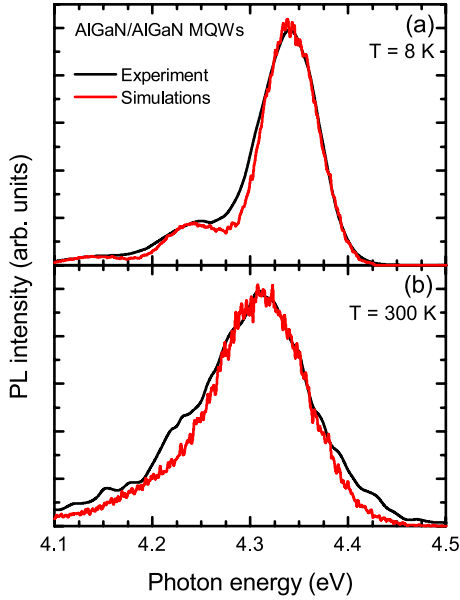


Figure 2. Experimental (black) and simulated (red) PL spectra of AlGaIn MQWs at 8 K (a) and 300 K (b) temperatures.

presented by points in figure 3(a). The PL intensity is almost constant at temperatures below ~40 K and decreases by two orders of magnitude as the temperature is increased up to room temperature. The solid line in figure 3(a) represents the simulated dependence, which fits fairly well. The modeling revealed that the IQE equals ~90% at low temperature and decreases down to less than 1% at room temperature. The PL efficiency decrease with temperature is caused by the increasing fraction of free carriers as well as by an increasing rate of nonradiative recombination.

The temperature dependence of the PL band peak position, shown by filled points in figure 3(b), exhibits nonmonotonous S-shape behavior with three shift regions: initial red shift up to 100 K, followed by a flat region in the range between 100 K and 180 K, and a red shift again at elevated temperatures. Such behavior is typical for ternary III-nitrides and indicates carrier (exciton) redistribution through the localized states [7, 14, 16–21]. At the lowest temperatures, the carriers are frozen at the localized states they occupy after relaxation from excited states, since the thermally-activated redistribution has low probability. Nevertheless, they are still able to hop to adjacent lower-energy states by tunneling. The initial increase in

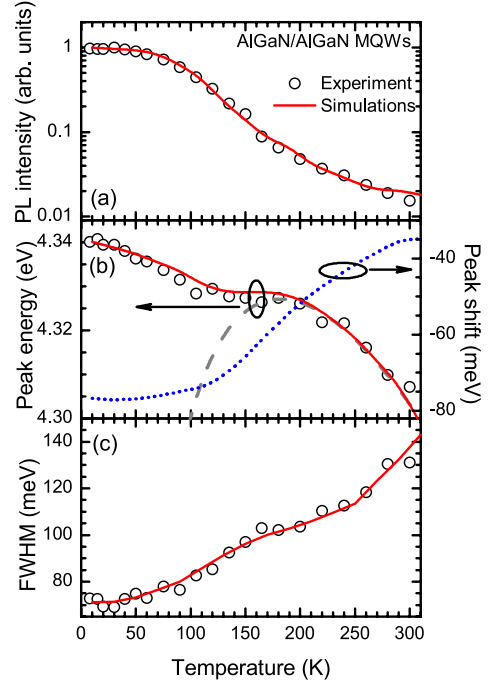


Figure 3. Experimental (points) and simulated (line) PL efficiency (a), band peak position (b), and band width (c) dependences on temperature in AlGaIn MQWs under study. The gray dashed line and the blue dotted line in (b) illustrate, respectively, the peak position calculated using Eliseev formula [17] and the peak position shift with respect to that at 0 K after subtracting the band gap shrinkage (see details in text).

temperature facilitates the carrier redistribution to the lowest available states. The further temperature increase leads to thermalization of the carriers and a blue shift of the band, which results in a more or less pronounced dip in the S-shaped dependence. The PL band red shift at elevated temperatures is caused by the band gap shrinkage.

The high-temperature region of the peak position dependence can be adequately described by the Eliseev formula [17], as shown by the dashed line in figure 3(b), which provides the localization parameter $\sigma = 30 \text{ meV}$ reflecting the energy dispersion of localized states. Meanwhile, subtracting the band gap shrinkage calculated by the Varshni formula [46] with parameters $\alpha = 1.04 \text{ meV K}^{-1}$ and $\beta = 888 \text{ K}$ [47] and plotting the peak position shift with respect to the band gap energy

at 0 K (4.417 eV) reveals that the difference between the PL band and the band gap is constant up to ~100 K temperature. This behavior, shown by open triangles in figure 3(b), indicates that most carriers (excitons) occupy the lowest energy states even at the temperatures as low as 8 K. Moreover, the initial difference of 77 meV is substantially larger than the energy dispersion of localized states (30 meV). Thus, the carriers at low temperatures occupy localized states deep on the tail of the Gaussian distribution. The simulated dependences using these insights and the localization parameter $\sigma = 30$ meV are shown by solid lines in figure 3(b). The fit of simulated results with the experimental data is fairly good in the entire temperature range.

The measured temperature dependence of the PL band width is shown by points in figure 3(c). It exhibits a W-shaped behavior, as is usual for the strong influence of carrier localization [18, 19, 21]. The PL band width varies little below 60 K, increases with temperature until ~160 K, remains constant until ~200 K, and increases again at higher temperatures. The first major increase in PL band width is caused by increasing ability of localized carriers (excitons) to occupy higher energy states. The kink at ~160 K represents a crossover from a non-thermalized to a thermalized energy distribution of the excitons, while the constant band width above the crossover is an indication that a thermalized exciton energy distribution is established. Finally, the second increase in PL band width at elevated temperatures is due to strengthening carrier-phonon interaction [19].

The simulations of PL band width dependence on temperature revealed that the simple localization model, described by a single parameter σ , is insufficient, thus, a more sophisticated double-scaled potential profile model was used. According to this model [18, 19, 21–24], localized carriers (excitons) experience potential fluctuations with the dispersion parameter σ within a certain macroscopically large-scale spatial region. The average exciton energy of such regions fluctuates on another energy scale with dispersion parameter Γ . Under the assumption that the carrier redistribution between the separate large-scale regions is negligible, the dynamics of the PL band peak position is governed mostly by the small-scale potential fluctuations, whereas, the PL band width is a result of the convolution of the distributions reflecting fluctuations on both scales. As shown by the solid line in figure 3(c), the best fit was achieved using the parameters $\sigma = 30$ meV and $\Gamma = 26$ meV. The phonon-assisted band broadening $\Delta\Phi$ has been taken into account as follows [48, 49]:

$$\Delta\Phi(T) = \beta T + \frac{\gamma}{\exp\left(\frac{\hbar\omega_{LO}}{k_B T}\right) - 1}. \quad (12)$$

Here β and γ represent the coupling strength of carriers (excitons) with acoustic and LO phonons, respectively. We use $\hbar\omega_{LO} = 98$ meV, $\beta = 0.04$ meV K⁻¹ and $\gamma = 0.75$ eV obtained from the linear interpolation between the values for GaN and AlN [49].

Finally, the excitation power density dependences of PL efficiency at different temperatures were simulated by taking

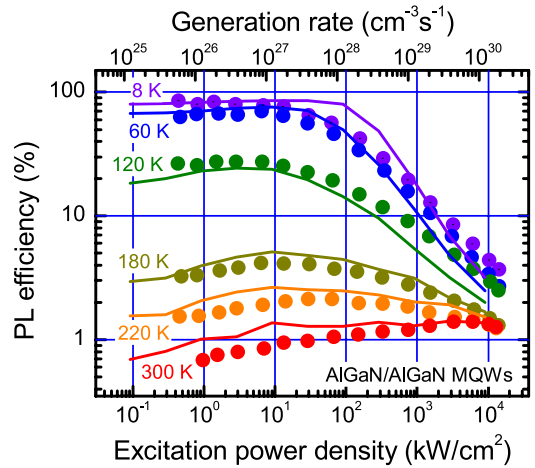


Figure 4. The measured and simulated PL efficiency dependences on excitation power density (points) and carrier generation rate (lines), respectively, at different temperatures (indicated).

into account the localizing potential landscape. The PL efficiency was calculated as the ratio of spectrally-integrated PL intensity and excitation power density. As illustrated by points in figure 4, the experimental dependences have two regions: a small initial increase, and the droop at elevated excitations. The droop onset shifts to lower excitations as the temperature is decreased. The solid lines in figure 4 represent the simulated dependences, which quite adequately follow the experimentally observed behavior for the selected value of localized state density $N_{loc} = 10^{19}$ cm⁻³.

The initial increase of PL efficiency is typically attributed to several effects: the saturation of NRCs, the increasing role of bimolecular radiative recombination due to filling of localized states, and the screening of built-in electric field in QWs [11, 41, 45]. Likewise, the efficiency droop is also assigned to several competing mechanisms with Auger recombination and carrier delocalization being the most important [4, 7–11, 14, 31, 33, 41, 42, 44]. Both for efficiency increase and decrease, the main factor governing the PL efficiency is the ratio between the densities of localized and free carriers: the free carriers recombine radiatively via the more effective bimolecular-type transitions, however, are vulnerable to nonradiative recombination, conversely, the localized carriers are less susceptible to nonradiative recombination, but their radiative recombination is linear. This ratio depends on the localizing potential landscape, and recently, we have proposed a parameter $k_B T / \sigma$, which reflects the ability of localized carriers to delocalize and migrate, and determines the droop mechanism [14, 44]. However, this parameter does not provide details on the contributions of different mechanisms. The simulated excitation and temperature dependences of the ratio between localized and free carrier densities are presented in figure 5. As can be observed, the carriers are mostly localized at temperatures below 100 K, and only at elevated excitations,

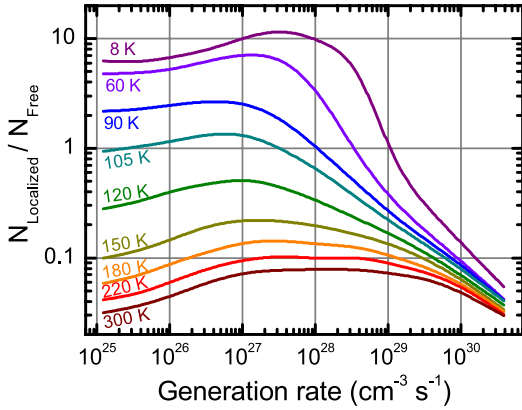


Figure 5. Simulated dependences of the ratio between localized and free carrier densities on generation rate at different temperatures.

once the localized states start saturating, the free carriers become a dominant fraction. Furthermore, at low excitations, the fraction of localized carriers increases with excitation even at temperatures as high as 300 K.

The results of our simulations allowed us to divide the generation rate dependences of the PL efficiency at different temperatures into four areas reflecting the dominance of certain processes in the dynamics of nonequilibrium carriers. Figure 6 presents the division schematically.

In area I, most of the carriers are deeply localized and, as a result, are well isolated from NRCs. The radiative recombination of localized carriers (excitons) controls the PL spectrum and intensity. IQE is high, weakly depends on temperature, and is limited by the ratio between the rates of carrier capture to the localized states and to the NRCs. The density of localized states and radiative lifetime of localized carriers (excitons) determine the range of this area at fixed temperature.

In area II, the efficiency droop emerges due to the nonradiative recombination of localized carriers deteriorating the efficiency. Besides, the fraction of free carriers starts increasing, even though still remaining minor. The onset of area II indicates the ability of excitons to reach NRCs, whereas the slope depends on the NRC density. Nevertheless, the slope remains smaller than that in the area III.

Area III corresponds to the efficiency droop. At elevated excitations, the localized states start saturating, thus, the fraction of free carriers rapidly increases and becomes dominant. However, the free carrier nonradiative recombination dominates over bimolecular recombination, which is still lower than the radiative recombination from localized carriers (excitons).

Area IV is the area exhibiting an increase in efficiency at increasing excitation. Since carrier capture occurs only to those localized states, which have both electron and hole nearby, the increasing carrier density results in the higher

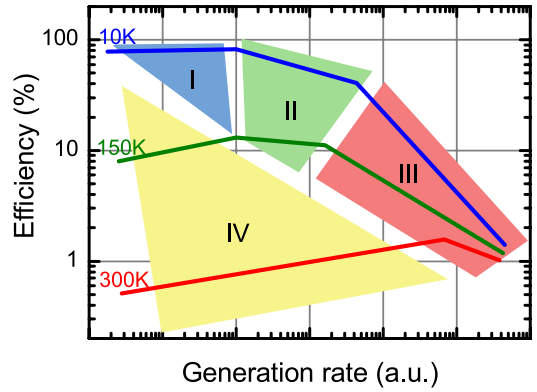


Figure 6. Main regions of the PL efficiency dependences reflecting specific dynamics of nonequilibrium carriers.

probability of carrier localization. As the delocalization rate at fixed temperature is almost constant, it ensues the rising fraction of localized carriers even at 300 K temperature, and causes the efficiency increase.

All the data discussed above imply that the major contribution to photon generation is from localized carriers (excitons) even at room temperature and high generation rate. Despite the considerable increase in free carrier density at elevated excitations, the dominant nonradiative recombination ensures that the role of bimolecular recombination remains smaller than that of the radiative recombination of localized carriers. The PL efficiency dynamics reflects the changes in the relative rates of recombination due to these mechanisms.

5. Conclusions

Kinetic Monte Carlo simulations applied for the system consisting of localized and free carriers enables evaluating the contributions and rates of the main processes determining the efficiency droop, temperature dependence of luminescence efficiency, and the shape of temperature dependences of luminescence band parameters. It has been shown that the efficiency droop in such a system can be interpreted without significant influence of Auger recombination and is mainly determined by peculiarities of carrier localization. The droop effect is attributed to the transition of the system of nonequilibrium carriers from the state with the dominant light emission from strongly localized states with weak nonradiative recombination to the state of predominantly free carriers with a high rate of nonradiative recombination and still a low rate of radiative bimolecular recombination. Excellent agreement between theoretical simulations and experimental data was obtained by employing the developed model for AlGaIn QWs with high density of localized states. The model and simulation procedures are applicable for analysis of carrier dynamics in any materials, where localized and free carriers coexist.

Acknowledgments

The research was funded by European Social Fund (Project No. LMT-K-712-01-0076) under grant agreement with the Research Council of Lithuania (LMTLT).

ORCID iDs

O Kravcov  <https://orcid.org/0000-0001-7148-3335>

J Mickevičius  <https://orcid.org/0000-0003-1623-4138>

References

- [1] Hitzel F, Klewer G, Lahmann S, Rossow U and Hangleiter A 2005 *Phys. Rev. B* **72** 081309
- [2] Kaneta A, Funato M and Kawakami Y 2008 *Phys. Rev. B* **78** 125317
- [3] Chichibu S, Azuhata T, Sota T and Nakamura S 1996 *Appl. Phys. Lett.* **69** 4188
- [4] Shatalov M, Yang J, Sun W, Kennedy R, Gaska R, Liu K, Shur M and Tamulaitis G 2009 *J. Appl. Phys.* **105** 073103
- [5] Jones C M, Teng C-H, Yan Q, Ku P-C and Kioupakis E 2017 *Appl. Phys. Lett.* **111** 113501
- [6] Shahmohammadi M, Liu W, Rossbach G, Lahourcade L, Dussaigne A, Bougerol C, Butte R, Grandjean N, Deveaud B and Jacopin G 2017 *Phys. Rev. B* **95** 125314
- [7] Mickevičius J, Tamulaitis G, Shur M, Shatalov M, Yang J and Gaska R 2013 *Appl. Phys. Lett.* **103** 011906
- [8] Bochkareva N, Rebane Y T and Shreter Y G 2013 *Appl. Phys. Lett.* **103** 191101
- [9] Wang J, Wang L, Wang L, Hao Z, Luo Y, Dempewolf A, Muller M, Bertram F and Christen J 2012 *J. Appl. Phys.* **112** 023107
- [10] Hader J, Moloney J V and Koch S W 2010 *Appl. Phys. Lett.* **96** 221106
- [11] Lin Y, Zhang Y, Liu Z, Su L, Zhang J, Wei T and Chen Z 2014 *J. Appl. Phys.* **115** 023103
- [12] Mickevičius J, Jurkevičius J, Kazlauskas K, Žukauskas A, Tamulaitis G, Shur M S, Shatalov M, Yang J and Gaska R 2012 *Appl. Phys. Lett.* **101** 041912
- [13] Pecora E F, Zhang W, Nikiforov A Yu, Zhou L, Smith D J, Yin J, Paiella R, Dal Negro L and Moustakas T D 2012 *Appl. Phys. Lett.* **100** 061111
- [14] Mickevičius J, Jurkevičius J, Tamulaitis G, Shur M S, Shatalov M, Yang J and Gaska R 2014 *Opt. Express* **22** A491
- [15] Pinos A, Marcinkevičius S, Yang J, Bilenko Y, Shatalov M, Gaska R and Shur M S 2009 *Appl. Phys. Lett.* **95** 181914
- [16] Kuokstis E, Sun W H, Shatalov M, Yang J W and Asif Khan M 2006 *Appl. Phys. Lett.* **88** 261905
- [17] Eliseev P G, Perlin P, Lee J and Osinski M 1997 *Appl. Phys. Lett.* **71** 569
- [18] Kazlauskas K, Tamulaitis G, Pobedinskas P, Žukauskas A, Springis M, Huang C-F, Cheng Y-C and Yang C C 2005 *Phys. Rev. B* **71** 085306
- [19] Ozaki T, Funato M and Kawakami Y 2017 *Phys. Rev. B* **96** 125305
- [20] Bell A, Srinivasan S, Plumlee C, Omiya H, Ponce F A, Christen J, Tanaka S, Fujioka A and Nakagawa Y 2004 *J. Appl. Phys.* **95** 4670
- [21] Kazlauskas K, Žukauskas A, Tamulaitis G, Mickevičius J, Shur M S, Fareed R S Q, Zhang J P and Gaska R 2005 *Appl. Phys. Lett.* **87** 172102
- [22] Mickevičius J, Dobrovolskas D, Aleknavičius J, Grinyš T, Kadys A and Tamulaitis G 2018 *J. Lumin.* **199** 379
- [23] Pinos A, Liuolia V, Marcinkevičius S, Yang J, Gaska R and Shur M S 2011 *J. Appl. Phys.* **109** 113516
- [24] Marcinkevičius S, Jain R, Shatalov M, Yang J, Shur M and Gaska R 2014 *Appl. Phys. Lett.* **105** 241108
- [25] Iwata Y, Oto T, Gachet D, Banal R G, Funato M and Kawakami Y 2015 *J. Appl. Phys.* **117** 115702
- [26] Hahn W et al 2018 *Phys. Rev. B* **98** 045305
- [27] Oliver R A, Bennett S E, Zhu T, Beesley D J, Kappers M J, Saxey D W, Cerezo A and Humphreys C J 2010 *J. Phys. D: Appl. Phys.* **43** 354003
- [28] Filoche M, Piccardo M, Wu Y-R, Li C-K, Weisbuch C and Mayboroda S 2017 *Phys. Rev. B* **95** 144204
- [29] Piccardo M, Li C-K, Wu Y-R, Speck J S, Bonef B, Farrell R M, Filoche M, Martinelli L, Peretti J and Weisbuch C 2017 *Phys. Rev. B* **95** 144205
- [30] Li C-K, Piccardo M, Lu L-S, Mayboroda S, Martinelli L, Peretti J, Speck J S, Weisbuch C, Filoche M and Wu Y-R 2017 *Phys. Rev. B* **95** 144206
- [31] Piprek J 2010 *Phys. Status Solidi a* **207** 2217
- [32] Hopkins M A, Allsopp D W E, Kappers M J, Oliver R A and Humphreys C J 2017 *J. Appl. Phys.* **122** 234505
- [33] Nippert F, Mazraehno M T, Davies M J, Hoffmann M P, Lugauer H-J, Kure T, Kneisl M, Hoffmann A and Wagner M R 2018 *Appl. Phys. Lett.* **113** 071107
- [34] Nippert F, Karpov S Yu, Callsen G, Galler B, Kure T, Nenstiel C, Wagner M R, Strassburg M, Lugauer H-J and Hoffmann A 2016 *Appl. Phys. Lett.* **109** 161103
- [35] Haughn C R, Rupper G, Wunderer T, Yang Z, Johnson N M, Wraback M and Garrett G A 2019 *Appl. Phys. Lett.* **114** 102101
- [36] Langer T, Chernikov A, Kalincev D, Gerhard M, Bremers H, Rossow U, Koch M and Hangleiter A 2013 *Appl. Phys. Lett.* **103** 202106
- [37] Baranovskii S D, Eichmann R and Thomas P 1998 *Phys. Rev. B* **58** 13081
- [38] Baranowski M, Kudriawiec R, Luce A V, Latkowska M, Yu K M, Kuang Y J, Misiewicz J, Tu C W and Walukiewicz W 2015 *J. Appl. Phys.* **117** 175702
- [39] Mickevičius J, Tamulaitis G, Kuokstis E, Liu K, Shur M S, Zhang J P and Gaska R 2007 *Appl. Phys. Lett.* **90** 131907
- [40] Podlipskas Ž, Aleksiejūnas R, Kadys A, Mickevičius J, Jurkevičius J, Tamulaitis G, Shur M, Shatalov M, Yang J and Gaska R 2016 *J. Phys. D: Appl. Phys.* **49** 145110
- [41] Mickevičius J, Tamulaitis G, Shur M, Shatalov M, Yang J and Gaska R 2012 *Appl. Phys. Lett.* **101** 211902
- [42] Iveland J, Martinelli L, Peretti J, Speck J S and Weisbuch C 2013 *Phys. Rev. Lett.* **110** 177406
- [43] Delaney K T, Rinke P and Van de Walle C G 2009 *Appl. Phys. Lett.* **94** 191109
- [44] Mickevičius J, Jurkevičius J, Kadys A, Tamulaitis G, Shur M, Shatalov M, Yang J and Gaska R 2016 *AIP Adv.* **6** 045212
- [45] Gfroerer T H, Chen R, Watt G, Liu Z and Zhang Y 2019 *J. Appl. Phys.* **125** 204502
- [46] Varshni Y P 1967 *Phys. Status Solidi* **19** 459
- [47] Nepal N, Li J, Nakarmi M L, Lin J Y and Jiang H X 2005 *Appl. Phys. Lett.* **87** 242104
- [48] Rudin S, Reinecke T L and Segall B 1990 *Phys. Rev. B* **42** 11218
- [49] Nam K B, Li J, Lin J Y and Jiang H X 2004 *Appl. Phys. Lett.* **85** 3489

2nd publication

Impact of Alloy-Disorder-Induced Localization on Hole Diffusion in Highly Excited c-Plane and m-Plane (In, Ga) N Quantum Wells

Ramūnas Aleksiejūnas, Kazimieras Nomeika, Oleg Kravcov, Saulius Nargelas, Leah Kuritzky, Cheyenne Lynsky, Shuji Nakamura, Claude Weisbuch, James S Speck

Physical Review Applied, vol. **14**, no. 5, pp. 1–11, (2020).
DOI: <https://dx.doi.org/10.1103/PhysRevApplied.14.054043>

Reprinted with permission from American Physical Society


Impact of Alloy-Disorder-Induced Localization on Hole Diffusion in Highly Excited *c*-Plane and *m*-Plane (In,Ga)N Quantum Wells

Ramūnas Aleksiejūnas,¹ Kazimieras Nomeika^{1,*}, Oleg Kravcov¹, Saulius Nargelas,¹ Leah Kuritzky,² Cheyenne Lynsky², Shuji Nakamura,² Claude Weisbuch,^{2,3} and James S. Speck²

¹*Institute of Photonics and Nanotechnology, Vilnius University, Saulėtekio Avenue 3, Vilnius LT-10257, Lithuania*

²*Materials Department, University of California, Santa Barbara, California 93106, USA*

³*Laboratoire de Physique de la Matière Condensée, Ecole Polytechnique, CNRS, IP Paris, Palaiseau Cedex 91128, France*

 (Received 15 June 2020; revised 26 August 2020; accepted 15 October 2020; published 18 November 2020)

The diffusion coefficient of holes can provide knowledge about carrier localization in (In,Ga)N, where the carrier dynamics are altered by randomly fluctuating potential landscape. In group-III nitrides, the diffusivity of holes is difficult to measure by electrical methods but it can be studied using optical techniques. Here, we investigate the dependence of the hole diffusion coefficient on direction and carrier density in *c*-plane and *m*-plane (In,Ga)N structures by employing the light-induced transient-grating technique. We show that the hole diffusion coefficient is anisotropic in the *m*-plane structure, where it is several times larger along the *a* crystallographic direction than along the *c* direction. Such anisotropy is observed within the broad range of carrier densities from 10^{18} to 10^{20} cm⁻³. The diffusivity changes nonmonotonously with increasing photoexcitation, this dependence being different in thick and thin layers. We argue that an unexpectedly high diffusion coefficient at low carrier densities in thick quantum wells can be a signature of efficient hole transport via percolative paths occurring due to compositional disorder. In turn, a decrease of diffusivity with the excitation can reflect the effect of Coulomb blockade of these paths. Finally, we demonstrate that disorder impacts carrier diffusivity even at carrier densities above 10^{19} cm⁻³, where the overflow of localized states must be included to explain the observed increase of the diffusion coefficient with the carrier density.

DOI: [10.1103/PhysRevApplied.14.054043](https://doi.org/10.1103/PhysRevApplied.14.054043)

I. INTRODUCTION

The ternary nitride alloys (In,Ga)N and (Al,Ga)N are currently the materials of choice for light-emitting diodes (LEDs) operating in the visible and ultraviolet spectral range. A key requirement for any LED material is to have a high internal quantum efficiency (IQE), which is an internal material property defined as the ratio of the radiative to the overall recombination rates. Surprisingly, the (In,Ga)N compound is capable of IQE values above 90% despite the extremely high threading dislocation densities, which typically exceed $10^7 - 10^8$ cm⁻² [1,2]. Cathodoluminescence (CL) data have confirmed that threading dislocations indeed act as the nonradiative recombination centers in (In,Ga)N [3,4]. It has been proposed that localization of charge carriers may be the process that hinders carrier transport and, thus, limits nonradiative recombination at dislocations [5].

The presence of carrier localization in (In,Ga)N structures has been demonstrated both experimentally and

theoretically. Localization occurring on a very small scale of 5 nm has been observed directly using scanning tunneling luminescence [6]. Strong hole and weaker electron localization have been proven in several studies, where photoluminescence (PL) and CL measurements have been combined with atomistic calculations [7–12]. Carrier localization is expected to have broad implications that are still being studied and discussed, e.g., a possible link with the “green-gap” problem [13,14], local modification of the recombination constants [15], whether the release of carriers with increasing excitation can contribute to the efficiency droop [16,17], etc.

Solutions to the above-mentioned problems would benefit from better knowledge of localization parameters that, unfortunately, are difficult to measure. Most often, the only known localization parameter is the spectral distribution of the localized states deduced from the “S shape” of the PL peak temperature dependence [18]. On the other hand, it is reasonable to assume for inorganic semiconductors that carriers in the localized states are immobile and that carrier transport occurs via the extended states [19]. Therefore, the transport coefficients must reflect the contribution of

*kazimieras.nomeika@ff.vu.lt

localization when a considerable fraction of the nonequilibrium carriers become trapped in the abundant and deep localized states. In particular, it has been shown that the localization–thermal-release cycle alters the diffusion coefficient of charge carriers [19,20]. Since the holes are strongly localized in (In,Ga)N [8], the hole diffusivity can be a valuable source of information about the localization conditions in a sample. This idea can also be applied beyond nitrides: it has been demonstrated that carrier diffusion in GaAs depends on excitation due to hole trapping by defect states that can be saturated by increasing the carrier density [21,22]. Electrical methods such as Hall measurements rely on the Einstein relation to yield the diffusion coefficient but its applicability is uncertain for highly disordered systems [23,24]. Another option is to use optical methods that measure the ambipolar diffusion coefficient, which, under band-to-band excitation, is governed by hole transport [25].

The ambipolar diffusion coefficient in (In,Ga)N is usually measured using scanning near-field optical microscopy (SNOM) [26], time-of-flight [27], or light-induced transient-grating (LITG) techniques [28]. The former are based on determination of the carrier diffusion length L_D and calculation of the diffusivity D if the carrier lifetime τ is known: $L_D^2 = D\tau$. This approach has been used in several publications to determine the diffusion coefficient in polar (In,Ga)N quantum wells (QWs) [27,29–31]. Also, a modified multimode SNOM setup has been applied to measure the diffusivity in a nonpolar (In,Ga)N QW sample [32]. While allowing for high spatial resolution, the time-of-flight and SNOM-based measurements also have several limitations, such as diffusivity determination from the lifetime-dependent diffusion length and difficult calibration of the photoexcitation. The LITG technique, in contrast, provides a spatially integrated approach and also allows for more accurate calibration of the photoexcited carrier density. The ability of LITG to access very high carrier densities allows studies that are relevant for the IQE droop regime. Furthermore, the technique provides a rather direct measurement of D by separately determining the carrier lifetime and diffusion length. The LITG technique has been used in several publications to study the diffusion coefficient and its dependence on the carrier density and temperature [17,33–35], the authors having concluded that carrier localization indeed affects the ambipolar diffusion coefficient D . However, these studies have also left many unanswered questions, including the possible role of the built-in electrical field or other high-density effects that can influence the diffusivity, such as band degeneracy or electron-hole scattering.

To address these less-investigated aspects of carrier transport in (In,Ga)N quantum structures, we apply the LITG technique to investigate intrawell carrier transport and its dependence on the carrier density and diffusion

direction with respect to the crystallographic axes in polar and nonpolar (In,Ga)N QW structures. To better understand the possible impact of various high-density processes on the value of the ambipolar diffusion coefficient D , we fit the obtained data to a model, which accounts for the carrier localization, degeneracy, and electron-hole scattering. As a result, we are able to confirm that the ambipolar diffusion coefficient is a measure of the hole diffusivity, which is very anisotropic in m -plane samples, and that the hole diffusion is strongly affected by carrier localization even at carrier densities above 10^{18} cm^{-3} . We also show that the dependence of the diffusion coefficient on the carrier density in thick nonpolar QWs is not typical for (In,Ga)N QW structures and we present possible explanations. Finally, we discuss the relevance of the obtained results to LED applications.

II. EXPERIMENT

In this work, we use four different (In,Ga)N structures, all grown by metalorganic chemical vapor deposition. Two samples are deposited on c -plane sapphire substrate, followed by a $3\text{-}\mu\text{m}$ -thick unintentionally doped GaN buffer layer. Onto such a template, we deposit either ten pairs of 3-nm -thick $\text{In}_{0.1}\text{Ga}_{0.9}\text{N}$ QWs— 10 nm GaN barriers in the “ c -MQW” sample or a 58-nm -thick $\text{In}_{0.1}\text{Ga}_{0.9}\text{N}$ single layer in the “thick- c -layer” sample. Both structures are protected by an 8-nm -thick GaN cap layer. The other two m -plane structures have identical structures, except for the QW thickness. They are grown on an m -plane GaN substrate miscut by -1° toward the $[0001]$ direction. On the substrate, a homoepitaxially grown approximately $1.2\text{-}\mu\text{m}$ -thick Si-doped GaN buffer layer is followed by three periods of either 8-nm - (“thick m -plane MQW”) or 4-nm -thick (“thin m -plane MQW”) $\text{In}_{0.13}\text{Ga}_{0.87}\text{N}$ QWs, separated by 9-nm -thick barriers. On top, a 7.5-nm $\text{Al}_{0.22}\text{Ga}_{0.78}\text{N}$ electron blocking layer and a 143-nm p -doped GaN cap layer are deposited.

We employ the LITG technique to measure the ambipolar diffusion coefficient, D_a , and the carrier lifetime, τ , in different directions and at various excitation levels. In the LITG experiment, an interference pattern of two laser beams is used to create a spatially periodic distribution of nonequilibrium carriers in a sample [28]. Figure 1(a) illustrates the basic LITG setup used for this study. The experiment is based on the PHAROS (Light Conversion) laser, which emits 250-fs-duration pulses at a 1030 nm fundamental wavelength at a 30 kHz repetition rate. The laser beam is divided into pump and probe parts. The pump wavelength is tuned to 394 nm using an ORPHEUS (Light Conversion) optical parametric amplifier. The pump wavelength is chosen to photoexcite only the (In,Ga)N QWs but not the GaN layers. To achieve spatially periodic excitation of the sample, we use a holographic beam splitter (HBS) to divide the pump beam into two equal parts (the

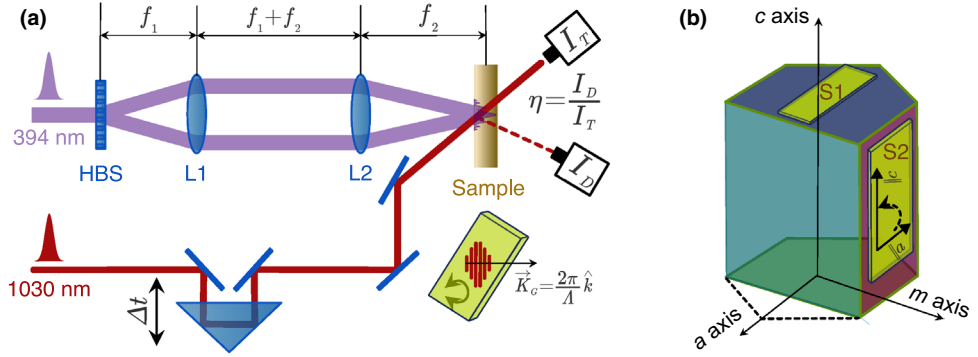


FIG. 1. (a) The light-induced transient-grating (LITG) experimental setup. (b) The orientation of the samples with respect to the crystallographic axes.

beams diffracted into ± 1 orders are used), which are later combined by the lenses L1 and L2 and interfered on the sample surface [36]. The periodic light field photoexcites the nonequilibrium carrier pattern that repeats the periodicity of the photoexcitation, thus recording a transient diffraction grating. The direction of the carrier density gradient is parallel to the transient-grating vector K_g , while the grating period Λ can be varied by using one of the several beam splitters with different periods. We use HBSs with periods of 10, 11.7, 16, and 40 μm , which results in transient diffraction gratings on the sample with periods of $\Lambda = 2.47, 2.91, 4.0,$ and $9.93 \mu\text{m}$, respectively. The exact period of the transient gratings is measured from the phase shift of the diffracted signal [37]. The direction of carrier diffusion with respect to the sample crystallographic orientation is changed by rotating the sample as illustrated in Fig. 1 (b). The photoexcited carrier density N_0 is varied by changing the energy flux (“excitation”) of the pump pulse. At the end of the pulse, N_0 can be estimated as $N_0 = (1 - R)\alpha I_0/h\nu$, where $R = 0.21$ is the reflection coefficient, $\alpha = 1.3 \times 10^5 \text{ cm}^{-1}$ is the (In,Ga)N absorption coefficient at the pump wavelength [34], I_0 is the pump pulse intensity, and $h\nu$ is the pump photon energy. We estimate the photogenerated carrier density by measuring the light absorption in an integrating sphere and find good agreement (within 10%) with the N_0 expression above. The 394-nm excitation wavelength has sufficiently high energy relative to the absorption edge (the band gap) in the (In,Ga)N QWs to avoid absorption bleaching due to the Burstein shift [38] at the lower energies in the QWs [39].

The transient grating is probed by monitoring the diffraction of a probe pulse at 1030 nm, which is arbitrarily delayed with respect to the pump pulse. The diffraction is quantified by the diffraction efficiency η , which is defined as the ratio between the intensities of the diffracted I_D and transmitted I_T parts of the probe beam. Using the classical

Drude theory, $\eta(t)$ can be expressed in the following form [28]:

$$\eta(t) = \left(\frac{\pi dn_{\text{eh}} N(t)}{\lambda} \right)^2 = \left(\frac{\pi dn_{\text{eh}} N_0}{\lambda} \right)^2 \exp\left(-\frac{2t}{\tau_G}\right), \quad (1)$$

where d is the thickness of the photoexcited material, n_{eh} is the refractive index change due to a single electron-hole pair, $N(t)$ is the density of carriers at time t , N_0 is the density of photoexcited carriers at the end of the pump pulse, λ is the wavelength of the probe beam, and τ_G is the time constant of the transient-grating decay.

For light frequencies far from resonance, n_{eh} is equivalent to the following [28]:

$$n_{\text{eh}} = -\frac{e^2}{2n_0 m_r \omega^2 \epsilon_0}, \quad (2)$$

where e is the elementary charge, n_0 is the unperturbed refractive index for the probe wavelength ($\lambda = 1030 \text{ nm}$), $1/m_r = 1/m_e + 1/m_h$ is the reduced electron-hole effective mass (m_e and m_h are the electron and hole effective masses, respectively), ω is the circular frequency of the probe light wave, and ϵ_0 is the permittivity of vacuum.

Note that in Eq. (1) we use the *instantaneous* decay time, τ_G , which describes the decay rate at chosen delay time. Under such an approximation, τ_G can be expressed using the reciprocal summation of the recombination time, τ , and the diffusion-grating decay time, τ_D , [28]:

$$\frac{1}{\tau_G} = \frac{1}{\tau} + \frac{1}{\tau_D} = \frac{1}{\tau} + \frac{4\pi^2 D_a}{\Lambda^2}. \quad (3)$$

Equation (3) indicates that one can extract τ and D_a from the linear fit of the dependence $\tau_G^{-1} = f(\Lambda^{-2})$.

All measurements are carried out at room temperature.

III. RESULTS AND DISCUSSION

We begin with the illustration of D_a and τ determination in the “thick” m -plane sample. Figure 2(a) shows the LITG transients recorded at various grating periods Λ for two different excitations; the shown transients are rather typical. At both excitations, the LITG decay is visibly faster for smaller Λ values, which indicates the measurable impact of diffusion on grating erasure. τ_G is determined from the exponential fit according to Eq. (1) of the initial part of the LITG transient, within approximately 100 ps after the excitation. We assume that this time span is short enough compared to the carrier lifetime so that the photoexcited carrier density N remains close to N_0 . D_a and τ are obtained by fitting Eq. (3) to $1/\tau_G = f(1/\Lambda^2)$, as shown in Fig. 2(b).

In the LITG technique, the carrier density gradient and, thus, the direction of diffusion are parallel to the grating vector. Hence, the anisotropy of the in-plane diffusion can be revealed by rotating a sample, which changes the orientation of the diffusion direction with respect to the crystallographic directions. No changes in D_a values are observed for several random orientations of the c -plane sample, while the D_a value in both m -plane samples is noticeably anisotropic. Figure 3 shows the D_a (a) and τ (b) values as a function of the angle at two excitations in the “thick” m -plane sample; the qualitative picture in the m -MQW structure with thin QWs is similar. The 0° (90°) angle corresponds to the grating vector being parallel to the a (c) direction, as illustrated in Fig. 1(b). We note that pump energy fluences of 90 and $360 \mu\text{J}/\text{cm}^2$ result in photoexcited carrier densities of 1.7×10^{19} and $6.8 \times 10^{19} \text{cm}^{-3}$, respectively. At the lower excitation, D_a changes with the angle from approximately $0.4 \text{cm}^2/\text{s}$ along the c direction to approximately $2.0 \text{cm}^2/\text{s}$ along the a direction. The

anisotropy of the diffusion coefficient is even clearer at the higher excitation of $360 \mu\text{J}/\text{cm}^2$, where D_a increases from approximately $1.3 \text{cm}^2/\text{s}$ to approximately $4.5 \text{cm}^2/\text{s}$. We note that the existence of a small peak at 75° is not certain; most likely it represents measurement error. On the other hand, the carrier lifetime does not depend on the sample orientation and drops from approximately 500 ps to approximately 220 ps with increased excitation [Fig. 3(b)]. These results demonstrate that the electron and hole density distribution is isotropic and that the D anisotropy must be related to the transport anisotropy.

Under the given experimental conditions, where electrons and holes are photoexcited in pairs via interband absorption, the carrier transport is of an ambipolar type. The ambipolar diffusion coefficient obtained in the LITG measurements can be expressed via the monopolar diffusion coefficients using the relation [28]

$$D_a = \frac{n+p}{n/D_h + p/D_e}, \quad (4)$$

where $n(p)$ is the electron (hole) density and D_e (D_h) is the monopolar electron (hole) diffusion coefficient. $n \approx p$ because the photoexcited carrier density exceeds the equilibrium electron density by several orders of magnitude, which in our samples is estimated as lower than 10^{17}cm^{-3} . Also, the inequality $D_e \gg D_h$ holds in group-III nitrides due to the electron mobility being much higher than that of the holes. Under the latter approximations, Eq. (4) leads to $D_a \approx 2D_h$, i.e., the ambipolar diffusion is hole governed. In turn, the monopolar diffusion coefficient in a nondegenerate semiconductor is related to the mobility and the effective mass as $D_h = \mu_h k_B T / e = \tau_{\text{scatt}} k_B T / m_h$, where μ_h is the hole mobility, $k_B T$ is the thermal energy, and τ_{scatt} is the hole-momentum scattering time. The differences in

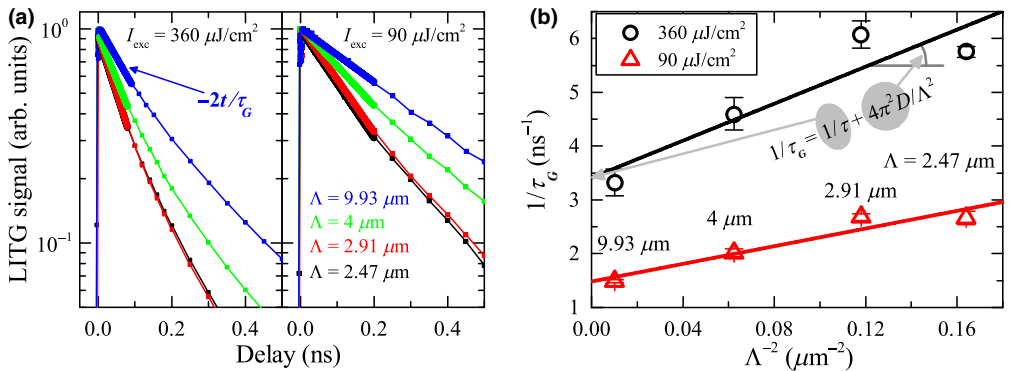


FIG. 2. (a) Normalized LITG transients recorded at four periods Λ (9.93, 4.0, 2.91, and $2.47 \mu\text{m}$) and two excitation energy fluences I_{exc} (90 and $360 \mu\text{J}/\text{cm}^2$, reflection excluded) in the thick m -plane sample. The lines in the initial parts of the transients are exponential fits according to Eq. (1). (b) τ_G^{-1} as a function of Λ^{-2} . The solid lines show the fits according to Eq. (3). The sample is oriented so that carriers diffuse along the a axis.

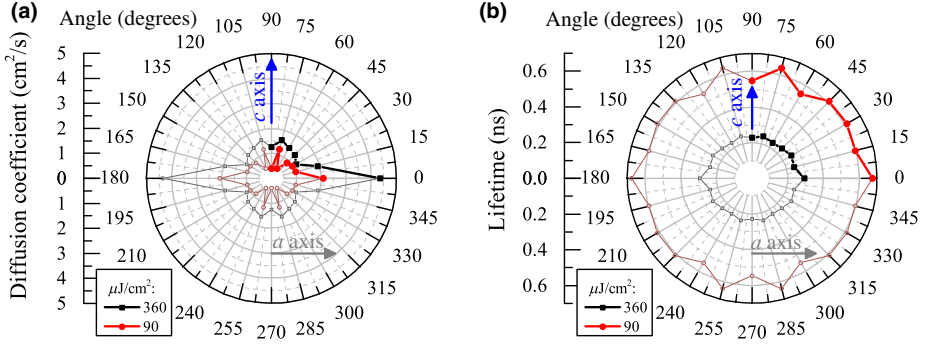


FIG. 3. The measured (a) diffusion coefficient D_a and (b) lifetime τ values as functions of the angle for two excitations of 90 and 360 $\mu\text{J}/\text{cm}^2$ in the “thick” m -plane sample. The data in the first quadrant represent the measured values, while the points in other three quadrants are obtained by symmetrical reflections of the measured values.

the D_a values can be attributed to the anisotropy of the hole effective mass in the m -plane (In,Ga)N. This assumption is in good agreement with the theoretical works by Park *et al.*, who have calculated a hole effective mass of 0.38 m_0 and 1.91 m_0 (m_0 is electron mass) along the a and c directions, respectively, in the m -plane (In,Ga)N, and by Zhao *et al.*, who have attributed the cause of the valence-band anisotropy to unbalanced biaxial stress [40,41]. Our D_a values are also close to those obtained by Mensi *et al.*, in m -plane QWs (0.4 and 1.9 cm^2/s along and perpendicular to the c direction, respectively), where the diffusion anisotropy has also been attributed to the different hole-mass values [32]. Ščajev *et al.* have also observed the anisotropy of the hole diffusion coefficient in bulk m -plane GaN substrates, but the difference in the D_a values along the perpendicular directions has only been found to be 17% [42] (we note that McLaurin *et al.* have found that the hole mobility in bulk m -plane GaN is isotropic [43]). The much smaller anisotropy of the diffusion coefficient in bulk nonpolar GaN, which lacks biaxial strain, agrees well with the explanation for the anisotropy proposed by Zhao *et al.* [41]. We do not, however, exclude the possibility of some contribution by the compositional disorder to anisotropy of the hole diffusion coefficient. As the compositional fluctuations create internal electric fields and potential barriers in nitrides and these fields are strongest along the c direction in the wurtzite structure, one might expect that such barriers will hinder the motion of carriers in the c direction, which is indeed seen in our results. Also, the use of Einstein’s relation between the mobility and the diffusion coefficient might be an approximation in our disordered-alloy system.

Figures 4(a) and 4(b) show the measured diffusion coefficient D_a as a function of the carrier density N in the m -plane and the c -plane samples, respectively. In the

thin c -plane MQW structure (Fig. 4(b), blue triangles), $D_a = 0.7 \text{ cm}^2/\text{s}$ is approximately constant at low densities and starts to increase with excitation above $N = 4 \times 10^{18} \text{ cm}^{-3}$. For the thick c -plane layer as well as the m -plane samples, the diffusion coefficient at low densities behaves differently: it starts from unexpectedly high values (e.g., $D_{\parallel a} = 8 \text{ cm}^2/\text{s}$ and $D_{\parallel c} = 2 \text{ cm}^2/\text{s}$ at $\approx 10^{18} \text{ cm}^{-3}$ in the thick m -plane structure), decreases with the excitation until the minimum value at $N \approx 10^{19} \text{ cm}^{-3}$, and then begins to increase. An extremely high value of $D_a = 25 \text{ cm}^2/\text{s}$ is obtained in the thick c -plane single layer [Fig. 4(b), olive circles]. Let us recall that the low-density D value is $\approx 1 - 2 \text{ cm}^2/\text{s}$ in bulk c -plane GaN [42,44]. We note that in the thick m -plane sample, the ratio between the D_a values along the main orthogonal directions remains approximately constant within the entire density range, which supports the proposition that ambipolar diffusion along those directions is governed by hole transport with different effective masses. On the other hand, $D_a(N)$ at high densities does not seem to depend much on the layer thickness.

While the dependence $D_a(N)$ in the thin c -plane MQW sample resembles those observed in other polar (In,Ga)N QW structures [33,45], the kind of behavior seen in the m -plane and thick c -plane samples is untypical. To better understand the processes behind it, we separately analyze the “low-density” region, where $D(N)$ decreases with increasing density, and the “high-density region,” where the $D(N)$ dependence is opposite and increases with the excitation.

To discuss the low-density region, we begin with the question of why D_a in the m -plane MQWs and the thick c -plane layer is much higher than that in the c -plane MQW sample. No such dependence has been observed in bulk m -plane or c -plane GaN layers [42,44] or in other

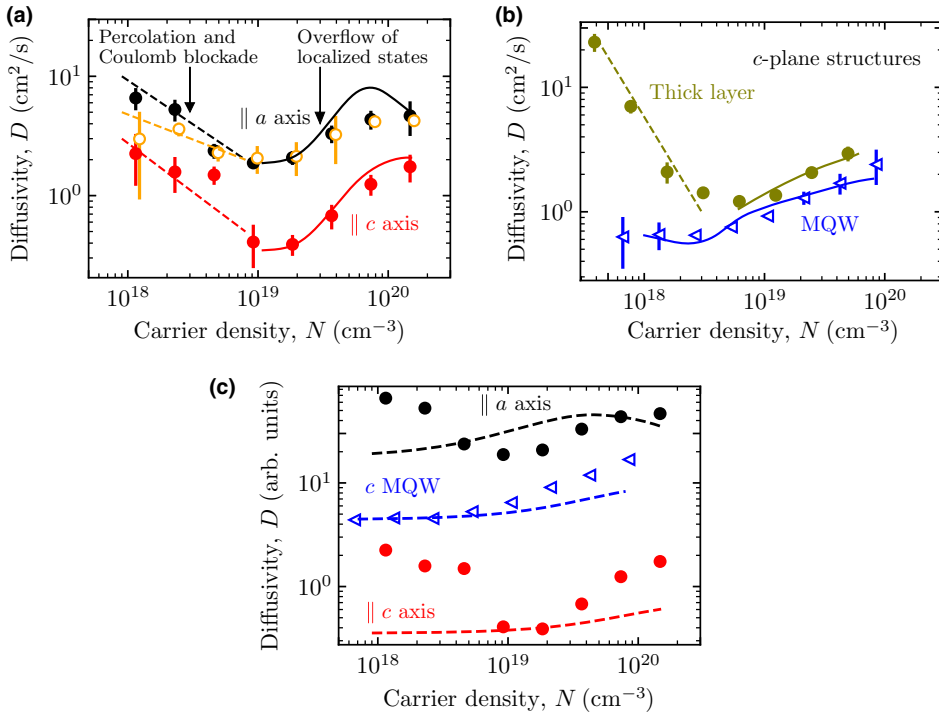


FIG. 4. (a) The measured diffusion coefficient D as a function of the photoexcited carrier density N in the m -plane MQW samples along the $\parallel a$ (black and orange circles for 8-nm and 4-nm wells, respectively) and $\parallel c$ (red circles for 8-nm wells) directions. The dashed lines are guides for the eye to depict the onset of Coulomb blockade along the percolation paths through the localized states. The solid lines show the fits obtained by numerically solving Eqs. (6)–(8). (b) The same $D(N)$ dependences in the thick c -plane layer (olive circles) and the MQW structure (blue triangles). The meaning of the lines is the same as in (a). (c) Fits (dashed lines) of measured $D(N)$ values (symbols), assuming no localization ($N_L = 0$), solving Eqs. (5)–(7). The curves in this figure are arbitrarily shifted with respect to each other for the sake of visibility.

c -plane QW structures [34,45]. These facts suggest that the high diffusivity must be related to the thick layers and compositional disorder.

A possible transport mechanism is due to percolation paths through the disorder-induced localized states, as seen in simulations of MQW LEDs for perpendicular transport. Such simulated percolation paths appear to be at the root of the increased current for a given voltage compared to simulations without disorder [12,46], thereby explaining the diminished turn-on voltage of (In,Ga)N-based LEDs compared to disorderless models. They have also been carefully demonstrated in vertical unipolar transport structures for (In,Ga)N and (Al,Ga)N [47]. Let us remark that bulk or in-plane percolative transport has been observed in bulk semiconductors for a long time, where the disorder is provided by random impurities [48]. In low-dimensional structures, studies of quantum Hall plateaus [49,50] and metal-insulator transitions below the transition threshold [51–53] have also been linked to percolative transport. To

then understand the appearance here of the high diffusion coefficients only for thick layers of (In,Ga)N materials, one should recall the universal increase of percolation with system thickness. The role of QW thickness in increasing percolation from such a compositional disorder has recently been discussed by Horton *et al.* [54]. This idea is well supported by our current results: the increase in D_a is the highest in the c -plane layer, which is the thickest in the sample set, and then this value is smaller in the 8-nm-thick m -plane wells and even smaller in the 4-nm m -plane wells [25, 8, and 2–3 cm^2/s , respectively; see Figs. 4(a) and 4(b)]. Still, these values remain higher than the corresponding D_a value in the even thinner c -plane MQW sample. Therefore, we propose that the high D values at low carrier densities can be explained by efficient hole transport via such percolative paths.

In turn, the decrease of the diffusivity with excitation can occur due to Coulomb blocking in the percolative paths, an effect similar to that in quantum-dot solids, when

occupation of localized states along the percolative paths by carriers hinders the movement of other charge carriers due to the Coulomb interaction between charges [55,56]. A numerical model describing the percolative transport and Coulomb blockade in thick QWs would be challenging, as three-dimensional- (3D) like transport simulations accounting both for compositional disorder and screening of internal electric fields are not yet available. In a simple rule-of-thumb picture, though, one can expect that charging of the localized states occurs at a carrier density N_a such that $a = 1/\sqrt[3]{N_a}$, where a is the size of the localized state. For a typical diameter and separation of 5 nm of the localized states [6,12], the charging is expected to occur at a density of $5 \times 10^{18} \text{ cm}^{-3}$, which is indeed observed in Figs. 4(a) and 4(b). The Coulomb-blockade effect should disappear when the carrier density is such that the Fermi level is above the level of doubly charged localized states—most certainly holes in the present case, as the ambipolar diffusion is dominated by hole transport. This typically occurs at levels of a few tens of millielectronvolts in quantum dots with sizes similar to those of our localized states [55,56], which corresponds to $2 \times 10^{19} \text{ cm}^{-3}$ [38], again in the observed range. Another cause for getting above the Coulomb blockade for diffusion is the filling of states above the depth of the localized states, again a few tens of millielectronvolts [12].

In a more quantitative model, the increase of $D(N)$ with density in the high-density region above 10^{19} cm^{-3} can be explained by hole diffusion in a degenerate semiconductor with disorder; however, without having to take into account the carrier diffusion through the localized states. This is reasonable, as there would be many more delocalized carriers than localized ones. Let us first discuss a model without localization: the increase of the hole diffusion constant in a degenerated case cannot be explained by the degenerate hole gas alone, contrary to what has been shown in bulk GaN [44]. To demonstrate this, we model the dependence $D_E(N)$ for holes using the general Einstein relation, which represents the relation between the diffusivity and mobility of charge carriers in degenerate bands of an ordered semiconductor:

$$D_E(N) = \frac{k_B T}{e} \mu A(\eta) = D_0 A(\eta),$$

$$A(\eta) = \frac{F_{1/2}(\eta)}{F_{-1/2}(\eta)}, \quad \eta = \frac{E - E_F}{k_B T}, \quad (5)$$

where D_0 is the low-density diffusion coefficient without localization and the $F_{\pm 1/2}(\eta)$ are the Fermi integrals of the respective order. We stress that D_0 is considered as a fitting parameter in further discussion, as it is not accessible by experiment. In addition, we include the electron-hole scattering, which becomes important and limits the growth of diffusivity at high carrier densities, especially for a small effective mass [57]. We calculate the corresponding

diffusion coefficient D_{eh} using the modified Fletcher formula, which models the decrease of diffusion coefficient of carriers due to electron-hole collisions in a classical semiconductor when the electron and hole densities are equal ($n \approx p = N$) [58]:

$$D_{\text{eh}}(N) = 48\pi^{3/2} 2^{-3/2} N^{-1} (\epsilon \epsilon_0)^2 e^{-4} \left(\frac{m_e + m_h}{m_e m_h} \right)^{1/2} \times \frac{(k_B T)^{5/2}}{\lg[1 + 256 (\epsilon \epsilon_0)^2 N^{-2/3} e^{-4} k_B^2 T^2]}, \quad (6)$$

where ϵ is the static relative permittivity of the material and ϵ_0 is the permittivity of vacuum. The overall diffusion constant $D(N)$ is given by a sum of reciprocals:

$$\frac{1}{D(N)} = \frac{1}{D_E(N)} + \frac{1}{D_{\text{eh}}(N)}. \quad (7)$$

The dashed lines in Fig. 4(c) show the calculated dependences; D_0 is varied to adjust the calculated curves to the lowest measured D values. The discrepancy with the measured values is obvious for all cases. For a lower effective mass (along the a axis), Eq. (5) almost recreates the rate of $D(N)$ growth with excitation but noticeably underestimates the density at which the increase should start. For higher effective masses (along the c axis), the diffusion coefficient should increase due to hole-gas degeneracy much less than it does in the experiment. This result suggests that another ingredient should be included, namely structural disorder in (In,Ga)N.

To account for the localization effect in the presence of degeneracy, we adopt the relation proposed by Ščajev *et al.*, which calculates the diffusivity D_{loc} [59]:

$$D_{\text{loc}}(N) = \frac{A(\eta) D_0}{1 + A(\eta) \frac{E_U N_L}{k_B T N_C}}, \quad (8)$$

where E_U is the Urbach energy, describing the width of the Gaussian distribution of the localization energy, and N_L and N_C are the densities of the localized and free (mobile) carriers ($N = N_L + N_C$). This model is based on the assumption that carriers in the localized states are immobile and that transport occurs only via extended states, which is reasonable in inorganic semiconductors [19]. In addition, carrier localization is considered a very fast process with a time constant of the order of a picosecond. As a result, such a system can be considered in quasiequilibrium in terms of localized-state occupation on the time scale of hundreds of picoseconds.

The solid lines in Figs. 4(a) and 4(b) show the function $D(N)$ calculated from Eqs. (6)–(8) for effective masses of $0.38 m_0$ (black) and $1.91 m_0$ (red) for the m -plane sample and $1.1 m_0$ (blue) for the c -plane MQW sample, using D_{loc} instead of D_E in Eq. (7). In the modeling, D_0

and $E_U \cdot N_L/N_C$ are fitting parameters, the latter being the density function. The presented fits are obtained assuming the same distribution function but different densities of localized states, the latter being lower by an order of magnitude in the c -plane sample than in the m -plane structure. We believe that this difference in N_L values reflects the different dimensionality of density of states in these samples: the 3D density of states in the thick m -plane sample provides a higher amount of states if compared to the two-dimensional case in the thin c -plane MQW sample. The fits obtained using Eq. (8) follow the diffusion coefficient in the high-density region much more closely, proving that carrier delocalization due to the overflow of localized states plays an important role in diffusivity even at such high densities.

Finally, we discuss the relevance of the presented results to the understanding and optimization of nitride-based LEDs. Experiments coupled with 3D simulations have corroborated that the polarization barriers present in long-wavelength c -plane LEDs limit vertical transport of holes and contribute to the large excess voltage of green LEDs relative to their blue counterparts, resulting in a power-conversion efficiency loss, and are a major contributor to the so-called “green gap” [60]. For long-wavelength c -plane LEDs, it has been demonstrated that these limits to vertical injection can be overcome through the use of inverted hexagonal V defects, where hole injection occurs in parallel into all the QWs of the active LED layer via the V -defect semipolar sidewall [61–63]. LEDs containing engineered V defects currently represent the most promising path to achieving high wall plug efficiency (WPE) long-wavelength devices. However, despite the demonstration of a high WPE at low current using V defects [62,63], the LEDs still exhibit significant current droop, indicating that it is now the in-plane hole transport that hampers complete volumetric injection of multiple QWs. Mitigation of the current droop using V defects and optimized hole-transport structures represents an important opportunity for the advancement of nitride LEDs. Knowledge of hole diffusion in (In,Ga)N alloys and mitigating structures will enable rational heterostructure design through both experimental and 3D simulation methods, such as those carried out by Li *et al.* [64].

For such mitigation studies, in addition to experimental V -defect engineering, the critical in-plane hole diffusion parameters are required as inputs for accurate device simulation. Simulations of LEDs with (In,Ga)N alloy active layers require the incorporation of alloy-disorder effects. Simple one-dimensional simulation tools, therefore not including in-plane compositional fluctuations, lead to excessive onset voltages compared to experiments. Recent 3D simulations including disorder show much improved agreement with experiment and therefore provide an extremely useful tool to further improve LED performance [12,46,60]. However, these modeling tools

require input parameters that are not straightforward to measure by usual techniques. This is particularly true for carrier transport parameters, which require doped materials, whereas the active layers of LEDs are undoped, introducing some variance of measured parameters with those of LED materials, and which, in addition, are typically taken as constant with the carrier density in simulations. Therefore, the presented results obtained by the LITG technique provide valuable information regarding the variation of the diffusion coefficient, and hence the mobility, with the carrier density in undoped material. This situation is commonly encountered when computing I - V characteristics where carrier densities vary by two orders of magnitude in the range of interest. By separating lateral from vertical transport effects, LITG measurements can be used to understand and optimize nitride LEDs.

IV. CONCLUSIONS

We apply the light-induced transient-grating technique to study the hole diffusion in unintentionally doped c -plane and m -plane (In,Ga)N QW structures. The diffusion coefficient in m -plane QWs is anisotropic, up to 5 times higher along the a crystallographic axis if compared to that along the c axis. This difference arises due to anisotropy of the hole effective mass in the topmost valence band. While the diffusion coefficient strongly depends on the carrier density, this dependence differs in thick and thin structures. We suggest that the high diffusivity at low carrier densities in thick structures can be explained by efficient hole transport via percolative paths related to compositional disorder and that a sufficient thickness of layers leads to increased percolative 3D-like transport, i.e., large diffusion coefficients. In turn, the drop of the diffusivity with the carrier density in the range below 10^{19} cm^{-3} can tentatively be attributed to Coulomb blocking of these percolative paths. Alternatively, at carrier densities above 10^{19} cm^{-3} , the growth of the diffusivity with the carrier density could be explained by the cumulative effect of hole-gas degeneracy and overflow of localized states. The obtained understanding of the hole diffusion dependence on carrier density and QW thickness can be useful for LED modeling tools that require transport parameters of undoped (In,Ga)N.

ACKNOWLEDGMENTS

The research at Vilnius University was supported by the Lithuanian Research Council, under Contract No. S-MIP-17-75. The research at the University of California, Santa Barbara was supported by the Solid State Lighting and Energy Electronics Center (SSLEEC), U.S. Department of Energy, under Award No. DE-EE0008204, the National Science Foundation, under Grant No. DMS-1839077, and by grants from the Simons Foundation (Grants No. 601952 to J.S. and No. 601954 to C.W.).

- [1] C. A. Humi, A. David, M. J. Cich, R. I. Aldaz, B. Ellis, K. Huang, A. Tyagi, R. A. Delille, M. D. Craven, F. M. Steranka, and M. R. Krames, Bulk GaN flip-chip violet light-emitting diodes with optimized efficiency for high-power operation, *Appl. Phys. Lett.* **106**, 031101 (2015).
- [2] C. Weisbuch, M. Piccardo, L. Martinelli, J. Iveland, J. Peretti, and J. S. Speck, The efficiency challenge of nitride light-emitting diodes for lighting, *Phys. Status Solidi (A)* **212**, 899 (2015).
- [3] S. J. Rosner, E. C. Carr, M. J. Ludowise, G. Girolami, and H. I. Erikson, Correlation of cathodoluminescence inhomogeneity with microstructural defects in epitaxial GaN grown by metalorganic chemical-vapor deposition, *Appl. Phys. Lett.* **70**, 420 (1997).
- [4] W. Liu, J.-F. Carlin, N. Grandjean, B. Deveaud, and G. Jacopin, Exciton dynamics at a single dislocation in GaN probed by picosecond time-resolved cathodoluminescence, *Appl. Phys. Lett.* **109**, 042101 (2016).
- [5] S. Chichibu, T. Azuhata, T. Sota, and S. Nakamura, Spontaneous emission of localized excitons in InGaN single and multiquantum well structures, *Appl. Phys. Lett.* **69**, 4188 (1996).
- [6] W. Hahn, J.-M. Lentali, P. Polovodov, N. Young, S. Nakamura, J. S. Speck, C. Weisbuch, M. Filoche, Y.-R. Wu, M. Piccardo, F. Maroun, L. Martinelli, Y. Lassailly, and J. Peretti, Evidence of nanoscale Anderson localization induced by intrinsic compositional disorder in InGaN/GaN quantum wells by scanning tunneling luminescence spectroscopy, *Phys. Rev. B* **98**, 045305 (2018).
- [7] C. Humphreys, J. Griffiths, F. Tang, F. Oehler, S. Findlay, C. Zheng, J. Etheridge, T. Martin, P. Bagot, M. Moody, D. Sutherland, P. Dawson, S. Schulz, S. Zhang, W. Fu, T. Zhu, M. Kappers, and R. Oliver, The atomic structure of polar and non-polar InGaN quantum wells and the green gap problem, *Ultramicroscopy* **176**, 93 (2017).
- [8] S. Schulz, M. A. Caro, C. Coughlan, and E. P. O'Reilly, Atomistic analysis of the impact of alloy and well-width fluctuations on the electronic and optical properties of InGaN/GaN quantum wells, *Phys. Rev. B* **91**, 035439 (2015).
- [9] S. Schulz, D. P. Tanner, E. P. O'Reilly, M. A. Caro, T. L. Martin, P. A. J. Bagot, M. P. Moody, F. Tang, J. T. Griffiths, F. Oehler, M. J. Kappers, R. A. Oliver, C. J. Humphreys, D. Sutherland, M. J. Davies, and P. Dawson, Structural, electronic, and optical properties of *m*-plane InGaN/GaN quantum wells: Insights from experiment and atomistic theory, *Phys. Rev. B* **92**, 235419 (2015).
- [10] J. T. Griffiths, S. Schulz, P. Dawson, M. A. Caro, M. J. Davies, C. J. Humphreys, D. S. P. Tanner, R. A. Oliver, E. P. O'Reilly, F. Tang, M. J. Kappers, F. Oehler, and D. Sutherland, Theoretical and experimental analysis of the photoluminescence and photoluminescence excitation spectroscopy spectra of *m*-plane InGaN/GaN quantum wells, *Appl. Phys. Lett.* **109**, 223102 (2016).
- [11] P. Dawson, S. Schulz, R. A. Oliver, M. J. Kappers, and C. J. Humphreys, The nature of carrier localisation in polar and nonpolar InGaN/GaN quantum wells, *J. Appl. Phys.* **119**, 181505 (2016).
- [12] C. K. Li, M. Piccardo, Y. R. Wu, J. S. Speck, B. Bonef, R. M. Farrell, M. Filoche, L. Martinelli, J. Peretti, and C. Weisbuch, Localization landscape theory of disorder in semiconductors. II. Urbach tails of disordered quantum well layers, *Phys. Rev. B* **95**, 144206 (2017).
- [13] S. Y. Karpov, Carrier localization in InGaN by composition fluctuations: Implication to the “green gap”, *Photonics Res.* **5**, A7 (2017).
- [14] D. S. P. Tanner, P. Dawson, M. J. Kappers, R. A. Oliver, and S. Schulz, Polar InGaN/GaN Quantum Wells: Revisiting the Impact of Carrier Localization on the Green Gap Problem, *Phys. Rev. Appl.* **13**, 044068 (2020).
- [15] M. Shahmohammadi, W. Liu, G. Rossbach, L. Lahourcade, A. Dussaigne, C. Bougerol, R. Butté, N. Grandjean, B. Deveaud, and G. Jacopin, Enhancement of Auger recombination induced by carrier localization in InGaN/GaN quantum wells, *Phys. Rev. B* **95**, 125314 (2017).
- [16] C. M. Jones, C. H. Teng, Q. Yan, P. C. Ku, and E. Kioupakis, Impact of carrier localization on recombination in InGaN quantum wells and the efficiency of nitride light-emitting diodes: Insights from theory and numerical simulations, *Appl. Phys. Lett.* **111**, 113501 (2017).
- [17] R. Aleksiejūnas, K. K. Gelžinytė, S. Nargelas, K. Jarašiūnas, M. Vengris, E. A. Armour, D. P. Byrnes, R. A. Arif, S. M. Lee, and G. D. Papanoulis, Diffusion-driven and excitation-dependent recombination rate in blue InGaN/GaN quantum well structures, *Appl. Phys. Lett.* **104**, 022114 (2014).
- [18] Y.-H. Cho, G. H. Gainer, A. J. Fischer, J. J. Song, S. Keller, U. K. Mishra, and S. P. DenBaars, “S-shaped” temperature-dependent emission shift and carrier dynamics in InGaN/GaN multiple quantum wells, *Appl. Phys. Lett.* **73**, 1370 (1998).
- [19] J. Bisquert, Interpretation of electron diffusion coefficient in organic and inorganic semiconductors with broad distributions of states, *Phys. Chem. Chem. Phys.* **10**, 3175 (2008).
- [20] M. Ansari-Rad, J. A. Anta, and J. Bisquert, Interpretation of diffusion and recombination in nanostructured and energy-disordered materials by stochastic quasiequilibrium simulation, *J. Phys. Chem. C* **117**, 16275 (2013).
- [21] T. H. Gfroerer, Y. Zhang, and M. W. Wanlass, An extended defect as a sensor for free carrier diffusion in a semiconductor, *Appl. Phys. Lett.* **102**, 012114 (2013).
- [22] F. Chen, Y. Zhang, T. H. Gfroerer, A. N. Finger, and M. W. Wanlass, Spatial resolution versus data acquisition efficiency in mapping an inhomogeneous system with species diffusion, *Sci. Rep.* **5**, 10542 (2015).
- [23] R. Richert, L. Pautmeier, and H. Bässler, Diffusion and Drift of Charge Carriers in a Random Potential: Deviation from Einstein’s Law, *Phys. Rev. Lett.* **63**, 547 (1989).
- [24] Y. Roichman and N. Tessler, Generalized Einstein relation for disordered semiconductors—Implications for device performance, *Appl. Phys. Lett.* **80**, 1948 (2002).
- [25] R. Aleksiejūnas, M. Sūdzius, T. Malinauskas, J. Vaitkus, K. Jarašiūnas, and S. Sakai, Determination of free carrier bipolar diffusion coefficient and surface recombination velocity of undoped GaN epilayers, *Appl. Phys. Lett.* **83**, 1157 (2003).

- [26] A. Vertikov, I. Ozden, and A. V. Nurmikko, Investigation of excess carrier diffusion in nitride semiconductors with near-field optical microscopy, *Appl. Phys. Lett.* **74**, 850 (1999).
- [27] J. Danhof, U. T. Schwarz, A. Kaneta, and Y. Kawakami, Time-of-flight measurements of charge carrier diffusion in $\text{In}_x\text{Ga}_{1-x}\text{N}/\text{GaN}$ quantum wells, *Phys. Rev. B* **84**, 035324 (2011).
- [28] H. J. Eichler, P. Gunter, and D. W. Pohl, *Laser-Induced Dynamic Gratings* (Springer-Verlag, New York, 1986).
- [29] A. Vertikov, I. Ozden, and A. V. Nurmikko, Diffusion and relaxation of excess carriers in InGaN quantum wells in localized versus extended states, *J. Appl. Phys.* **86**, 4697 (1999).
- [30] A. Kaneta, T. Hashimoto, K. Nishimura, M. Funato, and Y. Kawakami, Visualization of the local carrier dynamics in an InGaN quantum well using dual-probe scanning near-field optical microscopy, *Appl. Phys. Express* **3**, 102102 (2010).
- [31] H.-M. Solowan, J. Danhof, and U. T. Schwarz, Direct observation of charge carrier diffusion and localization in an InGaN multi quantum well, *Jpn. J. Appl. Phys.* **52**, 08JK07 (2013).
- [32] M. Mensi, R. Ivanov, T. K. Uždavinyš, K. M. Kelchner, S. Nakamura, S. P. DenBaars, J. S. Speck, and S. Marcinkevičius, Direct measurement of nanoscale lateral carrier diffusion: Toward scanning diffusion microscopy, *Acs Photonics* **5**, 528 (2017).
- [33] R. Aleksiejūnas, P. Ščajev, S. Nargelas, T. Malinauskas, A. Kadys, and K. Jarašiūnas, Impact of diffusivity to carrier recombination rate in nitride semiconductors: From bulk GaN to (In, Ga) N quantum wells, *Jpn. J. Appl. Phys.* **52**, 08JK01 (2013).
- [34] K. Nomeika, R. Aleksiejūnas, S. Miasojedovas, R. Tomašiūnas, K. Jarašiūnas, I. Pietzonka, M. Strassburg, and H. J. Lugauer, Impact of carrier localization and diffusion on photoluminescence in highly excited cyan and green InGaN LED structures, *J. Lumin.* **188**, 301 (2017).
- [35] Z. Ye, H. Nguyen, S.-W. Feng, H.-C. Wang, and H.-L. Chou, Carrier dynamics in InGaN/GaN on the basis of different In concentrations, *Appl. Sci.* **9**, 2279 (2019).
- [36] K. Jarašiūnas, R. Aleksiejūnas, T. Malinauskas, V. Gudelis, T. Tamulevičius, S. Tamulevičius, A. Guobienė, A. Usikov, V. Dmitriev, and H. J. Gerritsen, Implementation of diffractive optical element in four-wave mixing scheme for *ex situ* characterization of hydride vapor phase epitaxy-grown GaN layers, *Rev. Sci. Instrum.* **78**, 033901 (2007).
- [37] T. Malinauskas, S. Nargelas, R. Aleksiejūnas, and K. Jarašiūnas, Heterodyne detection scheme for light-induced transient grating experiment, *Opt. Commun.* **281**, 6061 (2008).
- [38] M. Feneberg, S. Osterburg, K. Lange, C. Lidig, B. Garke, R. Goldhahn, E. Richter, C. Netzel, M. D. Neumann, N. Esser, S. Fritze, H. Witte, J. Bläsing, A. Dadgar, and A. Krost, Band gap renormalization and Burstein-Moss effect in silicon- and germanium-doped wurtzite GaN up to 10^{20} cm^{-3} , *Phys. Rev. B* **90**, 075203 (2014).
- [39] C. Shank, R. Fork, R. Yen, J. Shah, B. Greene, A. Gossard, and C. Weisbuch, Picosecond dynamics of hot carrier relaxation in highly excited multi-quantum well structures, *Solid State Commun.* **47**, 981 (1983).
- [40] S. H. Park, D. Ahn, and S. L. Chuang, Electronic and optical properties of *a*- and *c*-plane wurtzite InGaN-GaN quantum wells, *IEEE J. Quantum Electron.* **43**, 1175 (2007).
- [41] Y. Zhao, R. M. Farrell, Y.-R. Wu, and J. S. Speck, Valence band states and polarized optical emission from nonpolar and semipolar III-nitride quantum well optoelectronic devices, *Jpn. J. Appl. Phys.* **53**, 100206 (2014).
- [42] P. Ščajev, K. Jarašiūnas, Ü. Özgür, H. Morkoç, J. Leach, and T. Paskova, Anisotropy of free-carrier absorption and diffusivity in *c*-plane GaN, *Appl. Phys. Lett.* **100**, 022112 (2012).
- [43] M. McLaurin and J. S. Speck, *p*-type conduction in stacking-fault-free *m*-plane GaN, *Phys. Status Solidi (RRL)—Rapid Res. Lett.* **1**, 110 (2007).
- [44] T. Malinauskas, K. Jarašiūnas, M. Heuken, F. Scholz, and P. Brückner, Diffusion and recombination of degenerate carrier plasma in GaN, *Phys. Status Solidi (C)* **6**, S743 (2009).
- [45] R. Aleksiejūnas, K. Nomeika, S. Miasojedovas, S. Nargelas, T. Malinauskas, K. Jarašiūnas, Ö. Tuna, and M. Heuken, Carrier dynamics in blue and green emitting InGaN MQWs, *Phys. Status Solidi (B)* **252**, 977 (2015).
- [46] T.-J. Yang, R. Shivaraman, J. S. Speck, and Y.-R. Wu, The influence of random indium alloy fluctuations in indium gallium nitride quantum wells on the device behavior, *J. Appl. Phys.* **116**, 113104 (2014).
- [47] D. A. Browne, M. N. Fireman, B. Mazumder, L. Y. Kuritzky, Y.-R. Wu, and J. S. Speck, Vertical transport through AlGaIn barriers in heterostructures grown by ammonia molecular beam epitaxy and metalorganic chemical vapor deposition, *Semicond. Sci. Technol.* **32**, 025010 (2017).
- [48] B. I. Shklovskii and A. L. Efros, *Electronic Properties of Doped Semiconductors*, Springer Series in Solid-State Sciences (Springer-Verlag, Berlin, 1984).
- [49] R. F. Kazarinov and S. Luryi, Quantum percolation and quantization of Hall resistance in two-dimensional electron gas, *Phys. Rev. B* **25**, 7626 (1982).
- [50] D.-H. Lee, Z. Wang, and S. Kivelson, Quantum Percolation and Plateau Transitions in the Quantum Hall Effect, *Phys. Rev. Lett.* **70**, 4130 (1993).
- [51] L. A. Tracy, E. H. Hwang, K. Eng, G. A. Ten Eyck, E. P. Nordberg, K. Childs, M. S. Carroll, M. P. Lilly, and S. Das Sarma, Observation of percolation-induced two-dimensional metal-insulator transition in a Si MOSFET, *Phys. Rev. B* **79**, 235307 (2009).
- [52] J.-S. Kim, A. M. Tyryshkin, and S. A. Lyon, Annealing shallow Si/SiO₂ interface traps in electron-beam irradiated high-mobility metal-oxide-silicon transistors, *Appl. Phys. Lett.* **110**, 123505 (2017).
- [53] A. Sammak, D. Sabbagh, N. W. Hendrickx, M. Lodari, B. P. Wuetz, A. Tosato, L. Yeoh, M. Bollani, M. Virgilio, M. A. Schubert, P. Zaumseil, G. Capellini, M. Veldhorst, and G. Scappucci, Shallow and undoped germanium quantum wells: A playground for spin and hybrid quantum technology, *Adv. Funct. Mater.* **29**, 1807613 (2019).
- [54] M. K. Horton and M. A. Moram, Alloy composition fluctuations and percolation in semiconductor alloy quantum wells, *Appl. Phys. Lett.* **110**, 162103 (2017).

- [55] H. E. Romero and M. Drndić, Coulomb Blockade and Hopping Conduction in PbSe Quantum Dots, *Phys. Rev. Lett.* **95**, 156801 (2005).
- [56] R. E. Chandler, A. J. Houtepen, J. Nelson, and D. Vanmaekelbergh, Electron transport in quantum dot solids: Monte Carlo simulations of the effects of shell filling, Coulomb repulsions, and site disorder, *Phys. Rev. B* **75**, 085325 (2007).
- [57] N. H. Fletcher, The high current limit for semiconductor junction devices, *Proc. IRE* **45**, 862 (1957).
- [58] A. H. Hill, K. E. Smyser, C. L. Kennedy, E. S. Mas-saro, and E. M. Grumstrup, Screened charge carrier transport in methylammonium lead iodide perovskite thin films, *J. Phys. Chem. Lett.* **8**, 948 (2017).
- [59] P. Ščajev, C. Qin, R. Aleksiejūnas, P. Baronas, S. Miasojedovas, T. Fujihara, T. Matsushima, C. Adachi, and S. Juršėnas, Diffusion enhancement in highly excited MAPbI₃ perovskite layers with additives, *J. Phys. Chem. Lett.* **9**, 3167 (2018).
- [60] C. Lynsky, A. I. Alhassan, G. Lheureux, B. Bonef, S. P. DenBaars, S. Nakamura, Y.-R. Wu, C. Weisbuch, and J. S. Speck, Barriers to carrier transport in multiple quantum well nitride-based *c*-plane green light emitting diodes, *Phys. Rev. Mater.* **4**, 054604 (2020).
- [61] Z. Quan, L. Wang, C. Zheng, J. Liu, and F. Jiang, Roles of *V*-shaped pits on the improvement of quantum efficiency in InGaN/GaN multiple quantum well light-emitting diodes, *J. Appl. Phys.* **116**, 183107 (2014).
- [62] F. Jiang, J. Zhang, L. Xu, J. Ding, G. Wang, X. Wu, X. Wang, C. Mo, Z. Quan, X. Guo, C. Zheng, S. Pan, and J. Liu, Efficient InGaN-based yellow-light-emitting diodes, *Photonics Res.* **7**, 144 (2019).
- [63] S. Zhang, J. Zhang, J. Gao, X. Wang, C. Zheng, M. Zhang, X. Wu, L. Xu, J. Ding, Z. Quan, *et al.*, Efficient emission of InGaN-based light-emitting diodes: Toward orange and red, *Photonics Res.* **8**, 1671 (2020).
- [64] C.-K. Li, C.-K. Wu, C.-C. Hsu, L.-S. Lu, H. Li, T.-C. Lu, and Y.-R. Wu, 3D numerical modeling of the carrier transport and radiative efficiency for InGaN/GaN light emitting diodes with V-shaped pits, *AIP Adv.* **6**, 055208 (2016).

3rd publication

Origin of thermal quenching of exciton photoluminescence in AlGaN epilayers

O. Kravcov, J. Mickevičius, G. Tamulaitis

Lithuanian Journal of Physic, vol. **61**, no. 2, pp. 84–90, (2021).

DOI: <https://dx.doi.org/10.3952/physics.v61i2.4437>

Reprinted with permission from Lithuanian Academy of Sciences

ORIGIN OF THERMAL QUENCHING OF EXCITON PHOTOLUMINESCENCE IN AlGaN EPILAYERS

O. Kravcov, J. Mickevičius, and G. Tamulaitis

Institute of Photonics and Nanotechnology, Vilnius University, Saulėtekio 3, 10257 Vilnius, Lithuania

Email: kravcovas@gmail.com; juras.mickevicius@ff.vu.lt

Received 11 May 2021; accepted 13 May 2021

The dynamics of a low-density exciton system is simulated using the kinetic Monte Carlo algorithm. The temperature dependences of photoluminescence (PL) intensity and PL band Stokes shift in a high-Al-content AlGaN epilayer are calculated and fitted to the experimentally measured ones. The key features of nonradiative recombination via delocalized states and direct tunnelling to nonradiative recombination centres and its influence on PL efficiency are analysed. A strong influence of the tunnelling-based recombination in AlGaN epilayers with a large ratio between the densities of nonradiative recombination centres and localized states is revealed.

Keywords: III-nitrides, carrier localization, Monte Carlo simulations, exciton hopping, nonradiative recombination

PACS: 78.55.-m, 78.20.Bh, 73.50.Gr

1. Introduction

The quantum efficiency of photoluminescence (PL) in semiconductor materials and their heterostructures decreases with increasing temperature. Regardless of the specific quenching mechanism, the temperature dependence of the spectrally-integrated PL intensity is usually described by the expression

$$I(T) = \frac{I_0}{1 + \sum_i c_i \exp\left(-\frac{E_{Ai}}{k_B T}\right)}, \quad (1)$$

where I_0 is the low-temperature PL intensity, c_i and E_{Ai} are the rate constant and activation energy of the i th process, and i is the number of nonradiative recombination channels, typically ranging from 1 to 3 [1–9]. The thermally-activated mechanisms responsible for the PL quenching are usually related to the thermal dissociation of free or bound excitons [1–3], escape of carriers out of a quantum well [3, 4], transfer of carriers over a barrier to nonradiative recombination centres [5, 6], and thermal activation of localized carriers [4, 6–9].

The mechanism of carrier delocalization is commonly used to interpret the PL temperature dynamics in materials having a large density of localized states, e.g. ternary nitride alloys, InGaN [6, 7] and AlGaN [8, 9]. However, a few distinct activation energies are hardly compatible with a wide and continuous energy distribution of localized states. An alternative approach is based on the concepts of carrier transport in disordered semiconductors [10, 11]. Such approach takes into account not only the interplay between radiative and nonradiative processes, but also the dynamic exchange of carriers between localized states. The temperature dependence of PL intensity in disordered semiconductors has been shown to be determined both by carrier localization energy scale and the relative concentration of nonradiative centres [11, 12]. However, while the main mechanism of nonradiative recombination is linked to the carrier delocalization, an alternative channel of direct tunnelling to nonradiative centres is usually neglected [13].

In the current paper, we combined both approaches to analyse the thermal quenching of PL intensity in AlGaN epilayers. Exploiting Monte

Carlo simulations to reproduce the PL characteristics and their dependence on temperature, and introducing different recombination mechanisms step-by-step into the model enabled us to reveal the influence and importance of these mechanisms for exciton dynamics and PL properties in the temperature range from 8 to 300 K. We show that the mechanism of exciton tunnelling to nonradiative centres cannot be neglected at high relative densities of nonradiative centres. Moreover, this mechanism has a strong impact on PL intensity already at the lowest temperatures.

2. Experiment

A single AlGa_N epilayer distinguished by strong carrier localization was selected for the study. The Al_{0.65}Ga_{0.35}N epilayer was grown by migration-enhanced metalorganic chemical vapour deposition (MEMOCVD[®]) on the c-plane sapphire substrate. The photoluminescence was measured under quasi-steady-state excitation conditions. The 5th harmonic (213 nm) of the Q-switched YAG:Nd laser radiation (pulse duration 4 ns) was used for excitation. A closed-cycle helium cryostat enabled the variation of temperature in the range from 8 to 300 K. The PL signal was analysed by a double monochromator (*Jobin Yvon* HRD-1) and detected by a UV-enhanced photomultiplier.

3. Theoretical model and Monte Carlo simulation procedures

The model of carrier dynamics that we use for our simulations of PL properties is based on the modified exciton hopping model [11, 14, 15]. In this model, electrons and holes generated by optical excitation rapidly form strongly correlated pairs of excitons, which behave like single non-interacting particles that can be trapped by localizing potential. Localized excitons can recombine radiatively, hop to another localized state or to the mobility edge and become delocalized, or tunnel to a nonradiative recombination centre (NRC). Delocalized (free) excitons can be captured by either a localized state or a NRC. The radiative recombination of free excitons is assumed much slower than the capture processes and is, therefore, neglected. All the kinetic processes considered in the model are schematically illustrated in Fig. 1(a). The rates (prob-

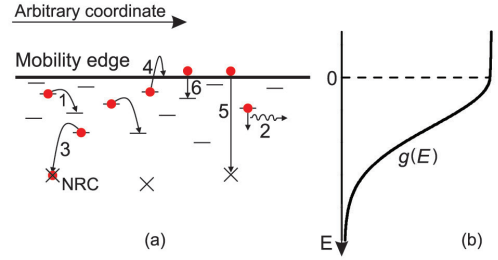


Fig. 1. (a) A schematic illustration of the processes involved in the model of exciton dynamics: hopping transitions between localized states (1), radiative recombination (2), tunnelling to NRC (3), delocalization to the mobility edge (4), capture to NRC (5) and capture to localized state (6). (b) Schematic energy distribution of localized states in the band tail. The origin of energy axes is set to the mobility edge.

abilities) of different processes are described by formulae presented below.

The localized excitons can move through the localized states at the rate of hopping from site i to site j calculated using the well-known Miller–Abrahams formula

$$v_{i \rightarrow j} = v_0 \exp\left(-\frac{2R_{ij}}{\alpha}\right) \exp\left(-\frac{E_j - E_i + |E_j - E_i|}{2k_B T}\right), \quad (2)$$

where E_i and E_j are the energies of the initial and final states, respectively, R_{ij} is the distance between the states in real space, α is the decay length of exciton wavefunction, and v_0 is the attempt-to-escape frequency.

The radiative recombination rate equals the inverse of exciton lifetime,

$$v_{\text{rad}} = \tau_0^{-1}. \quad (3)$$

The rate of nonradiative recombination of localized excitons is determined by the probability of tunnelling to NRCs, that depends on the spatial distributions of both NRCs and localized states. Using Eq. (2) and assuming that deep levels act as NRCs, the rate of exciton tunnelling to NRC is described as

$$v_{\text{tunnel}} = v_0 \exp\left(-\frac{2R_{i,\text{NRC}}}{\alpha}\right), \quad (4)$$

where $R_{i,\text{NRC}}$ is the distance from the localized state to NRC.

The carrier delocalization is considered as a vertical transition in energy space to the mobility edge at the rate

$$v_{\text{deloc}} = v_0 \exp\left(-\frac{\Delta E}{k_B T}\right), \quad (5)$$

determined by $\Delta E = E_{\text{me}} - E_i$, the energy difference between the mobility edge E_{me} and localized state E_i .

A free exciton can be captured to any localized state at the rate

$$v_{\text{capr}} = v_0 \frac{N_{\text{loc}}}{N}, \quad (6)$$

whereas the rate for the capture of free excitons by NRCs is described by a similar expression

$$v_{\text{capnr}} = v_0 \frac{N_{\text{NRC}}}{N}. \quad (7)$$

Here $N = N_{\text{loc}} + N_{\text{NRC}}$ is the total density of localized states and NRCs.

The simulations have been performed using the kinetic Monte Carlo algorithm. The simulation procedure starts by creating a 4D space-energy grid with three spatial and one energy dimensions. The localized states and nonradiative recombination centres with densities N_{loc} and N_{NRC} , respectively, are randomly generated within the grid. The energy distribution of the localized states $g(E)$ is assumed to be Gaussian

$$g(E) = \frac{N_{\text{loc}}}{\sqrt{2\pi}\sigma^2} \exp\left(-\frac{(E - E_{\text{me}})^2}{2\sigma^2}\right), \quad (8)$$

with the energy scale defined as the standard deviation for the potential fluctuations σ [16, 17]. No correlation between the energies of the localized states and their spatial positions is allowed.

Next, a single exciton is generated randomly within the grid. The rates of all possible transitions are calculated using Eqs. (2–8), as described above, and the process is selected randomly. This procedure is repeated until the exciton recombines. For a given distribution of localized states and NRCs, the simulations are repeated many times in order to obtain reliable results. The PL spectrum is accumulated by summing the contribution of each radiative recombination event. Since experimentally obtained PL spectra are typically collected from

the area much larger than the simulation grid, the simulations are repeated for a large number of different random distributions of localized states.

4. Results and discussion

The simulations of exciton dynamics and, consequently, of PL properties has been performed by stepwise introduction of different processes into the model describing exciton dynamics. This approach enabled us to reveal the importance of the processes, study the influence of the parameters defining the rate of the processes and link the parameters with the material properties.

At low excitations, the radiative recombination of localized excitons is the dominant radiative process. The PL band shape is generally determined by the distribution function of localized states and parameters $v_0\tau_0$ and $N\alpha^3$, which govern the localized exciton hopping process in time and space, respectively [14, 15]. Meanwhile, the PL intensity (and efficiency) is governed by the ratio $N_{\text{NRC}}/N_{\text{loc}}$, which controls the influence of nonradiative recombination [11, 15].

To evaluate the energy scale of the distribution of localized states as well as estimate the values of exciton hopping parameters $v_0\tau_0$ and $N\alpha^3$, we exploited the temperature dependence of the Stokes shift (defined as the difference between the PL band peak position and the mobility edge) shown in Fig. 2. The measured PL Stokes shift slightly

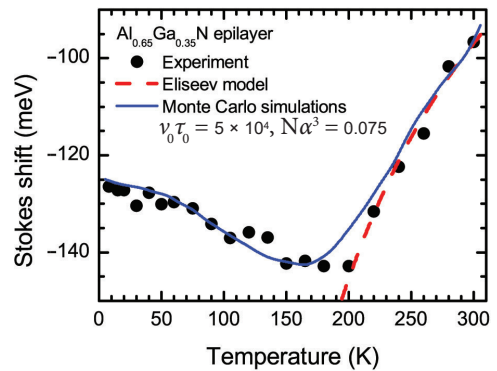


Fig. 2. The temperature dependence of Stokes shift in the AlGa_{0.35}N epilayer with Al content of 65%. Lines show the fits using the Eliseev model (dashed line, red online) and Monte Carlo simulations (solid line, blue online).

increases with increasing temperature approximately in the range from 8 to 200 K and decreases at elevated temperatures up to 300 K. A simple quantitative model of band tail filling, also referred to as Eliseev model [16], reproduces the Stokes shift decrease at elevated temperatures, as indicated by a red (online) dashed line in Fig. 2. The application of the Eliseev model in this temperature range enables estimation of the dispersion parameter describing the energy distribution of localized states ($\sigma = 50$ meV for the $\text{Al}_{0.65}\text{Ga}_{0.35}\text{N}$ epilayer presented in Fig. 2). Meanwhile, the increase of the Stokes shift as well as its low-temperature value was successfully simulated using an exciton hopping model, and allowed estimating the hopping parameters $\nu_0 \tau_0 = 5 \times 10^4$ and $N\alpha^3 = 0.075$. The simulated Stokes shift dependence is presented by a blue (online) solid line in Fig. 2, and a good agreement with the experimental points is achieved.

The determination of simulation parameters that influence the radiative recombination enabled us to simulate the temperature dependence of PL intensity, which is strongly affected by the nonradiative recombination. The temperature dependence of PL intensity measured under quasi-steady-state excitation is presented in Fig. 3. In the selected high-Al-content epilayer, the PL intensity decreases, albeit slowly, already at low temperatures. The decrease becomes substantially faster at elevated temperatures. The experimental points might be well fitted

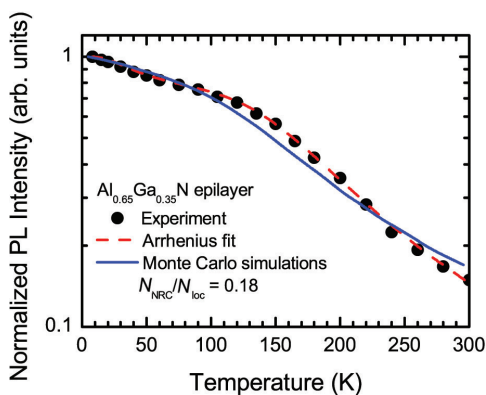


Fig. 3. The temperature dependence of integrated PL intensity in the AlGa_N epilayer with Al content of 65%. Lines show the fits using Eq. (1) (dashed line, red online) and Monte Carlo simulations (solid line, blue online).

using Eq. (1) with $i = 2$ (a dashed line, red online, in Fig. 3) implying involvement of two nonradiative channels with activation energies of 6 and 69 meV. These channels might be tentatively attributed to the exciton redistribution within the localized states and exciton delocalization to the mobility edge, respectively [9].

To link the activation energies to the specific exciton transfer and/or recombination processes, we simulated the exciton dynamics by considering two nonradiative recombination mechanisms: i) exciton delocalization to the mobility edge followed by its capture by a NRC and ii) direct tunnelling to a NRC. To reveal the importance of each mechanism, we first analyse their impact on the temperature dependence of PL intensity separately.

The exciton delocalization and subsequent capture by NRCs is considered to be the main mechanism of nonradiative recombination in the exciton hopping models presented in literature [11–13, 15]. This mechanism is governed by the relative density of nonradiative and localized centres $N_{\text{NRC}}/N_{\text{loc}}$ and by the temperature. The curves of PL efficiency as a function of temperature simulated for several values of parameter $N_{\text{NRC}}/N_{\text{loc}}$ are presented in Fig. 4(a). At low temperatures, the efficiency is practically unaffected and remains close to 100%.

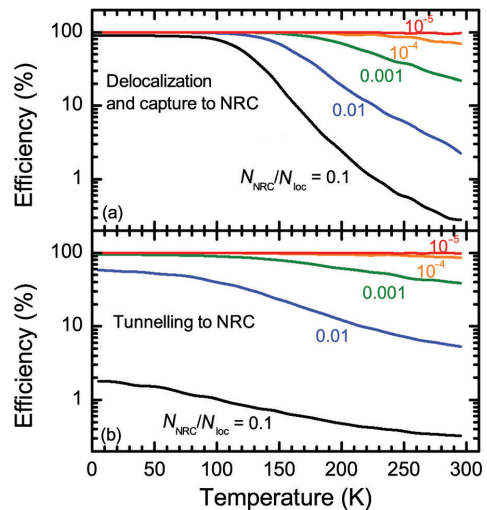


Fig. 4. The simulated PL efficiency dependences on temperature for different nonradiative recombination mechanisms: delocalization and capture to NRCs (a) and direct tunnelling to NRCs (b).

The temperature for the onset of efficiency decrease and the decrease rate afterwards depend on the ratio $N_{\text{NRC}}/N_{\text{loc}}$. As the ratio increases, the PL efficiency decrease onset shifts to lower temperatures, which, in turn, results in a lower room-temperature efficiency. This mechanism is basically a two-step process, thus, the low probability of delocalization ensures almost temperature-unaffected PL intensity at low temperatures. The PL intensity dependences on temperature for this mechanism can be described by Arrhenius-type Eq. (1) with a single thermally-activated channel with activation energy E_A in the range from 107 to 120 meV, and the rate constant c , which reflects the strength of this mechanism and correlates with the parameter $N_{\text{NRC}}/N_{\text{loc}}$.

The rate of direct exciton tunnelling to NRCs depends on how many NRCs are in the close vicinity of a given localized state, thus, this mechanism is governed only by the density of nonradiative centres relative to the density of localized states, described by the parameter $N_{\text{NRC}}/N_{\text{loc}}$. The simulated PL efficiency curves are shown in Fig. 4(b) for several values of this parameter. Usually, the ratio $N_{\text{NRC}}/N_{\text{loc}}$ is assumed to be small and the process of exciton tunnelling to NRC is neglected [13]. Indeed, for low densities of NRCs, only a slight decrease of the PL efficiency is observed at high temperature, as shown in Fig. 4(b). However, the increase in the ratio $N_{\text{NRC}}/N_{\text{loc}}$ results in a significant decrease of the low-temperature efficiency value and a gradual decrease starting already at low temperatures. The former feature is consistent with the previously reported experimental results [12, 18], whereas it is not observed for the nonradiative recombination via delocalized states (see Fig. 4(a)) discussed above. The Arrhenius-type description of PL intensity dependences for the tunnelling mechanism requires two thermally-activated channels with activation energies of the order of 7 and 50 meV.

Comparing the experimental PL intensity dependence (see Fig. 3) with the simulated curves of Fig. 4, several features might be pointed out. A quite significant decrease of PL intensity within the temperature range between 8 and 100 K, observed in the experimentally obtained dependence, implies a strong influence of the direct tunnelling mechanism. Moreover, a high ratio of the measured PL intensities at room and low temperatures, $I_{\text{pl}, 300\text{K}}/I_{\text{pl}, 8\text{K}} = 0.15$, indicates a large value of the parameter $N_{\text{NRC}}/N_{\text{loc}}$. Thus, the tunnelling mechanism

cannot be neglected, and the simulations of PL intensity must include both nonradiative recombination mechanisms. The simulated curve is shown by a blue (online) solid line in Fig. 3. An adequate agreement has been achieved using the $N_{\text{NRC}}/N_{\text{loc}}$ value of 0.18.

Thus, the fitting of simulated and measured dependences revealed that the temperature dependence of PL intensity could not be properly described by taking into account the nonradiative recombination only via delocalized states. The tunnelling to NRCs causes a significant decrease in the low-temperature efficiency value and a gradual decrease in the temperature range where the first mechanism is insignificant. The lower activation energy extracted from the fit using Eq. (1) serves as an indicator of the strong tunnelling mechanism. At temperatures elevated above 100 K, the efficiency decrease might be described by the Arrhenius-type functions for both nonradiative recombination mechanisms. Therefore, the higher activation energy extracted from the fit using Eq. (1) represents an effective average of both processes, except for the epilayers with the low ratio $N_{\text{NRC}}/N_{\text{loc}}$ when the nonradiative recombination proceeds predominantly via delocalized states.

5. Conclusions

To summarize, we simulated the dynamics of a low-density exciton system using the kinetic Monte Carlo algorithm and calculated the temperature dependence of PL intensity in a high-Al-content AlGaIn epilayer to fit it to the experimentally measured dependence. The temperature dependence of the Stokes shift between the mobility edge and the peak position of PL band has been exploited to estimate the parameters necessary for the simulations. The study included two nonradiative recombination mechanisms: recombination via delocalized states and direct tunnelling to NRCs. The analysis and subsequent fitting with experimental results revealed the importance of the direct tunnelling to NRCs in epilayers with a high ratio between the densities of nonradiative recombination centres and localized states, which might be expected in certain III-nitride epilayers, especially in high-Al-content epilayers. The tunnelling to NRCs results in a substantial decrease in the absolute values of low-temperature efficiency

and a gradual efficiency decrease with temperature in the range from 8 to ~ 100 K. The temperature dependence of the efficiency affected exclusively by nonradiative recombination via delocalized states is negligible in this range for any reasonable material parameters. Thus, the gradual efficiency decrease, that has been observed in the epilayer used for fitting in this paper and in many other III-nitride epilayers, has to be attributed to the influence of direct tunnelling to NRCs. Above ~ 100 K temperature, both mechanisms cause the efficiency decrease with temperature, that can be described by an Arrhenius-type function. However, except for the cases when the tunnelling effect might be neglected (at low densities of NRCs), the activation energy extracted from such description of experimental dependence is just an empirical parameter that depends on the activation energies for both processes.

The sample of the $\text{Al}_{0.65}\text{Ga}_{0.35}\text{N}$ epilayer, which has been used for fitting the calculated and measured characteristics in this paper, shows that the contribution of exciton recombination via tunnelling to nonradiative recombination centres might be not only important but also dominant over the nonradiative recombination via delocalized states. The features peculiar to a strong influence of tunnelling are observed in many AlGaIn epilayers, presumably in those with high densities of NRCs. The conclusion on the importance of tunnelling is also consistent with a low luminescence efficiency at low temperatures, which has been observed experimentally. It supports the instruction to cautiously apply the assumption that the low-temperature efficiency is 100% in estimating the absolute values of photoluminescence efficiency at elevated temperatures.

Acknowledgements

The research was supported by the European Social Fund under Grant Agreement with the Research Council of Lithuania (LMTLT) (Project No. LMT-K-712-01-0076). Support for mobility by COST Action CA17126 is also acknowledged.

References

[1] D. Bimberg, M. Sondergeld, and E. Grobe, Thermal dissociation of excitons bound to neu-

- tral acceptors in high-purity GaAs, *Phys. Rev. B* **4**, 3451 (1971).
- [2] M. Hugues, B. Damilano, J.-Y. Duboz, and J. Massies, Exciton dissociation and hole escape in the thermal photoluminescence quenching of (Ga, In)(N, As) quantum wells, *Phys. Rev. B* **75**, 115337 (2007).
- [3] Y. Yang, P. Ma, X. Wei, D. Yan, Y. Wang, and Y. Zeng, Design strategies for enhancing carrier localization in InGaIn-based light-emitting diodes, *J. Lumin.* **155**, 238 (2014).
- [4] H.D. Sun, S. Calvez, M.D. Dawson, J.A. Gupta, G.C. Aers, and G.I. Sproule, Thermal quenching mechanism of photoluminescence in $1.55\ \mu\text{m}$ GaInNASb/Ga(N)As quantum-well structures, *Appl. Phys. Lett.* **89**, 101909 (2006).
- [5] K.L. Teo, J.S. Colton, P.Y. Yu, E.R. Weber, M.F. Li, W. Liu, K. Uchida, H. Tokunaga, N. Akutsu, and K. Matsumoto, An analysis of temperature dependent photoluminescence line shapes in InGaIn, *Appl. Phys. Lett.* **73**, 1697 (1998).
- [6] X.H. Zheng, H. Chen, Z.B. Yan, D.S. Li, H.B. Yu, Q. Huang, and J.M. Zhou, Influence of the deposition time of barrier layers on optical and structural properties of high-efficiency green-light-emitting InGaIn/GaN multiple quantum wells, *J. Appl. Phys.* **96**, 1899 (2004).
- [7] M.A. Sousa, T.C. Esteves, N.B. Sedrine, J. Rodrigues, M.B. Laurenco, A. Redondo-Cubero, E. Alves, K.P. O'Donnell, M. Bockowski, C. Wetzel, M.R. Correia, K. Lorenz, and T. Monteiro, Luminescence studies on green emitting InGaIn/GaN MQWs implanted with nitrogen, *Sci. Rep.* **5**, 9703 (2015).
- [8] A. Yasan, R. McClintock, K. Mayes, D.H. Kim, P. Kung, and M. Razeghi, Photoluminescence study of AlGaIn-based 280 nm ultraviolet light-emitting diodes, *Appl. Phys. Lett.* **83**, 4083 (2003).
- [9] J. Mickevičius, G. Tamulaitis, J. Jurkevičius, M.S. Shur, M. Shatalov, J. Yang, and R. Gaska, Efficiency droop and carrier transport in AlGaIn epilayers and heterostructures, *Phys. Status Solidi B* **252**, 961 (2015).
- [10] S.D. Baranovskii, Theoretical description of charge transport in disordered organic semiconductors, *Phys. Status Solidi B* **252**, 961 (2014).

- [11] O. Rubel, S.D. Baranovskii, K. Hantke, B. Kunert, W.W. Ruhle, P. Thomas, K. Volz, and W. Stolz, Model of temperature quenching of photoluminescence in disordered semiconductors and comparison to experiment, *Phys. Rev. B* **73**, 233201 (2006).
- [12] M. Baranowski, R. Kudrawiec, J. Misiewicz, H. Turski, and C. Skierbiszewski, Photoluminescence characterization of InGaN/InGaN quantum wells grown by plasma-assisted molecular beam epitaxy: impact of nitrogen and gallium fluxes, *Phys. Status Solidi B* **252**, 983 (2015).
- [13] K. Jandieri, B. Kunert, S. Liebich, M. Zimprich, K. Volz, W. Stolz, F. Gebhard, S.D. Baranovskii, N. Koukourakis, N.C. Gerhardt, and M.R. Hofmann, Nonexponential photoluminescence transients in Ga(NAsP) lattice matched to a (001) silicon substrate, *Phys. Rev. B* **87**, 035303 (2013).
- [14] S.D. Baranovskii, R. Eichmann, and P. Thomas, Temperature-dependent exciton luminescence in quantum wells by computer simulation, *Phys. Rev. B* **58**, 13081 (1998).
- [15] M. Baranowski, M. Latkowska, R. Kudrawiec, and J. Misiewicz, Model of hopping excitons in GaInNAs: simulations of sharp lines in micro-photoluminescence spectra and their dependence on the excitation power and temperature, *J. Phys. Condens. Matter* **23**, 205804 (2011).
- [16] P.G. Eliseev, P. Perlin, J. Lee, and M. Osinski, 'Blue' temperature-induced shift and band-tail emission in InGaN-based light sources, *Appl. Phys. Lett.* **71**, 569 (1997).
- [17] K. Kazlauskas, A. Žukauskas, G. Tamulaitis, J. Mickevičius, M.S. Shur, R.S. Qhalid Fareed, J.P. Zhang, and R. Gaska, Exciton hopping and nonradiative decay in AlGaIn epilayers, *Appl. Phys. Lett.* **87**, 172102 (2005).
- [18] J. Mickevičius, G. Tamulaitis, M. Shur, M. Shatalov, J. Tang, and R. Gaska, Internal quantum efficiency in AlGaIn with strong carrier localization, *Appl. Phys. Lett.* **101**, 211902 (2012).

EKSITONINĖS FOTOLIUMINESCENCIJOS AlGaIn EPITAKSINIUOSE SLUOKSNIUOSE TEMPERATŪRINIO GESIMO PRIGIMTIS

O. Kravcov, J. Mickevičius, G. Tamulaitis

Vilniaus universiteto Fotonikos ir nanotechnologijų institutas, Vilnius, Lietuva

Santrauka

Mažo tankio eksitonų sistemos dinamika tirta skaitmeninio modeliavimo metodais naudojant kinetinį Monte Karlo algoritmą. Sumodeliuotos fotoluminescencijos (FL) intensyvumo ir FL juostos Stokso poslinkio temperatūrinės priklausomybės buvo tapatinamos su eksperimentiškai išmatuotomis AlGaIn epitaksiniame sluoksnyje su dideliu Al kiekiu. Darbe analizuojamos

dvejų nespindulinės rekombinacijos mechanizmų – pagavimo per delokalizutas būsenas ir tiesioginio tuneliavimo į nespindulinius centrus – savybės ir poveikis FL efektyvumui. Atskleista stipri tuneliavimo mechanizmo įtaka AlGaIn epitaksiniuose sluoksniuose, pasižyminčiuose dideliu nespindulinių centrų ir lokalizuotų būsenų tankių santykiu.



A series of horizontal lines for writing. The first line starts with a small gap under the pen icon. There are 24 horizontal lines in total.

Vilniaus universiteto leidykla
Saulėtekio al. 9, III rūmai, LT-10222 Vilnius
El. p. info@leidykla.vu.lt, www.leidykla.vu.lt
bookshop.vu.lt, journals.vu.lt
Tiražas 15 egz.